STUDIES OF ENANTIOSPECIFIC INTERACTION BETWEEN CHIRAL MOLECULES AND MAGNETIZED SURFACES

by

Yiyang Lu

B.Sc, Nanjing University, 2014

M.Sc, Nanjing University, 2018

Submitted to the Graduate Faculty of the

Dietrich School of Arts and Sciences in partial fulfillment

of the requirements for the degree of

Doctor of Philosophy

University of Pittsburgh

2023

UNIVERSITY OF PITTSBURGH

DIETRICH SCHOOL OF ARTS AND SCIENCES

This dissertation was presented

by

Yiyang Lu

It was defended on

October 26, 2023

and approved by

Dr. Shigeru Amemiya, Professor, Department of Chemistry

Dr. Geoffrey Hutchison, Associate Professor, Department of Chemistry

Dr. James R McKone, Associate Professor, Chemical and Petroleum Engineering Department

Thesis Advisor/Dissertation Director: Dr. David Waldeck, Professor, Department of Chemistry

STUDIES OF ENANTIOSPECIFIC INTERACTION BETWEEN CHIRAL MOLECULES AND MAGNETIZED SURFACES

Yiyang Lu, PhD

University of Pittsburgh, 2023

The chiral induced spin selectivity (CISS) effect describes the spin-dependent transport of electrons through chiral molecules, in which the preferred spin orientation is determined by the handedness of the molecule and the direction of motion. The CISS effect has attracted considerable research interest due to its important implications across a wide range of scientific fields, including enantiomeric resolution, spin controlled chemical reactions, biorecognition, among others. In this dissertation, fundamental studies on the enantiospecific spin exchange interaction between chiral molecules and magnetized ferromagnetic substrates are investigated and leveraged for enantioseparation, enantiorecognition and enantiospecific polymerization studies. In the first study, the enantiospecific adsorption of cysteine on a ferromagnetic electrode was shown to arise from a kinetically controlled process and not from a thermodynamic stabilization. In the second study, the enantiospecific adsorption of cysteine on a ferromagnetic electrode at different pHs was investigated. Here, the kinetics for enantiospecific adsorption were found to depend strongly on the charge state and geometry of the adsorbate. In the third study, the effects of spin on the enantioselective binding of amino acids with N-acetyl-cysteine coated ferromagnetic electrodes was probed. These studies revealed that the intermolecular interactions between the amino acids and the chiral ferromagnetic surface depend on the electron spin. In the fourth study, Two enantioselective electrochemical reactions that have used polarized electron spins as a chiral reagent are described; enantioselective electroreduction to resolve an enantiomer from a racemic

mixture and an oxidative electropolymerization to generate a chiral polymer from achiral monomers. These studies provide a more fundamental understanding of the CISS effect, identify the key contributions necessary for using the CISS effect in enantioseparations, and shed new light on enantiorecognition.

Table of Contents

List of Tables

List of Figures

Preface

I would like to express my deepest gratitude and appreciation to all those who have contributed to the completion of this doctoral thesis. Their support, guidance, and encouragement have been invaluable throughout this journey, and I am profoundly grateful for their unwavering assistance.

First and foremost, I would like to extend my heartfelt appreciation to my supervisor, Prof. David Waldeck, for his exceptional mentorship, patience, and expertise. He's not just an outstanding scientist, but also an incredible person. His consistent support and guidance have played a vital role in shaping my growth as a scientist. His trust in allowing me the autonomy I needed for my research has been incredibly valuable. Whenever I encountered challenges during my research, Dr. Waldeck's advice was like a guiding light. His patience has brought me a sense of calm during vulnerable moments. Having Dr. Waldeck as my advisor is a true honor, and I'm truly thankful for his significant role in my academic journey. It's hard to put into words how much I appreciate his contributions.

I am also indebted to the members of my thesis committee, Prof. Shigeru Amemiya, Prof. Geoffrey Hutchison and Prof. James McKone for their invaluable feedback and guidance. Their expertise and thoughtful suggestions have greatly contributed to the refinement of this research, and I am honored to have had the opportunity to benefit from their wisdom. During my research journey, I had the privilege of collaborating with great people such as Prof. Ron Naaman (Weizmann Institute of Science), Prof. Joseph Subotnik (University of Pennsylvania), and Dr. Francesco Tassinari (University of Modena Reggio Emilia). Their guidance and support played a pivotal role in the success of my endeavors.

I am also deeply grateful to my lab mates, including Dr. Brian Bloom, Dr. Supriya Ghosh, Dr. Jenny Georgieva, Dr. Caleb Clever, Dr. Simon Wei, Dr. Gouranga Debhnath, Dr. Wiley Dunlap-Shohl, Nazifa Tabassum, Aravind Vadakkayil, Joseph Albro, Jose Enrique Rivas Mata, Meera Joy, Elizabeth Shiby, Keerthana Govindaraj and Mary Molitoris. Right from the outset, Brian has assumed the role of a supportive elder sibling. His unwavering encouragement throughout the past five years has been a cornerstone of my journey. Despite my countless inquiries, even during odd hours, weekends, and holidays, he's consistently exhibited boundless patience and a warm welcome for my questions. His assistance isn't limited to research; he's also been of great help in my daily life, aiding me in managing stress, especially as I approach the imminent journey of becoming a father. He has generously shared a wealth of experiences related to this role. I remain profoundly thankful to Brian for his unending support. Supriya also helped me a lot when I joined the group. He encouraged me to keep learning different projects and techniques, and his guidance has significantly contributed to my learning process. I've learned a lot from him too. I would like to thank all my lab members for the help that they offered during these 5 years, working alongside them has been an incredibly positive experience.

I am thankful to my friends who stood by me during the highs and lows of this Ph.D. endeavor, offering encouragement, laughter, and sometimes a much-needed distraction. Special thanks go to Tim from Thai Gourmet Food Truck Express, where I bought lunch from during these five years. His delicious and affordable food saved me both money and time, providing sustenance and comfort on many busy days.

It is difficult to adequately express my profound gratitude for the incredible family I have been blessed with. My farther Zhengqi Lu and my mother Lihua Gao are the role models in my life. They rarely interfere in my life, consistently offering unwavering support for my decisions.

They have consistently provided me with the security and freedom to pursue my dreams and ambitions. When I accomplish something, they share in my joy while gently cautioning against excessive pride. In times of adversity, they offer encouragement and valuable advice to help me navigate challenges, wholeheartedly bolstering my ambitions. Due to the pandemic, I haven't been able to visit them in the past five years, but they have reassured me not to worry and to take good care of my own family, which is a great comfort to me and allows me to be more focused on my academic pursuits. My aunt Jianha Gao and uncle Xiaoming Jin are both wise individuals who have been incredibly kind to me. They have been living in the United States for many years and have provided me with a great deal of help and convenience since my arrival. Over the past five years, my wife and I have visited them almost every year for relaxation and rejuvenation. My aunt is exceptionally skilled at comforting us; her words are heartwarming and provide me with strength when I doubt myself. My uncle is highly knowledgeable, and whenever I discuss research or planning with him, he consistently offers excellent advice. Meanwhile, I also want to express gratitude to our 'eldest son,' Tiger, a British Shorthair cat. His arrival has added countless joys to our lives. He is sometimes cute, sometimes affectionate, injecting a mischievous touch into what was originally a somewhat monotonous Ph.D. journey.

At this pivotal moment, I also want to extend my heartfelt gratitude to my wife, Tingting Qu. Over these past 5 years, from our initial acquaintance to falling in love, getting married, and now expecting the arrival of our newborn son, her unwavering support and companionship have been the greatest source of joy in my life. We traversed more than 4 years of a long-distance relationship, initially meeting only during holidays. Throughout this time, she seldom voiced complaints and meticulously prepared for each of our meetings, creating precious memories that we both cherish. Later, during the pandemic, we had the opportunity to live together, and her thoughtfulness and love in our daily life made our time together remarkably comfortable. She has consistently shown patience and unwavering support, even in the face of her own academic and research responsibilities. Whenever I encountered difficulties or experienced moments of low spirits, she has consistently been my foremost source of comfort and encouragement. My words fall short in fully expressing my gratitude and affection for her. As we approach the milestones of obtaining our Ph.D. degrees and becoming parents, all I desire is to journey through life's new chapters hand in hand with her.

This thesis is the culmination of years of hard work, and I am grateful to all those who have played a part in its completion.

1.0 Introduction

1.1 Chiral Induced Spin Selectivity (CISS) Effect

An important phenomenon which connects the transmission of electrons and chirality was first reported in 1999 by Waldeck, Naaman and collaborators.[1] In this experiment, they measured the transmission of photoelectrons through a chiral film which consists of only L-or D-stearoyl lysine and found that the photoelectrons yield depended on the excitation polarization of the light source (clockwise vs. counterclockwise) and the handedness of the molecular film. Because circularly polarized light generates spin polarized photoelectrons from the gold substrate,[2] the experiment implies that the molecules were acting as ‘spin filters’.

In other words, when electrons move through a chiral molecule, there will be a spin separation depending on the chirality of the molecule and the motion of the electrons. (See Figure 1.1). The chiral molecule acts as a spin filter. This is called the Chiral Induced Spin Selectivity effect, or CISS effect.[3]

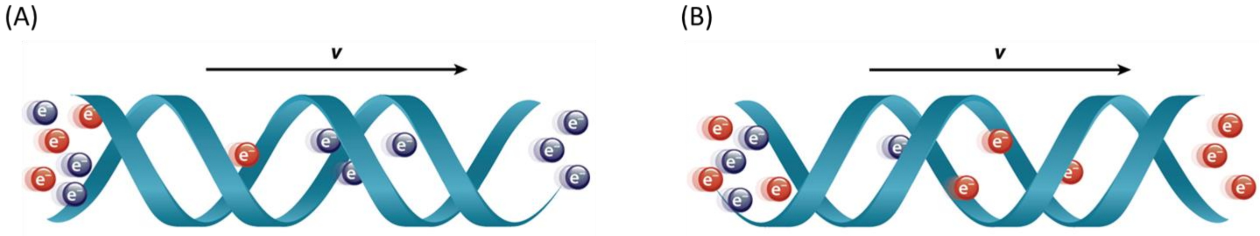

Figure 1.1 A schematic illustration of the CISS effect where the helical potential acts as an electron spin filter. (A) Spin down electrons (blue sphere) prefer to move through the left-handed helix. (B) Spin up electrons (red sphere) prefer to move through the right-handed helix. This figure is taken from reference 4.

Since the discovery of the CISS effect, numerous theoretical and experimental studies have been carried out with different methods and techniques to study this effect in different systems.[5-13] Over the past few years, the CISS effect has attracted considerable research interest because of its important implications across a wide range of scientific fields, including enantioseparations,[14-16] spin controlled chemical reactions,[17-18] biorecognition,[19-20] electron transmission,[4, 21-22] catalysis;[23-25] spintronics,[10, 26-27] and has since been shown to manifest in other systems beyond simple chiral molecules, such as supramolecular assemblies[28-29] and semiconductors.[30-31] Recent progress in this field has focused on fundamental studies to understand the structural and electronic origins of CISS, to provide a deeper understanding of the mechanistic underpinnings and improve our ability to exploit this phenomenon in biological and technological applications. In this introduction chapter, the basic principles of the CISS effect, the application of the CISS effect in spin-controlled separations and reactions, as well as some methods used in my thesis to study the CISS effect are discussed.

1.1.1 Basic principles of the CISS effect

When an electron moves through a chiral molecule, it will experience a chiral electric field ($\vec{E}_{\text{chiral}}$) arising from the electrostatic potential of the molecule. The charge current arising from the motion of the electron through the molecule, will also generate an effective magnetic field in the electron's rest frame $\vec{B}$:

$$\vec{B} = \frac{\vec{v}}{c^2}\vec{E}_{\text{chiral}} \qquad \text{Eq (1.1)}$$

in which $\vec{v}$ is the velocity of the moving electron, c is the speed of light, and $\vec{E}_{\text{chiral}}$ is the electric field acting on the electron while it moves through the chiral molecule (see Figure 1.2A).

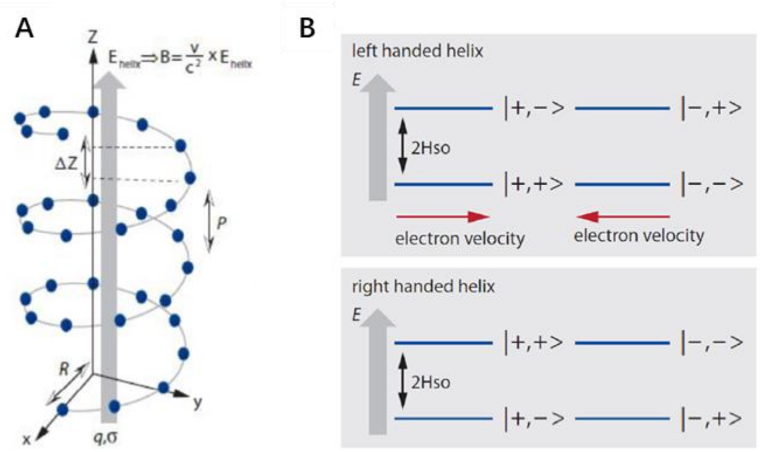

Figure 1.2 (A) The picture shows the essential physical picture of a charge q in spin state σ moving along the axis of a helical charge distribution (blue dots). The parameters are the helix pitch, p, the radius, R, and the spacing of the Δz component of the position vector of the charges distributed along it. The helical field E_{helix} induces a magnetic field B in the rest frame of the charge and hence influences its spin state. (B) The diagram shows the energy scheme for the momentum-spin states, |momentum, spin>, of an electron moving through a left or right-handed helix. This figure is taken from reference 3.

The early works on spin-selective electron transfer or transport are usually associated either with magnetic materials or with materials that have very large spin−orbit coupling (SOC).[32] [33] The SOC that acts on the propagating electrons is referred to as Dresselhaus[34] or Rashba[35], depending on whether they originate from bulk or structure inversion asymmetry, respectively.

The term in the Hamiltonian for the SOC[36] can be written as:

$$H_{\text{SOC}} = \lambda \vec{\sigma} \cdot (\vec{p} \times \vec{E}_{\text{chiral}}) \qquad \text{Eq (1.2)}$$

where $\lambda = \frac{e\hbar}{4m^2c^2}$, $\vec{p}$ is the electron momentum, m is the electron's mass, and $\vec{\sigma}$ is the vector whose components are the Pauli matrices (σ_x, σ_y, σ_z). It indicates that the coupling of the electron spin state and linear momentum plays an important role in the transport of charge through a chiral helix. To explain this, an energy scheme for the momentum-spin states of an electron moving through a chiral helix is shown in Figure 1.2B. Four states associated with a freely propagating electron are denoted by $|+,+\rangle$, $|-,-\rangle$, $|+,-\rangle$, and $|-,+\rangle$. The first variable in the ket represents the direction (right vs left) of the propagating electron and the second represents the electron spin orientation (up vs down). In a left-handed molecule (top right panel), the $|+,+\rangle$ and $|-,-\rangle$ states have lower energy compared to the $|+,-\rangle$,and $|-,+\rangle$ states, and indicates that the up electron is more stabilized when the electron moves to the right (+), while the down spin state (-) is more stabilized when the electron moves to the left (-). In a right-handed molecule (bottom right panel), the $|+,-\rangle$ and $|-,+\rangle$ states have lower energy compared to the $|+,+\rangle$,and $|-,-\rangle$ states, which means that the down spin state (-) is more stabilized when the electron moves to the right (+), while the up spin state (+) is more stabilized when the electron moves to the left (−).

The proposed mechanism above implies that the efficiency of spin filtering is influenced by the magnitude of the SOC, a property known to depend on the effective magnetic field generated during electron propagation. However, the SOC for carbon atoms in a curved molecule is only around 6 meV,[37] which seems too small to explain the considerable spin polarization because of CISS at room temperature. Thus, several theoretical frameworks have been developed in an attempt to adjust the magnitude of the SOC. Naaman and Waldeck[4] considered the motion of an electron similar to cyclotron motion, in which the electron motion is kept within the diameter of the helical molecule.[38] Thus, with the model of cyclotron motion, the SOC is given by Eq (1.3):

$$H_{\text{SOC}} = \frac{g\mu_{\text{B}}}{2}\left|B_{eff}\right| = \frac{g\mu_{\text{B}}mv}{2qr} \qquad \text{Eq (1.3)}$$

where μ_{B} is the Bohr magneton, $\left|B_{eff}\right|$ is the effective magnetic field, and g, m, v, q, and r are the electron's g factor, mass, velocity, charge, and the radius of the helical path of the electron, respectively. If we consider the $m = m_e = 9 \times 10^{-31}$ kg, $q = 1.6 \times 10^{-19}$ C, $v = 6 \times 10^{5}$ m/s (assuming a 1 eV kinetic energy) and $r = 0.5$ nm, then $H_{\text{SOC}} = 390$ meV. The difference between the two spin states in Fig.1.2B is 780 meV. This number exceeds the spin-orbit splittings reported for hydrocarbons by several orders of magnitude, and may be responsible for the CISS effect.[4] Binghai Yan revealed that despite the weak SOC in organic molecules, the orbital polarization effect (OPE) can induce spin polarization assisted by a large SOC of a metal contact. Moreover, OPE can induce spin-selective phenomena even in achiral but inversion-breaking materials.[39] Other theoretical works focus on explaining the large spin polarizations observed in experiments. In work by Ghazaryan *et al.*[40] a model was constructed to describe CISS which implies that the alignment of dipolar fields in relation to the chiral molecule/substrate orientation are important for generating spin polarization. Moreover, Dubi and coworkers presented a theory for the CISS effect based on the interplay between spin–orbit interactions in the electrode, the chirality of the molecule (which induces a solenoid field), and spin-transfer torque at the molecule–electrode spinterface.[41] These studies indicate that the spinterface at chiral molecule / substrate assemblies is crucial for the emergence of spin polarization. Hedegård and co-workers presented a theorem and demonstrated that if there are degeneracies in the molecular spectrum, the SOC does not have to be a small perturbation, the polarization can become large and increase with the length of molecule backbone.[42] Although a holistic mechanism describing CISS remains elusive, these theoretical works correlate well with the spin polarizations observed in experiments and may even predict spin-selective effects in some other materials.

1.1.2 Measurement methods and detection of spin selectivity

Historically, many different techniques have been developed to study the CISS effect. The sections below provide a brief summary of some of the most commonly used methods that are employed.

1.1.2.1 Photoemission Study

The first experiment to observe the CISS effect probed the transmission of spin polarized photoelectrons through a chiral film comprising L-or D-stearoyl lysine. These studies showed that the yield of photoelectrons depended on the polarization of the excitation light and the chirality of the molecules in the film. For instance, Figure 1.3A shows the photoelectron yield is increased through five layers of L-stearoyl lysine when right-handed circularly polarized light is used for the photoemission comparing to linearly polarized light, whereas a decrease for a left-handed circularly polarized light.[1]

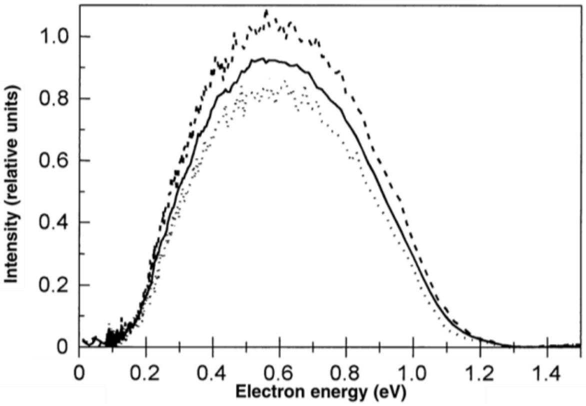

Figure 1.3 (A) Electron energy distribution for five layers of L-stearoyl lysine in which excitation of the photoelectrons was performed using linearly polarized light (solid line), right-handed circularly polarized light (dashed lines), and left-handed circularly polarized light (dotted lines). This figure is rearranged from reference 1.

Later, the spin of polarization of photoelectrons can be directly measured by their angular distribution using a Mott polarimeter. Göhler *et al.*[43] observed a strong spin polarization on a polycrystalline Au substrate coated with a self-assembled monolayer (SAM) of dsDNA. The average spin polarizations are $-54.5 \pm 5.7\ \%$ for the clockwise polarized light, (Figure 1.4A), $-57.2 \pm 5.9\ \%$ for the linearly polarized light (Figure 1.4B) and $-60.8 \pm 5.8\ \%$ for the counterclockwise polarized light (Figure 1.4C).

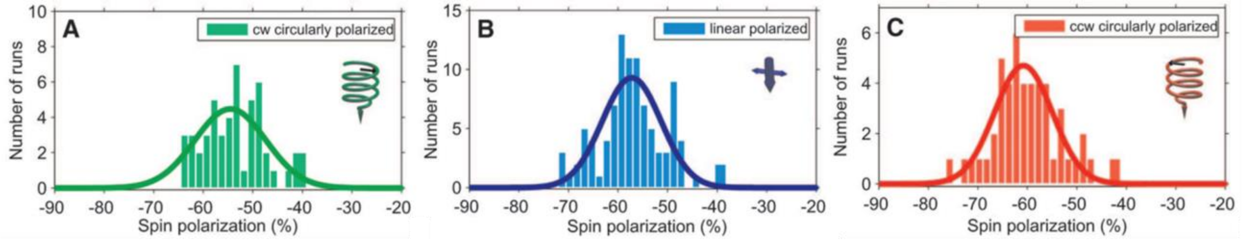

Figure 1.4 The photoelectron polarization as measured for electrons ejected from a poly(Au)-coated substrate with a monolayer of 78-bp dsDNA. For the cw circularly polarized light, the electron polarization is –(54.5 ± 7.0)% [(A), green]; for the linearly polarized light, the polarization is –(57.2 ± 5.9)% [(B), blue]; and for the ccw polarized laser, the electron polarization is –(60.8 ± 5.8)% [(C), red]. This figure is taken from reference 43.

Figure 1.5 shows a schematic illustration of a Mott electron polarimeter set-up, a thin foil of a high-Z material is used as the analyzing target.[43] In such a detector, the spin-orbit interaction is utilized, and the interaction potential depends on the orientation of the spin and the orbit of motion.[44] The spin-dependent scattering results in a left-right intensity asymmetry if the incident electrons are polarized perpendicular to the scattering plane. The spin polarization then can be calculated by Eq (1.4):

$$P = \frac{N_l - N_r}{N_l + N_r} \qquad \text{Eq (1.4)}$$

where N_l and N_r represent the scattering intensities to the left and right counter, respectively.

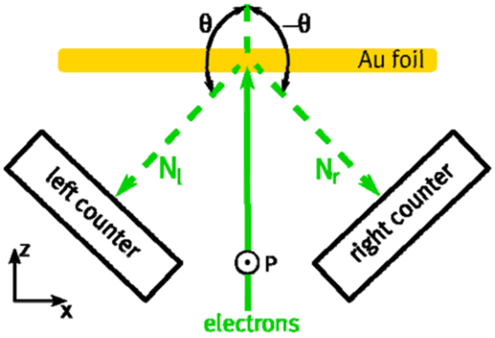

Figure 1.5 Schematic of a Mott electron polarimeter set-up. This figure is taken from reference 43.

1.1.2.2 Magnetic conductive AFM

Magnetic conductive AFM (mc-AFM) is another technique frequently employed to measure the spin-dependent transport of electrons through chiral molecules/materials. This measurement system is similar to conductive AFM, with the exception that the substrate, or tip, is a magnetized ferromagnet with its spin aligned parallel or anti-parallel to the electron transport. Figure 1.6 shows a representative schematic of mc-AFM, in which a ferromagnetic substrate is used. Here, a voltage is applied between a chiral molecule SAM coated Ni/Au substrate and an AFM tip with an external magnetic field. The current is measured between the tip and the chiral SAM coated ferromagnetic substrate.

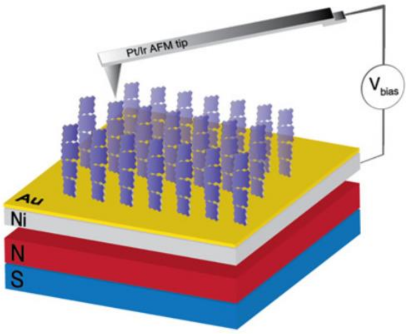

Figure 1.6 Schematic of magnetic conductive AFM . This figure is taken from reference 45.

Upon applying an external magnetic field, the electron spin in the Ni layer will become spin polarized, either parallel or antiparallel to the direction of electron transport. Because of the CISS effect, one spin will prefer to transport more than the other depending on the chirality of the molecule and the electron transport direction, generating a larger spin current. Thus, there will be an asymmetry in the current-voltage (I-V) curve for a pair of enantiomers under opposite magnetization direction. Figure 1.7 shows a representative example of the measurement technique. The I-V curves obtained for an achiral oligomer (PZn_4SAc), panel A, show no discernible difference with magnetic field direction (Figure 1.7A). Conversely, for chiral oligomers with opposite chirality $PZn_4SAc\text{-}B_R$, and $PZn_4SAc\text{-}B_S$, the I-V characteristics depend on the applied magnetic field. For $PZn_4SAc\text{-}B_R$, the current is higher when the applied magnetic dipole direction is up (Figure 1.7B). The reverse is true for $PZn_4SAc\text{-}B_s$ the current is higher when the applied magnetic dipole direction is down. (Figure 1.7C).[45]

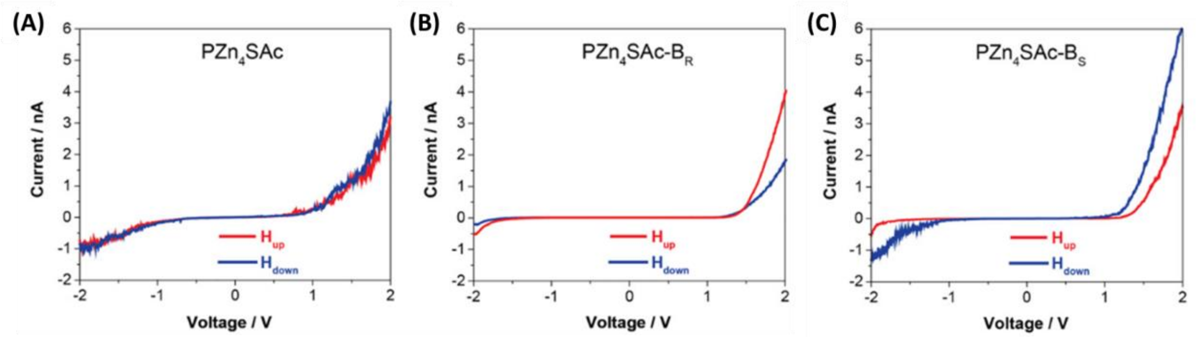

Figure 1.7 Spin-dependent conduction through PZn_4SAc, PZn_4SAc-BR, and PZn_4SAc-BSSAMs. I-V curves obtained for (A) PZn_4SAc, (B) $PZn_4SAc\text{-}B_R$, and(C) $PZn_4SAc\text{-}B_S$, respectively, with the north pole of the magnetic field pointing up (red line) or down (blue line). This figure is taken from reference 45.

1.1.2.3 Hall measurement

A Hall effect device is another measurement method used to detect spin selectivity. The Hall effect was first discovered in 1879 by Edwin Hall,[46] it demonstrates that when current flows between two electrodes with the presence of an perpendicular magnetic field, a potential difference (the Hall voltage) will be produced perpendicular to both the electric and magnetic field. Figure 1.8 shows the schematic representation of a Hall device used for measuring the CISS effect. Here the device is coated with a chiral SAM and a constant current (I_{SD}) flows between the source (S) and drain (D) electrodes. An applied electric field between the gate electrode and the device causes the SAM to become charge polarized, and because of the CISS effect, the charge polarization is accompanied by spin polarization, which generates a magnetic field. The magnetic field is perpendicular to the current flow and, because of the Lorentz force, leads to charge accumulation on the edges of the source-drain channel, a Hall voltage (V_H). Generally, a linear correlation is observed between the applied gate voltage and the Hall response. The slope of the correlation indicates the spin polarization properties of the material upon charge polarization.

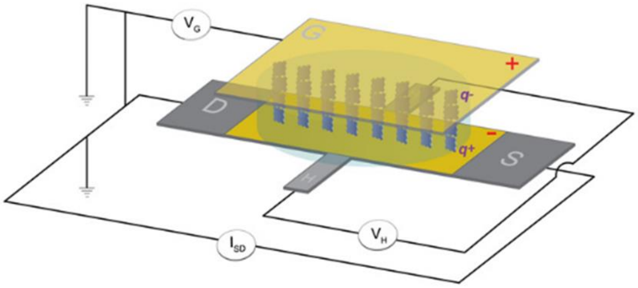

Figure 1.8 Schematic of the spin-polarization Hall device coated with a chiral SAM. The top gate electrode (gold) is used to apply an electric field. A current (I_{SD}) is generated by the applied voltage between source (S) and drain (D) electrodes. Once the gate voltage (V_G) is applied, an electric field (+,-) acts on the SAMs. If charge reorganization (q+,q-) in the SAM is accompanied by spin polarization, a magnetic field is generated that is detected by the device as a Hall voltage (V_H). This figure is taken from reference 45.

Figure 1.9 shows an example of the relationship between Hall voltage and gate voltage for SAMs comprising $PZn_4Sac\text{-}B_R$ and $PZn_4Sac\text{-}B_S$ molecules. The opposite signs of the slopes for $PZn_4SAc\text{-}B_R$ and $PZn_4SAc\text{-}B_S$ SAMs indicate that the opposite charge polarization–induced spin polarizations manifest and are determined by the chirality of the SAM.[45]

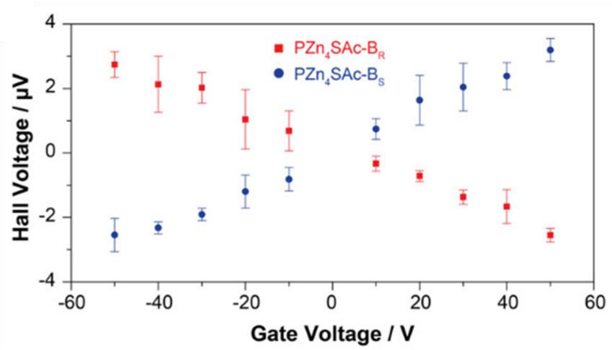

Figure 1.9 The relationship between Hall voltage and gate voltage observed for SAMs of $PZn_4SAc\text{-}B_R$ (red squares) and $PZn_4SAc\text{-}B_S$ (blue circles) SAMs assembling on the gold surface. This figure is taken from reference 45.

1.1.3 Materials which exhibit Spin Filtering

With the different techniques to measure and detect the spin polarization, a wide range of experiments have been performed to confirm the CISS effect in many chiral molecules,

1.1.3.1 DNA and oligopeptides

Earlier studies on the CISS effect were mostly done on either DNAs or oligopeptides with chiral helix secondary structure. Several studies have shown that the electron transport and electron transmission through DNA are spin dependent.[43, 47-48] Studies by Zwang *et al.*[49] demonstrated that the preferred electron spin transferring through DNA is directly determined by the handedness of the double helix. In other studies, Mishra *et al.* [50] used a Hall device to study spin-dependent charge polarization and charge transport through double-stranded DNA of various lengths and through double-stranded DNA containing oxidative damage. These results showed that the spin polarization increases with the length of the DNA and the spin-dependent transport can be enhanced through DNA containing oxidative damage.[11] The CISS effect has also been observed in oligopeptides. The spin polarization in conduction and in electric field-induced polarization for double-stranded DNA oligonucleotides and oligopeptides of different lengths using mc-AFM and Hall device measurement are shown in Figure 1.10.[51] Both of these measurements show that the spin polarization depends linearly on the length, and the spin selectivity per unit length is approximately four times larger for that the oligopeptides than for the dsDNA. It should be noted that the dsDNA and oligopeptide assemblies show an opposite sign of spin polarization, this is because when the handedness of oligopeptides is L made from natural amino acids, while handedness of the dsDNA is D. The preferred spin direction is consistent with variation in the optical activity.[52-53]

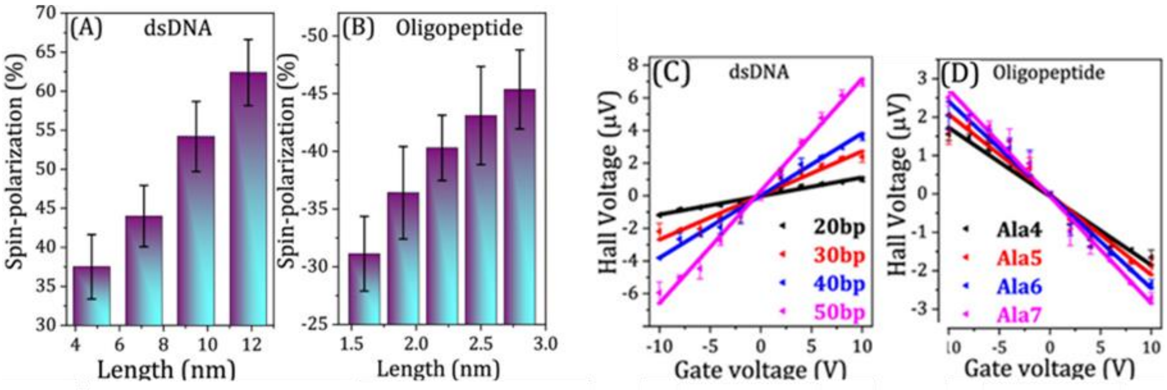

Figure 1.10 (A and B) Histogram summary of spin polarization, $P = \frac{I_U - I_D}{I_U + I_D} \times 100\%$, for various lengths of dsDNA and oligopeptide, respectively, all measured at 2 V. Where I_U andI_D represents the currents measured when the magnetic north pole points up or down, respectively. (C and D) Hall potential measured as a function of the gate voltage for dsDNA and oligopeptide, respectively.This figure is taken from reference 51.

1.1.3.2 Polymers

Spin-dependent electron transport has also been observed in chiral polymers and supramolecular structures that are based on homochiral building blocks possessing stereocenters or even based on achiral monomer but exhibit a chiral secondary structure. In order to find a correlation between molecular properties and spin filtering, the molecules must be organized in a well-defined way on the surface. There are two strategies: (1) use of flat, π-conjugated molecules to self-assemble into chiral molecules lying on the surface (Figure 1.11A). (2) preparation of SAMs employing chiral molecules equipped with anchoring groups standing on the surface (Figure 1.11B). For the polymers lying on the surface, the CISS effect is measured perpendicular to the main molecular axis. Mondal *et al.*[54] investigated spin-selective electron transport through polythiophene and observed the spin polarization of 34%. Kulkarni *et al.*[55] prepared helical supramolecular π-conjugated nanofibers and observed spin filtering in excess of 85%. For the polymers standing on the surface, the CISS effect is measured along the polymer backbone. Mishra *et al.*[56] studied the spin-dependent conduction and polarization in poly(4-ethynylbenzoyl-l-alanine decyl ester) (poly-1L) and poly(4-ethynylbenzoyl-d-alanine decyl ester) (poly-1D), and observed a spin polarization of about 50%. It demonstrates the importance of secondary structure in defining the magnitude of the CISS effect. Mondal *et al.*[28] demonstrated the CISS effect in supramolecular polymers exclusively containing achiral monomers and found that the spin polarization increases to a value of 65% when the length of the chiral self-assembled nanofibers increases. Jia *et al.*[57] explored the CISS effect in a microscale device with self-assembled superhelical conducting polyaniline (PANI) microfibers and a spin-selective efficiency up to 80% was achieved when spins traversed the *ca.* 2–6 μm-long helical channels at room temperature.

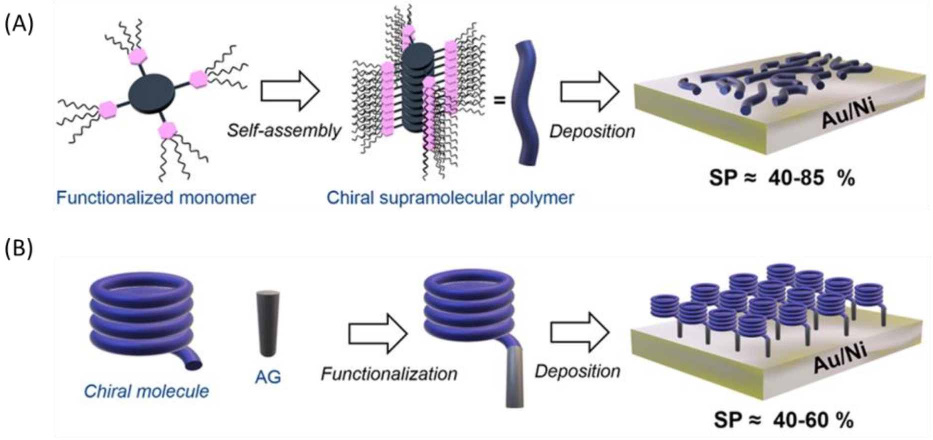

Figure 1.11 Existing strategies to prepare well-ordered chiral assemblies. (A) Chiral polymer lying on the surface. (B) Chiral polymer standing on the surface. This figure is taken from reference 58.

1.1.3.3 Single molecule scale

The CISS effect is not observed only in bulk materials but can also be detected on the single molecule scale. Several studies investigated the electron transfer and efficient spin filtering by single molecules of DNA[59] and oligopeptide[60] with mc-AFM at room temperature. Chiesa *et al.*[61] designed a simple magnetic resonance model system to detect polarization using a qubit sensor. Aragonès *et al*. [62-63] studied the electronic spin filtering capability of a single chiral helical peptide of both L- and D-isomers by measuring the spin-dependent single-molecule conductance and calculated the asymmetry in conductance for the L and D single chiral helical peptide ,which was 60% and 57%, respectively. Figure 1.12 shows the conductance measured for D- (panels A &C) and L-peptides (panels B &D) for spin down (panels A & D) and spin up (panels B & C) electrons. These studies demonstrate a dramatic change in the conductance of the chiral molecules with electron spin.

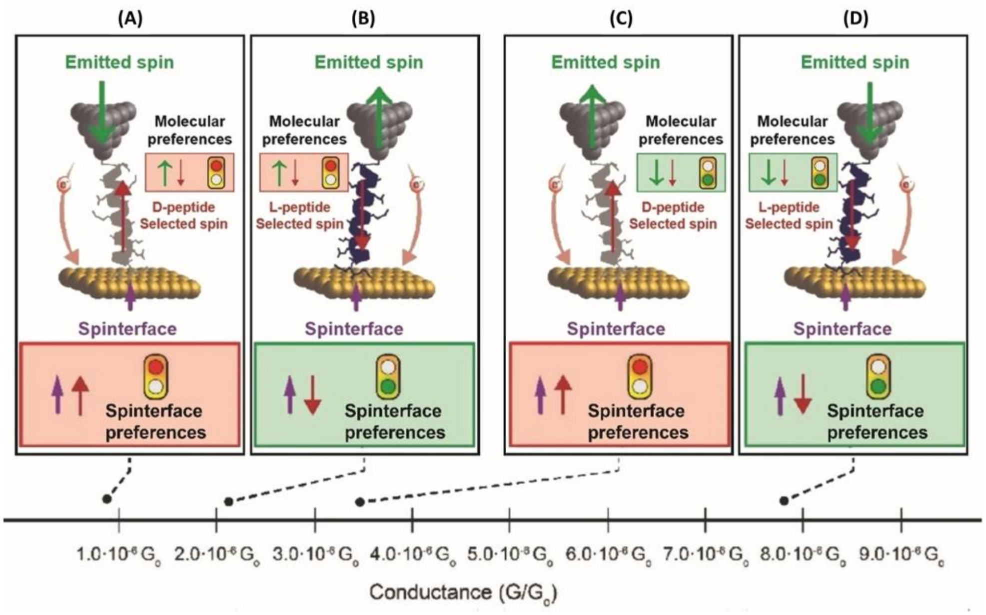

Figure 1.12 Schematic representation of two single-molecule devices based on chiral helical peptides and the spinterface as main ingredients. Experimental conductance values on the x-axis are ordered according to increasing values from left to right. Electron transport is defined by transport from the tip (the spin-polarization is indicated with a green arrow) to the substrate electrode. The binary traffic lights indicate the preferences of each subsystem; molecule (central lights) and spinterface (bottom lights), for the injected spin-polarization direction, where green means match and red means mismatch. D-Peptide support spin-up current polarization and L-peptide supports spin-down polarization. The spinterface, always spin-up polarised (purple arrow), supports spin-down polarization versus spin-up polarization when injected into Au. This figure is taken from reference 62.

1.2 Spin Controlled Enantioseparations

Despite the same molecular structure for a pair of enantiomers, the biochemical properties can be vastly different. As such, a thorough understanding of enantiomeric separation and development of separation techniques are paramount for pharmaceuticals.[64] Two of the leading methods for enantiomer separation methods are chromatography and crystallization.[65] While chromatographic methods possess high efficiency, it is often necessary to tailor the properties of the mobile phase and the stationary phase for each molecular set. Additionally, the cost of the column and the amount of mobile phase (especially when using liquids) is quite considerable.[66] Moreover, crystallization is not a universally applicable approach for chiral resolution. Using the CISS effect to guide enantioseparation through spin controlled interactions, thus provides a novel approach to chiral resolution.

1.2.1 Enantiospecific adsorption on a ferromagnetic substrate

Because of the CISS effect, it has been suggested that the charge redistribution in chiral molecules shows an enantiospecific preference in electron spin orientation, referred to spin-dependent charge reorganization (SDCR).[67] Based on this fact, Banerjee-Ghosh *et al.*[14] showed that the adsorption of L- or D-polyalanine (PAL)-based oligomers onto a structurally achiral but magnetized substrate was enantiospecific (Figure 1.13).

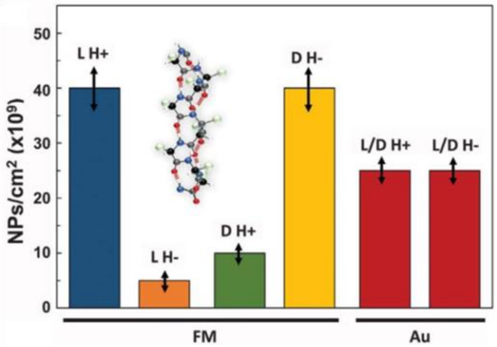

Figure 1.13 Adsorption of L- or D- PAL oligopeptides onto a ferromagnetic subsrate magnetized with the magnetic dipole pointing up (H+) or down (H–). SiO_2 nanoparticles (NPs) were tethered to the adsorbed PAL to act as a marker. A control experiment using a gold substrate, which is not ferromagnetic, did not show a difference in NP density when the chirality of the oligopeptide or the magnetic dipole was changed. This figure is taken from reference 14.

For L-PAL oligomers, a higher density was adsorbed onto a ferromagnetic substrate magnetized with the magnetic dipole pointing up compared to down, while the opposite was true for the D-PAL oligomer; higher density when the ferromagnetic substrate magnetized with the magnetic dipole is pointing down than up. Conversely, when the substrate was not ferromagnetic, the density of L-PAL and D-PAL was the same, independent of the magnetic dipole orientation. These studies demonstrate that the enantiospecificity is not controlled by the magnetic field per se, but originates from electron spin interactions between the chiral molecules and substrate. Because the charge polarization of the chiral molecule is spin specific, the exchange interaction between the molecule and magnetized ferromagnetic substrate dominates the adsorption behavior.

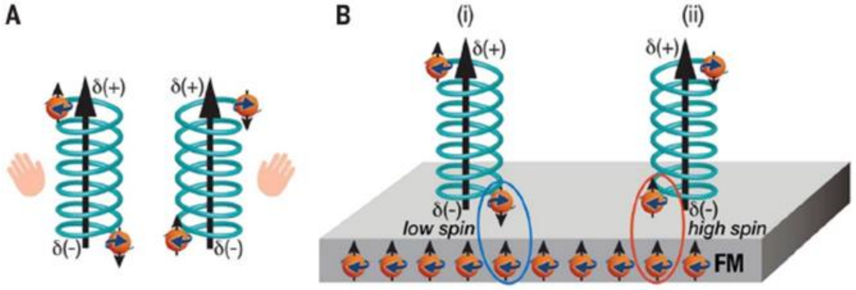

Figure 1.14 (A) A schematic picture of a charge polarization accompanied by a spin polarization. The electrical polarization of the molecule is accompanied by spin polarization. The spin alignment at each electric pole depends on the specific enantiomer. The horizontal arrows indicate the rotation, and the vertical arrows indicate the spin direction. (B) Therefore, for a specific enantiomer, the interaction between the magnetized surface and the molecule (circled in blue and red) follows either a low-spin (i) or a high-spin (ii) potential, depending on the direction of magnetization of the substrate. This figure is taken from reference 14.

Experiments by Ziv *et al*.[68] directly measured the spin exchange interaction between chiral molecules and a magnetic substrate using a spin-polarized scanning tunneling microscope and showed that the energy and force depend on whether the spins are aligned antiparallel or parallel. The experiments reported an energy difference of approximately150 meV at short range. Santra *et al.*[69] studied the adsorption of oxidatively damaged DNA onto magnetized ferromagnetic substrates using confocal fluorescence microscopy and quartz crystal microbalance methods, and showed that the adsorption rate and the coverage depend on the magnetization direction of the substrate and the position of the damage site on the DNA relative to the substrate. Safari *et al.*[70] studied the deposition of chiral heptahelicene $C_{30}H_{18}$ molecules from a racemic powder, and measured the number of each handed molecules on the magnetization direction of the ferromagnetic nanoislands by using low-temperature spin polarized scanning tunneling microscopy and spectroscopy. The experiments show that this enantiospecific adsorption can be achieved on the scale of single molecule scale and demonstrate that the CISS effect relies on single-molecular properties and not on ensemble or cooperative effects.

All these experiments prove that the enantiospecific spin exchange interaction between chiral molecules and a magnetic substrate can be used to separate chiral molecules with a magnet rather than an enantiospecific separating column. Moreover, the interaction depends on the charge polarization of the molecule (accompanied by its spin polarization) because of the CISS effect, which is general in chiral molecules, this separation method is thought to be applied to all chiral molecules.

1.2.2 Enantiospecific crystallization

Crystallization has also been developed to achieve enantioseparation. However, despite its simplicity and cost effectiveness, the strict conditions needed for chiral agent and solvent limits the kinds of enantiomers that can be separated. The discovery of the CISS effect provides a novel and universal method for resolving enantiomers through crystallization. Tassinari *et al.*[16] successfully achieved enantiospecific crystallization of three amino acids: asparagine (Asn), glutamic acid hydrochloride (Glu·HCl) and threonine (Thr) with magnetized ferromagnetic substrates. Here the spin acts as the seed to control selectivity through the alignment of spins between the ferromagnet surface and that of a given enantiomer (see Figure 1.15A). In subsequent studies, Bhowmick *et al*.[71] optimized the experimental setup, having the FM substrates in a vertical configuration and dramatically increased the enantiomeric excess of crystallization to around 100% (see Figure 1.15B). Ozturk *et al.*[72] extends this method from forming small enantiomeric amino acids crystal to RNA precursors. They studied the spin selective crystallization of racemic ribo-aminooxazoline (RAO), an RNA precursor, on magnetite (Fe_3O_4) surfaces, achieving an unprecedented enantiomeric excess of about 60%. The mechanism of the enantiomeric crystallization is shown in Figure 1.16, because of the SDCR effect, the adsorption rate on the surface is enantiospecific (see detailed discussion in section 1.2.1), which allows the surface to induce an asymmetric bias on the formation of the first crystal seeds and leads to an enantiomerically, pure growth of the crystal. These studies are leveraged as a prebiotically plausible pathway for achieving homochirality from completely racemic starting materials; the *i.e.* chiral symmetry-breaking induced by the CISS-controlled spin exchange interactions and self-amplification by conglomerate crystallization of building blocks of life.

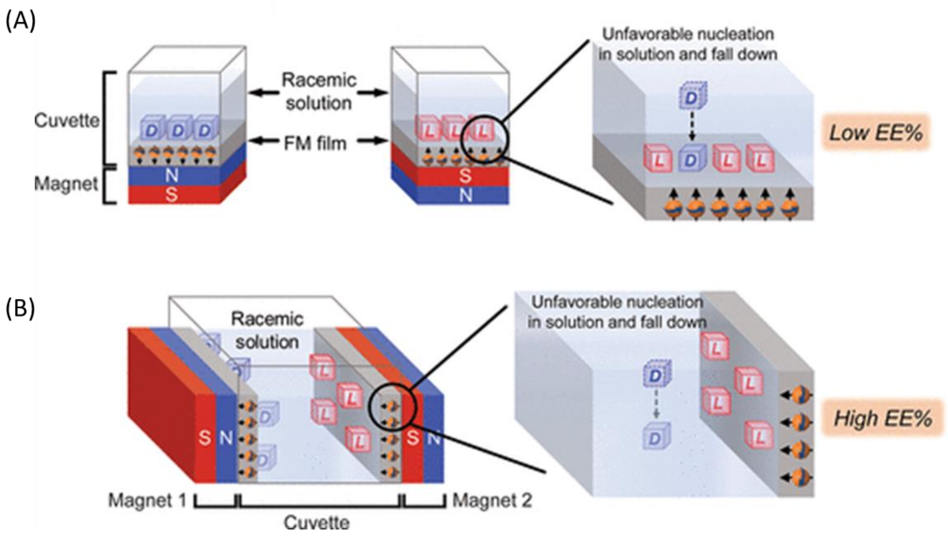

Figure 1.15 (a) Schematic of the experimental setup used in Tassinari's study. (b) Schematic of the setup used in Bhowmick's study. This figure is taken from reference 71.

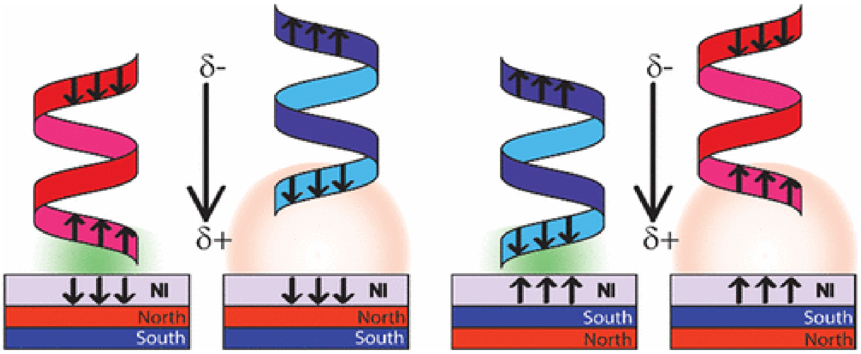

Figure 1.16 Scheme of the enantioselectivecrystallization mechanism. Upon interaction with the surface, the molecules (depicted as helixes in the scheme to represent the chiral structure) undergo a charge redistribution with the formation of a dipole moment, independent of the handedness of the molecule. Due to the SDCR effect, this dipole moment is spin-polarized, and the sign of the polarization depends on the handedness of the molecule. The spin-polarized molecules interact via exchange interaction with the spin-polarized surface, and depending on the handedness of the molecule, the interaction will be attractive or repulsive. This figure is taken from reference 71.

1.3 Spin Control in Chemical reactions

Besides enantioseparation, the other way to produce pure enantiomers of chiral molecules is to introduce asymmetric conditions during the synthesis so that it will preferentially produce one enantiomer over the other. The asymmetry commonly manifests itself as one enantiomer of a chiral reactant, a chiral catalyst, or a chiral solvent.[73] But the spin effects on intermolecular forces have largely been neglected because the total spin of a molecule is zero, even for a radical with unpaired spins, its molecular frame is not strongly coupled to the spin orientation.[67] However, the collision times between molecules are much shorter than the spin depolarization time,[74] so that the spin polarization during the collision can be defined according to the handedness of the molecule through many collisions.[18] Thus, although the total spin of the whole molecule is still zero, the anisotropic spin density can affect the interaction energy between chiral molecules. And the enantiospecific spin exchange interaction can provide a chiral bias for the molecule-molecule interaction.[19, 67] Figure 1.17B illustrates an enantiospecific mechanism for the instantaneous dipole - induced dipole force (dispersion force) acting between two, closed shell, chiral molecules. The blue region represents the electron cloud of a molecule. Because of the SDCR effect, the interaction between homochiral molecules can be viewed as a singlet state with opposite spin direction, so that the Pauli exclusion principle is satisfied (see Figure 1.17C). Yet the interaction between heterochiral molecules is in a triplet state where the spins have the same direction (see Figure 1.17D). Because the singlet state is less repulsive than the triplet state, the interaction is enantiospecific. It is important to appreciate that the spin interaction is a relatively short-range effect and only becomes important for molecules in intimate “contact”, overlapping electron clouds.[18] For chiral molecules, much of the total energy difference results from the Pauli exclusion and can easily exceed the available thermal energy (kT) at room temperature. This mechanism explains the energy difference between homochiral versus heterochiral interactions.

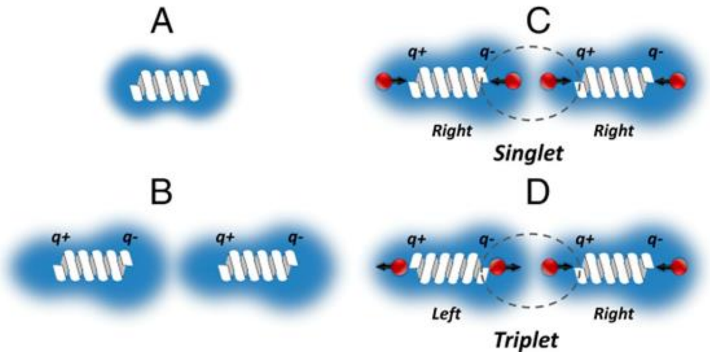

Figure 1.17 The effect of the spin-dependent charge reorganization (SDCR) on the interaction between chiral molecules. (A) The electron distribution (bluecloud) in a molecule that does not have a dipole moment before it interactswith another molecule. In this case, the distribution is symmetric. (B) The electron density distribution where the interaction between two molecules generates a charge polarization, i.e., an induced dipole–induced dipole interaction. (C) The induced dipole interaction of two molecules with the same handedness. As charge q transfers from one side of the molecule to the other, it generates a spin polarization (red ball and black arrow) of the same spin in the two molecules. The electron density left behind has the opposite spin polarization; thus, the interaction between the molecules is characterized by two opposite spins, as illustrated by the dotted circle singlet region. (D) When the two interacting molecules are of opposite chirality, the interaction between the molecules is characterized by two spins parallel to each other (in the dotted circle triplet region). This figure is taken from reference 19.

1.3.1 Enantioselective electropolymerization

Enantiopure chiral polymers are very important in chiral sensors and spintronic applications. The CISS effect has also been found to provide a novel general synthetic method for producing chiral isotactic polymers from their racemic or even achiral monomer units on a magnetized ferromagnetic electrode using the electropolymerization method. For instance, Tassinari *et al.*[75] showed that the electropolymerization of chiral-modified EDOT monomers on a magnetized ferromagnetic substrate is enantiospecific; *i.e.* depends on the spin exchange interactions between a magnetized substrate and the chirality of the monomeric unit. The exchange interactions were found to affect the electron injection barrier and hence polymerization nucleation and propagation. Bloom *et al.*[18] pointed out that asymmetric electrochemical reactions with spin polarized electrons do not require that the reactant molecules possess chirality, because the electron's helicity can evoke chirality in the reaction products. Three different chiral polymer thin films were successfully electropolymerized on a ferromagnetic electrode from achiral monomers (pyrenecarboxylic acid, carbazole, and 3,4-ethylenedioxythiophene). The handedness of the polymer thin film is determined by the orientation of the magnet that is used to magnetize the electrode. Bhowmick *et al.*[76] extended these studies to achieve enantioselective polymerization from achiral monomers poly(2-vinyl pyridine) to produce carbon stereocenters. It is pointed out that every second carbon atom in the backbone is stereogenic and addition of each monomer unit to the growing polymer backbone creates a new chiral center. Thus, the chirality of the polymer chain can be controlled by the electron's spin, which is defined by the magnetic dipole of the ferromagnetic substrate, during polymer propagation. See Figure 1.18 shows a generalized mechanism of the reaction scheme. Moreover, the spin polarization of the polymer film increases with an increase in the layer thickness, which is consistent with some previous experimental results[60, 77-78] and theoretical predictions.[40, 42, 79] Together, these studies illustrate the potential to induce enantioselectivity into polymerization by the electron spin and the possibility of synthesizing complex chiral structures by controlling the magnetization of the surface

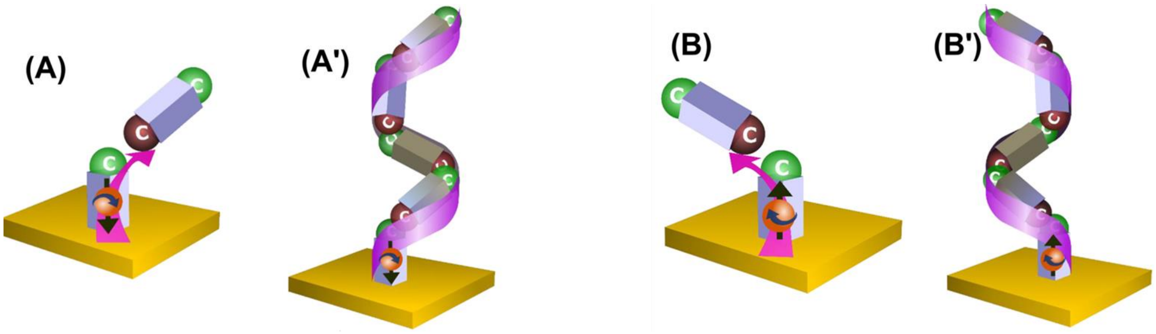

Figure 1.18 Schematic of a proposed mechanism for enantioselective polymerization in the presence of spin-polarized electrons. After the adsorption of the first monomer on the electrode (yellow), a second monomer is adsorbed either in the pro–right-handed (A) or in the pro–left-handed (B) configuration. Spin-polarized electrons are transferred from the electrode into the complex formed. Which spin polarization is injected depends on the magnetization direction of the substrate. One spin-polarized electron (the sphere with an arrow) is preferred for the right-handed configuration, and the opposite spin is preferentially transferred for the left-handed structure. The asymmetric carbon is denoted in green. The sequential polymerization continues, and accordingly, either right-handed (A') or left-handed structures (B') are formed. This figure is taken from reference 76.

1.3.2 Enantioselective electroreduction

Enantioselective asymmetric reduction is another important method in electroorganic reactions resulting in the introduction of one or more new elements of chirality into a target compound.[80] Recent studies have shown that spin-polarized electrons can induce enantioselectivity in the electrochemical reduction of a racemate. Metzger *et al.*[73] electrochemically reduced a solution of racemic camphorsulfonic acid (CSA) with an achiral magnetized substrate and found that the enantiomeric excess of the production depends on the orientation of the magnet used to magnetize the electrode. A maximum enantiomeric excess of about 9% can be reached after 6 h of electrolysis.

Ozturk *et al.*[81] proposed chiral-induced spin selectivity–driven reduction chemistry (CDRC) to explain how one handedness is differentiated from the other in the reduction process. According to CDRC, if the helicity of electrons is biased toward one direction, then one handedness would on average react faster than the other because of the energy difference in the activation energies for different isomers caused by CISS effect. For example, if a left-handed reagent, L–A, reacts faster than a right-handed reagent, D–A, in a reduction reaction driven by electrons in the right-handed helicity state, D–e$^-$, these two reactions can be written as[81]:

$$\mathrm{D{-}A} + \mathrm{D{-}e^-} \rightarrow \mathrm{D{-}B^-}, k_D$$

$$\mathrm{L{-}A} + \mathrm{D{-}e^-} \rightarrow \mathrm{L{-}B^-}, k_L$$

where k_D and k_L are the reaction rate. Thus, $\frac{k_L}{k_D} = \exp\left(\frac{2H_{SO}}{k_BT}\right)$, where H_{SO} is the effective spin-orbit energy, k_B is Boltzmann constant and T is the temperature. The ratio between the reaction rates for different enantiomers can vary from five to several thousand for effective spin-orbit energies (20−100 meV) typically used to account for CISS measurements.[3, 81] With that being said, besides the three main methods to generate chiral bias in electro-organic reactions: chiral electrodes, chiral medium, and chiral auxiliary effects,[80] the CISS effect demonstrates the importance of spin alignment, which could be synergistic with the diastereomeric interaction energy differences found for chiral molecules and create a much larger enantiopurity.

1.3.3 Biorecognition

Non-covalent interactions between molecules is believed to be a key feature for biorecognition,[82] and the existence of the SDCR in chiral molecules implies that the interaction of electron clouds of biomolecules also must include spin-dependent forces. Kapon *et al.*[83] directly measured the interaction force between two chiral peptides (right- and left-handed helical polyalanine peptides) and quantified the difference (about 70 pN) in the interaction force between homochiral and heterochiral pairs of molecules using AFM. Banerjee-Ghosh *et al.*[20] studied the effect of surface magnetization on the kinetics of antigen-antibody binding with a fluorescence microscope and found that the CISS effect can also be utilized to control the long-range charge recognition, and affect the kinetics of antibody–antigen interactions in proteins. Levy *et al.*[84] explored the role of spin-exchange interaction in protein structural stability using fluorescent lifetime experiments and revealed that the spin distribution is very important in internal polypeptide interactions which can affect protein structural stability at different ranges of urea concentrations as shown in Figure 1.19. When there is no urea, the surface spin orientation in ferromagnetic nanoparticles is fixed while that in paramagnetic nanoparticles are readily reoriented to account for optimal interactions with the protein (Figure 1.19A). At low urea concentrations, the paramagnetic nanoparticles can still stabilize the fine structure of the protein and maintain its activity, and the spins in ferromagnetic nanoparticles are not influenced by interactions with the protein (Figure 1.19B). While at high urea concentrations, electron spins in the paramagnetic nanoparticles will readily reorient themselves to accommodate for the inevitable conformational changes in the protein, while the robust and rigid magnetization orientation of the ferromagnetic nanoparticles will not change. Thus, the spin-exchange interaction are also crucial in protein structural dynamics and in the early evolution of proteins on non-organic magnetic surfaces. All these findings imply the importance of spin and exchange interactions in biological processes, which may help better understand the homochirality of nature and the origin of life.

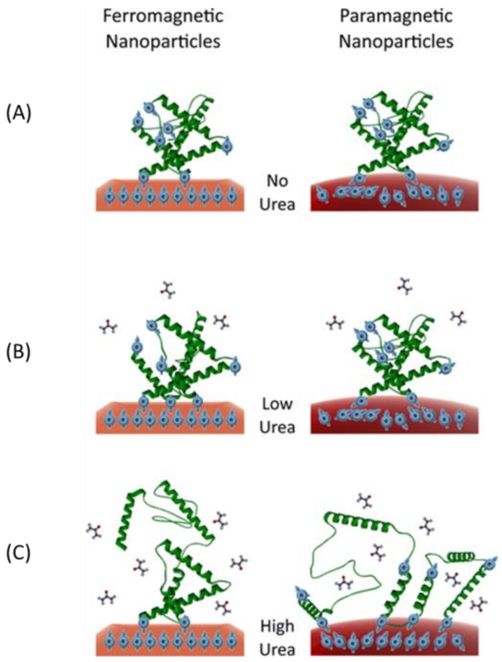

Figure 1.19 Scheme of the spin polarization influence on the structural stability of the proteins in different ranges of urea concentration. At low urea concentrations the paramagnetic nanoparticles stabilize the fine structure of the protein and maintain its activity, whereas at high urea concentrations, major structural changes are impeded by the ferromagnetic nanoparticles. The interaction is controlled by spin exchange interactions due to charge polarization that is accompanied by spin polarization in the proteins that interacts with the magnetic substrate. These interactions are large since the spin wavefunction is localized in the proteins. This figure is taken from reference 84.

1.3.4 Water Splitting

The electron spin direction also plays an important role in the electrochemical anodic oxygen evolution reaction (OER), which remains a significant bottleneck in electrolytic water splitting.[85] The OER involves a spin-unbalanced process from reactants (OH^-/H_2O), existing in a singlet ground state, to product formation(O_2), existing in a triplet ground state.[67] In principle, reactions that involve a transition between singlets and triplets are forbidden, which is suggested to account for the high overpotential of the OER.[86] Naaman's group first discovered that the overpotential can be significantly reduced on a chiral oligopeptide coated substrate.[87] When the electrode is chiral, then the electrons which are transferred have the same spin orientation because of the CISS effect, this will also leave two $OH^{\bullet}$ that have the same spin direction (Figure 1.20 B). Because of the spin alignment, the $OH^{\bullet}$ radicals interact on a triplet surface, and triplet oxygen can be formed through a spin-allowed process, whereas the formation of singlet H_2O_2 is suppressed. If the electrode surface is achiral (Figure 1.20 A), the $OH^{\bullet}$ radicals probably interact on a singlet surface with opposite spins, preferentially forming a singlet H_2O_2. Multiple studies have been conducted to improve the Faradaic efficiency and reaction overpotential with different chiral materials based on CISS effect,[24-25, 88-89] providing a new strategy to improve the oxygen evolution activity by spin control.

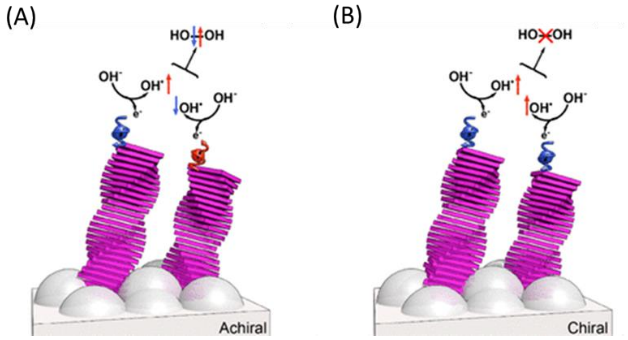

Figure 1.20 Scheme of hydrogen peroxide production. (A) When the electrons transfer to the anodes is non spin specific the spins of the unpaired electrons on the two $OH^{\bullet}$ are aligned antiparallel, hence the interaction between the two $OH^{\bullet}$is on a singlet surface that correlates with the production of hydrogen peroxide (H_2O_2). (B) When the electron transfer to the anode is spin specific, the spins of the two electrons are aligned parallel to each other, hence the two $OH^{\bullet}$ interact on a triplet surface that forbids the formation of H_2O_2 and facilitates the production of oxygen in its ground state. This figure is taken from reference 90.

1.4 Other Important Concepts

1.4.1 Electrochemical Quartz Crystal Microbalance

A quartz crystal microbalance (QCM) can be used to measure the mass change by measuring the frequency change of a quartz crystal resonator.[91] A QCM applies a piezoelectric effect, applying alternating current to the quartz crystal will induce oscillations. A change in thickness of the crystal correlates directly to a change in frequency.

The fundamental frequency of the quartz, f_0, can be calculated as:

$$f_0 = \frac{v_{tr}}{2t_Q} \qquad \text{Eq (1.6)}$$

where the v_{tr} is the transverse velocity, t_Q is the thickness of the quartz. Thus, when materials are deposited on the surface of the crystal, the thickness, t_Q, increases, then the frequency of oscillation decreases. The relationship between the mass change and frequency change can be obtained by the Sauerbrey equation:[92]

$$\Delta f = \frac{-2f_0^2}{A\sqrt{\mu\rho}}\Delta m \qquad \text{Eq (1.7)}$$

where Δf is the frequency change, A is the piezoelectrically active quartz crystal area, μ is the shear modulus of quartz crystal, ρ is the density of quartz, and Δm is the change in mass.

An electrochemical quartz crystal microbalance (EQCM) combines electrochemistry and QCM techniques; both potentiostatic and potentiodynamic responses can be measured in tandem with the mass change at the quartz crystal surface. As such a wide range of experiments to measure the adsorption / desorption,[93] electrodeposition,[94] electrosynthesis process.[95] Figure 1.21 shows the scheme of an EQCM device, the quartz crystal is used as a working electrode and the frequency change of the quartz crystal is recorded as the electrochemical measurement runs.

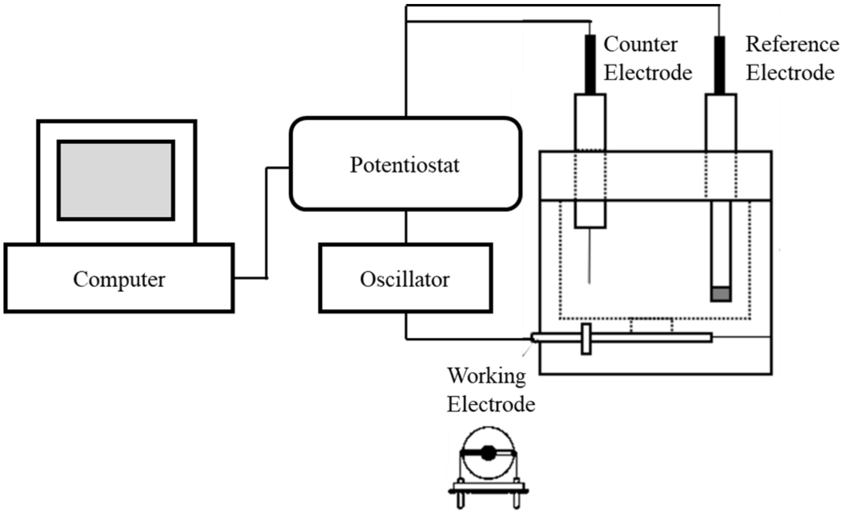

Figure 1.21 Schematic EQCM device. The quartz resonator works as the working electrode in the EQCM cell.

1.4.2 Single-site Langmuir (SSL) adsorption

The Langmuir adsorption model, which was first presented by Irving Langmuir, accounts for adsorption by assuming that the adsorbate behaves as an ideal gas under isothermal conditions and that a given surface has a certain number of equivalent sites to which a species can chemically or physically "stick".[96] There are several assumptions for the adsorption of a single adsorbate onto a series of equivalent sites onto the surface of the solid:[97]

1. The surface is perfectly flat with no corrugations, considered to be homogenous,
2. The adsorbate and binding site form an immobile state after adsorption.
3. Every binding site is identical, and the energy of adsorption is equal.
4. Each binding site can adsorb one molecule at most, which means only a monolayer can form onto the surface.
5. There are no interactions between adsorbed molecules.

If we assume the chemical adsorption is a reversible reaction, we found:

$$A + S \leftrightarrow AS$$

where A, S and AS represent the adsorbate, unoccupied adsorbing site and occupied site, respectively. Thus, the equilibrium constant of this adsorption can be written as:

$$K_{ads} = \frac{[AS]}{[A][S]}$$

where $[A]$ represents the concentration of adsorbate, and we can write a format for the general adsorption isotherm as:

$$\Delta m = \frac{\Delta m_{max} K_{ads} c}{1 + K_{ads} c}$$

where Δm is the mass of adsorption, Δm_{max} is the maximum amount of adsorption. C is the concentration of the adsorbates, which equal to $[A]$. This equation can be linearized as:

$$\frac{c}{\Delta m} = c \frac{1}{\Delta m_{max}} + \frac{1}{K_{ads} \cdot \Delta m_{max}}$$

Thus, the maximum adsorption amount and the adsorption equilibrium constant K_{ads} can be calculated by the slope and intercept value of the linear plot. From the K_{ads}, the Gibbs free energy of the adsorption can be calculated by:

$$K_{ads} = \frac{1}{c_{solvent}} \cdot \exp\left(\frac{-\Delta_{ads} G}{RT}\right)$$

where $c_{solvent}$ is the concentration of the solvent.

1.5 Dissertation Outline

The CISS effect has shown remarkable proof-of-concept for spin-controlled separations and reactions, yet a more fundamental understanding is required to assess the potential of CISSguided enantio resolution in real application. The work presented in this dissertation focuses on the fundamental aspects of enantiospecific spin exchange interactions between chiral molecules and ferromagnetic substrates and demonstrates key aspects in spin-controlled separations and reactions.

Chapter 2 explores the fundamental principles of the CISS effect in enantiospecificity of chiral molecules to magnetized ferromagnetic surfaces. Our work uses a magneto electrochemical quartz crystal microbalance (mEQCM) method to probe the behavior of chiral molecule adsorption on ferromagnetic surfaces. Here, the free energy of adsorption does not change with molecular chirality or electrode magnetization state, but the adsorption rate constant depends strongly on the magnetic field direction and the handedness of the chiral molecule. In addition, the enantioselectivity is shown to depend sensitively on the solution pH and the charge state of the chiral adsorbate.

Chapter 3 continues to explore the effect of solution conditions, pH and solvent isotope composition, on the enantiospecificity of chiral molecules to magnetized ferromagnetic surfaces. Our work uses the mEQCM method in tandem with DFT calculations to probe the effect of ionization state, geometric structure, dipole orientation, and molecule-solvent interactions on the enantiospecific adsorption. These studies show that the adsorbate geometry changes with the pH, resulting in changes in adsorption rate constant and even the preferred magnetization direction. Moreover, solvent-molecule interactions are found to be important variables for controlling efficient enantioseparation.

Chapter 4 investigates the implications of electron spin pairing on the intermolecular interactions of biorecognition mimics. Our work uses mEQCM methods to probe the intermolecular interactions between chiral molecules; the adsorption of amino acids onto chiral N-acetyl-cysteine self-assembled monolayer coated ferromagnetic substrate. Our results suggest that the spin-dependent exchange interactions manifest as changes in both the kinetically driven adsorption process as well as thermodynamically controlled surface energies. The spin-dependent phenomena occur in conjunction with traditional changes in intermolecular interaction energies associated with homochiral and heterochiral architectures. Moreover, the sign of the circular dichroism response of the adsorbate's interacting functional group is shown to be a good metric for predicting the spin preference of the interactions.

Chapter 5 reports two examples of enantioselective reactions at magnetized ferromagnetic electrodes: the kinetic resolution of a racemate via electroreduction, and the electropolymerization of chiral films from achiral monomer units. Our results suggest that enantioselectivity can be impart into chemical reactions by electron spin direction. Moreover, spin-dependent electrochemistry provides the possibility of synthesizing complex chiral structures with multiple chiral centers on surfaces using several steps while controlling both the electric and magnetic fields of the surface.

1.6 Reference

1.Ray, K.; Ananthavel, S.; Waldeck, D.; Naaman, R., Asymmetric scattering of polarized electrons by organized organic films of chiral molecules. *Science* **1999,** *283* (5403), 814-816.

2.Möllers, P. V.; Göhler, B.; Zacharias, H., Chirality Induced Spin Selectivity–the Photoelectron View. *Israel Journal of Chemistry* **2022**, e202200062.

3.Naaman, R.; Waldeck, D. H., Chiral-induced spin selectivity effect. *The journal of physical chemistry letters* **2012,** *3* (16), 2178-2187.

4.Naaman, R.; Waldeck, D. H., Spintronics and chirality: Spin selectivity in electron transport through chiral molecules. *Annual review of physical chemistry* **2015,** *66*, 263-281.

5.Michaeli, K.; Kantor-Uriel, N.; Naaman, R.; Waldeck, D. H., The electron's spin and molecular chirality–how are they related and how do they affect life processes? *Chemical Society Reviews* **2016,** *45* (23), 6478-6487.

6.Fontanesi, C., Spin-dependent electrochemistry: A novel paradigm. *Current Opinion in Electrochemistry* **2018,** *7*, 36-41.

7.Naaman, R.; Paltiel, Y.; Waldeck, D. H., Chiral molecules and the electron spin. *Nature Reviews Chemistry* **2019,** *3* (4), 250-260.

8.Pop, F.; Zigon, N.; Avarvari, N., Main-group-based electro-and photoactive chiral materials. *Chemical reviews* **2019,** *119* (14), 8435-8478.

9.Waldeck, D.; Naaman, R.; Paltiel, Y., The spin selectivity effect in chiral materials. *APL materials* **2021,** *9* (4), 040902.

10.Yang, S.-H.; Naaman, R.; Paltiel, Y.; Parkin, S. S., Chiral spintronics. *Nature Reviews Physics* **2021,** *3* (5), 328-343.

11.Naaman, R.; Paltiel, Y.; Waldeck, D. H., Chiral molecules and the spin selectivity effect. *The journal of physical chemistry letters* **2020,** *11* (9), 3660-3666.

12.Michaeli, K.; Naaman, R., Origin of spin-dependent tunneling through chiral molecules. *The Journal of Physical Chemistry C* **2019,** *123* (27), 17043-17048.

13.Evers, F.; Aharony, A.; Bar‐Gill, N.; Entin‐Wohlman, O.; Hedegård, P.; Hod, O.; Jelinek, P.; Kamieniarz, G.; Lemeshko, M.; Michaeli, K., Theory of chirality induced spin selectivity: Progress and challenges. *Advanced Materials* **2022,** *34* (13), 2106629.

14.Banerjee-Ghosh, K.; Ben Dor, O.; Tassinari, F.; Capua, E.; Yochelis, S.; Capua, A.; Yang, S.-H.; Parkin, S. S.; Sarkar, S.; Kronik, L., Separation of enantiomers by their enantiospecific interaction with achiral magnetic substrates. *Science* **2018,** *360* (6395), 1331-1334.

15.Lu, Y.; Bloom, B.; Qian, S.; Waldeck, D., Enantiospecificity of Cysteine Adsorption on a Ferromagnetic Surface: Is It Kinetically or Thermodynamically Controlled? *The Journal of Physical Chemistry Letters* **2021,** *12* (32), 7854-7858.

16.Tassinari, F.; Steidel, J.; Paltiel, S.; Fontanesi, C.; Lahav, M.; Paltiel, Y.; Naaman, R., Enantioseparation by crystallization using magnetic substrates. *Chemical science* **2019,** *10* (20), 5246-5250.

17.Naaman, R.; Paltiel, Y.; Waldeck, D. H., Chiral induced spin selectivity gives a new twist on spin-control in chemistry. *Accounts of Chemical Research* **2020,** *53* (11), 2659-2667.

18.Bloom, B.; Lu, Y.; Metzger, T.; Yochelis, S.; Paltiel, Y.; Fontanesi, C.; Mishra, S.; Tassinari, F.; Naaman, R.; Waldeck, D., Asymmetric reactions induced by electron spin polarization. *Physical Chemistry Chemical Physics* **2020,** *22* (38), 21570-21582.

19.Kumar, A.; Capua, E.; Kesharwani, M. K.; Martin, J. M.; Sitbon, E.; Waldeck, D. H.; Naaman, R., Chirality-induced spin polarization places symmetry constraints on biomolecular interactions. *Proceedings of the National Academy of Sciences* **2017,** *114* (10), 2474-2478.

20.Banerjee-Ghosh, K.; Ghosh, S.; Mazal, H.; Riven, I.; Haran, G.; Naaman, R., Long-range charge reorganization as an allosteric control signal in proteins. *Journal of the American Chemical Society* **2020,** *142* (48), 20456-20462.

21.Carmeli, I.; Skakalova, V.; Naaman, R.; Vager, Z., Magnetization of chiral monolayers of polypeptide: a possible source of magnetism in some biological membranes. *Angewandte Chemie* **2002,** *114* (5), 787-790.

22.Yang, X.; van der Wal, C. H.; van Wees, B. J., Spin-dependent electron transmission model for chiral molecules in mesoscopic devices. *Physical Review B* **2019,** *99* (2), 024418.

23.Metzger, T. S.; Siam, R.; Kolodny, Y.; Goren, N.; Sukenik, N.; Yochelis, S.; Abu-Reziq, R.; Avnir, D.; Paltiel, Y., Dynamic spin-controlled enantioselective catalytic chiral reactions. *The Journal of Physical Chemistry Letters* **2021,** *12* (23), 5469-5472.

24.Vadakkayil, A.; Clever, C.; Kunzler, K. N.; Tan, S.; Bloom, B. P.; Waldeck, D. H., Chiral electrocatalysts eclipse water splitting metrics through spin control. *Nature Communications* **2023,** *14* (1), 1067.

25.Ghosh, S.; Bloom, B. P.; Lu, Y.; Lamont, D.; Waldeck, D. H., Increasing the efficiency of water splitting through spin polarization using cobalt oxide thin film catalysts. *The Journal of Physical Chemistry C* **2020,** *124* (41), 22610-22618.

26.Brandt, J. R.; Salerno, F.; Fuchter, M. J., The added value of small-molecule chirality in technological applications. *Nature Reviews Chemistry* **2017,** *1* (6), 0045.

27.Yang, S.-H., Spintronics on chiral objects. *Applied Physics Letters* **2020,** *116* (12), 120502.

28.Mondal, A. K.; Preuss, M. D.; Ślęczkowski, M. L.; Das, T. K.; Vantomme, G.; Meijer, E.; Naaman, R., Spin filtering in supramolecular polymers assembled from achiral monomers mediated by chiral solvents. *Journal of the American Chemical Society* **2021,** *143* (18), 7189-7195.

29.Qian, Q.; Ren, H.; Zhou, J.; Wan, Z.; Zhou, J.; Yan, X.; Cai, J.; Wang, P.; Li, B.; Sofer, Z., Chiral molecular intercalation superlattices. *Nature* **2022,** *606* (7916), 902-908.

30.Feng, T.; Wang, Z.; Zhang, Z.; Xue, J.; Lu, H., Spin selectivity in chiral metal–halide semiconductors. *Nanoscale* **2021,** *13* (45), 18925-18940.

31.Lu, H.; Vardeny, Z. V.; Beard, M. C., Control of light, spin and charge with chiral metal halide semiconductors. *Nature Reviews Chemistry* **2022,** *6* (7), 470-485.

32.Lu, J. P.; Yau, J.-B.; Shukla, S.; Shayegan, M.; Wissinger, L.; Rössler, U.; Winkler, R., Tunable spin-splitting and spin-resolved ballistic transport in GaAs/AlGaAs two-dimensional holes. *Physical review letters* **1998,** *81* (6), 1282.

33.Datta, S.; Das, B., Electronic analog of the electro‐optic modulator. *Applied Physics Letters* **1990,** *56* (7), 665-667.

34.Dresselhaus, G., Spin-orbit coupling effects in zinc blende structures. *Physical Review* **1955,** *100* (2), 580.

35.Rashba, E., Properties of semiconductors with an extremum loop. I. Cyclotron and combinational resonance in a magnetic field perpendicular to the plane of the loop. *Sov. Phys.-Solid State* **1960,** *2*, 1109.

36.Winkler, R., *Spin-orbit coupling effects in two-dimensional electron and hole systems*. Springer: 2003; Vol. 191.

37.Huertas-Hernando, D.; Guinea, F.; Brataas, A., Spin-orbit coupling in curved graphene, fullerenes, nanotubes, and nanotube caps. *Physical Review B* **2006,** *74* (15), 155426.

38.Fuchs, J.; Piéchon, F.; Goerbig, M.; Montambaux, G., Topological Berry phase and semiclassical quantization of cyclotron orbits for two dimensional electrons in coupled band models. *The European Physical Journal B* **2010,** *77* (3), 351-362.

39.Liu, Y.; Xiao, J.; Koo, J.; Yan, B., Chirality-driven topological electronic structure of DNA-like materials. *Nature materials* **2021,** *20* (5), 638-644.

40.Ghazaryan, A.; Paltiel, Y.; Lemeshko, M., Analytic model of chiral-induced spin selectivity. *The Journal of Physical Chemistry C* **2020,** *124* (21), 11716-11721.

41.Alwan, S.; Dubi, Y., Spinterface origin for the chirality-induced spin-selectivity effect. *Journal of the American Chemical Society* **2021,** *143* (35), 14235-14241.

42.Dalum, S.; Hedegård, P., Theory of chiral induced spin selectivity. *Nano letters* **2019,** *19* (8), 5253-5259.

43.Göhler, B.; Hamelbeck, V.; Markus, T.; Kettner, M.; Hanne, G.; Vager, Z.; Naaman, R.; Zacharias, H., Spin selectivity in electron transmission through self-assembled monolayers of double-stranded DNA. *Science* **2011,** *331* (6019), 894-897.

44.Kessler, J., *Polarized electrons*. Springer Science & Business Media: 1985; Vol. 1.

45.Ko, C.-H.; Zhu, Q.; Tassinari, F.; Bullard, G.; Zhang, P.; Beratan, D. N.; Naaman, R.; Therien, M. J., Twisted molecular wires polarize spin currents at room temperature. *Proceedings of the National Academy of Sciences* **2022,** *119* (6), e2116180119.

46.Hall, E. H., On a new action of the magnet on electric currents. *American Journal of Mathematics* **1879,** *2* (3), 287-292.

47.Abendroth, J. M.; Nakatsuka, N.; Ye, M.; Kim, D.; Fullerton, E. E.; Andrews, A. M.; Weiss, P. S., Analyzing spin selectivity in DNA-mediated charge transfer via fluorescence microscopy. *ACS nano* **2017,** *11* (7), 7516-7526.

48.Xie, Z.; Markus, T. Z.; Cohen, S. R.; Vager, Z.; Gutierrez, R.; Naaman, R., Spin specific electron conduction through DNA oligomers. *Nano letters* **2011,** *11* (11), 4652-4655.

49.Zwang, T. J.; Hurlimann, S.; Hill, M. G.; Barton, J. K., Helix-dependent spin filtering through the DNA duplex. *Journal of the American Chemical Society* **2016,** *138* (48), 15551-15554.

50.Mishra, S.; Poonia, V. S.; Fontanesi, C.; Naaman, R.; Fleming, A. M.; Burrows, C. J., Effect of oxidative damage on charge and spin transport in DNA. *Journal of the American Chemical Society* **2018,** *141* (1), 123-126.

51.Mishra, S.; Mondal, A. K.; Pal, S.; Das, T. K.; Smolinsky, E. Z.; Siligardi, G.; Naaman, R., Length-dependent electron spin polarization in oligopeptides and DNA. *The Journal of Physical Chemistry C* **2020,** *124* (19), 10776-10782.

52.Bloom, B. P.; Graff, B. M.; Ghosh, S.; Beratan, D. N.; Waldeck, D. H., Chirality control of electron transfer in quantum dot assemblies. *Journal of the American Chemical Society* **2017,** *139* (26), 9038-9043.

53.Metzger, T. S.; Batchu, H.; Kumar, A.; Fedotov, D. A.; Goren, N.; Bhowmick, D. K.; Shioukhi, I.; Yochelis, S.; Schapiro, I.; Naaman, R., Optical Activity and Spin Polarization: The Surface Effect. *Journal of the American Chemical Society* **2023,** *145* (7), 3972-3977.

54.Mondal, P. C.; Kantor‐Uriel, N.; Mathew, S. P.; Tassinari, F.; Fontanesi, C.; Naaman, R., Chiral conductive polymers as spin filters. *Advanced Materials* **2015,** *27* (11), 1924-1927.

55.Kulkarni, C.; Mondal, A. K.; Das, T. K.; Grinbom, G.; Tassinari, F.; Mabesoone, M. F.; Meijer, E.; Naaman, R., Highly efficient and tunable filtering of Electrons' spin by supramolecular chirality of nanofiber‐based materials. *Advanced Materials* **2020,** *32* (7), 1904965.

56.Mishra, S.; Mondal, A. K.; Smolinsky, E. Z.; Naaman, R.; Maeda, K.; Nishimura, T.; Taniguchi, T.; Yoshida, T.; Takayama, K.; Yashima, E., Spin filtering along chiral polymers. *Angewandte Chemie International Edition* **2020,** *59* (34), 14671-14676.

57.Jia, L.; Wang, C.; Zhang, Y.; Yang, L.; Yan, Y., Efficient spin selectivity in self-assembled superhelical conducting polymer microfibers. *ACS nano* **2020,** *14* (6), 6607-6615.

58.Labella, J.; Bhowmick, D. K.; Kumar, A.; Naaman, R.; Torres, T., Easily processable spin filters: exploring the chiral induced spin selectivity of bowl-shaped chiral subphthalocyanines. *Chemical Science* **2023**.

59.Nogues, C.; Cohen, S. R.; Daube, S. S.; Naaman, R., Electrical properties of short DNA oligomers characterized by conducting atomic force microscopy. *Physical Chemistry Chemical Physics* **2004,** *6* (18), 4459-4466.

60.Kettner, M.; Gohler, B.; Zacharias, H.; Mishra, D.; Kiran, V.; Naaman, R.; Fontanesi, C.; Waldeck, D. H.; Sęk, S.; Pawłowski, J., Spin filtering in electron transport through chiral oligopeptides. *The Journal of Physical Chemistry C* **2015,** *119* (26), 14542-14547.

61.Chiesa, A.; Chizzini, M.; Garlatti, E.; Salvadori, E.; Tacchino, F.; Santini, P.; Tavernelli, I.; Bittl, R.; Chiesa, M.; Sessoli, R., Assessing the nature of chiral-induced spin selectivity by magnetic resonance. *The Journal of Physical Chemistry Letters* **2021,** *12* (27), 6341-6347.

62.Aragonès, A. C.; Aravena, D.; Ugalde, J. M.; Medina, E.; Gutierrez, R.; Ruiz, E.; Mujica, V.; Díez‐Pérez, I., Magnetoresistive Single‐Molecule Junctions: the Role of the Spinterface and the CISS Effect. *Israel Journal of Chemistry* **2022**, e202200090.

63.Aragonès, A. C.; Medina, E.; Ferrer‐Huerta, M.; Gimeno, N.; Teixidó, M.; Palma, J. L.; Tao, N.; Ugalde, J. M.; Giralt, E.; Díez‐Pérez, I., Measuring the spin‐polarization power of a single chiral molecule. *small* **2017,** *13* (2), 1602519.

64.Williams, K.; Lee, E., Importance of drug enantiomers in clinical pharmacology. *Drugs* **1985,** *30* (4), 333-354.

65.Porter, W. H., Resolution of chiral drugs. *Pure and applied chemistry* **1991,** *63* (8), 1119-1122.

66.Schurig, V., Separation of enantiomers by gas chromatography. *Journal of Chromatography A* **2001,** *906* (1-2), 275-299.

67.Naaman, R.; Paltiel, Y.; Waldeck, D. H., Chiral induced spin selectivity and its implications for biological functions. *Annual review of biophysics* **2022,** *51*, 99-114.

68.Ziv, A.; Saha, A.; Alpern, H.; Sukenik, N.; Baczewski, L. T.; Yochelis, S.; Reches, M.; Paltiel, Y., AFM‐Based Spin‐Exchange Microscopy Using Chiral Molecules. *Advanced Materials* **2019,** *31* (40), 1904206.

69.Santra, K.; Lu, Y.; Waldeck, D. H.; Naaman, R., Spin Selectivity Damage Dependence of Adsorption of dsDNA on Ferromagnets. *The Journal of Physical Chemistry B* **2023,** *127* (11), 2344-2350.

70.Safari, M. R.; Matthes, F.; Ernst, K.-H.; Bürgler, D. E.; Schneider, C. M., Enantiospecific adsorption on a ferromagnetic surface at the single-molecule scale. *arXiv preprint arXiv:2211.12976* **2022**.

71.Bhowmick, D.; Sang, Y.; Santra, K.; Halbauer, M.; Capua, E.; Paltiel, Y.; Naaman, R.; Tassinari, F., Simultaneous High-Purity Enantiomeric Resolution of Conglomerates Using Magnetic Substrates. *Crystal growth & design* **2021,** *21* (5), 2925-2931.

72.Ozturk, S. F.; Liu, Z.; Sutherland, J. D.; Sasselov, D. D., Origin of Biological Homochirality by Crystallization of an RNA Precursor on a Magnetic Surface. *arXiv preprint arXiv:2303.01394* **2023**.

73.Metzger, T. S.; Mishra, S.; Bloom, B. P.; Goren, N.; Neubauer, A.; Shmul, G.; Wei, J.; Yochelis, S.; Tassinari, F.; Fontanesi, C., The electron spin as a chiral reagent. *Angewandte Chemie* **2020,** *132* (4), 1670-1675.

74.Prisner, T.; Rohrer, M.; MacMillan, F., Pulsed EPR spectroscopy: biological applications. *Annual review of physical chemistry* **2001,** *52* (1), 279-313.

75.Tassinari, F.; Amsallem, D.; Bloom, B. P.; Lu, Y.; Bedi, A.; Waldeck, D. H.; Gidron, O.; Naaman, R., Spin-dependent enantioselective electropolymerization. *The Journal of Physical Chemistry C* **2020,** *124* (38), 20974-20980.

76.Bhowmick, D. K.; Das, T. K.; Santra, K.; Mondal, A. K.; Tassinari, F.; Schwarz, R.; Diesendruck, C. E.; Naaman, R., Spin-induced asymmetry reaction—The formation of asymmetric carbon by electropolymerization. *Science Advances* **2022,** *8* (31), eabq2727.

77.Ghosh, K.; Zhang, W.; Tassinari, F.; Mastai, Y.; Lidor-Shalev, O.; Naaman, R.; Möllers, P.; Nürenberg, D.; Zacharias, H.; Wei, J., Controlling chemical selectivity in electrocatalysis with chiral CuO-coated electrodes. *The Journal of Physical Chemistry C* **2019,** *123* (5), 3024-3031.

78.Díaz, E.; Domínguez-Adame, F.; Gutierrez, R.; Cuniberti, G.; Mujica, V., Thermal decoherence and disorder effects on chiral-induced spin selectivity. *The Journal of Physical Chemistry Letters* **2018,** *9* (19), 5753-5758.

79.Zöllner, M. S.; Saghatchi, A.; Mujica, V.; Herrmann, C., Influence of electronic structure modeling and junction structure on first-principles chiral induced spin selectivity. *Journal of Chemical Theory and Computation* **2020,** *16* (12), 7357-7371.

80.Ghosh, M.; Shinde, V. S.; Rueping, M., A review of asymmetric synthetic organic electrochemistry and electrocatalysis: concepts, applications, recent developments and future directions. *Beilstein Journal of Organic Chemistry* **2019,** *15* (1), 2710-2746.

81.Ozturk, S. F.; Sasselov, D. D., On the origins of life's homochirality: Inducing enantiomeric excess with spin-polarized electrons. *Proceedings of the National Academy of Sciences* **2022,** *119* (28), e2204765119.

82.Berthod, A., Chiral recognition mechanisms. ACS Publications: 2006.

83.Kapon, Y.; Saha, A.; Duanis-Assaf, T.; Stuyver, T.; Ziv, A.; Metzger, T.; Yochelis, S.; Shaik, S.; Naaman, R.; Reches, M., Evidence for new enantiospecific interaction force in chiral biomolecules. *Chem* **2021,** *7* (10), 2787-2799.

84.Levy, H. M.; Schneider, A.; Tiwari, S.; Zer, H.; Yochelis, S.; Goloubinoff, P.; Keren, N.; Paltiel, Y., The effect of spin exchange interaction on protein structural stability. *Physical Chemistry Chemical Physics* **2022,** *24* (47), 29176-29185.

85.Shi, Q.; Zhu, C.; Du, D.; Lin, Y., Robust noble metal-based electrocatalysts for oxygen evolution reaction. *Chemical Society Reviews* **2019,** *48* (12), 3181-3192.

86.Li, X.; Cheng, Z.; Wang, X., Understanding the mechanism of the oxygen evolution reaction with consideration of spin. *Electrochemical Energy Reviews* **2021,** *4*, 136-145.

87.Mtangi, W.; Kiran, V.; Fontanesi, C.; Naaman, R., Role of the electron spin polarization in water splitting. *The journal of physical chemistry letters* **2015,** *6* (24), 4916-4922.

88.Huang, Q.; Xie, S.; Hao, J.; Ding, Z.; Zhang, C.; Sheng, H.; Zhao, J., Spin‐Enhanced O‐H Cleavage in Electrochemical Water Oxidation. *Angewandte Chemie International Edition* **2023**, e202300469.

89.Feng, T.; Chen, W.; Xue, J.; Cao, F.; Chen, Z.; Ye, J.; Xiao, C.; Lu, H., Spin Polarization of Chiral Amorphous Fe‐Ni Electrocatalysts Enabling Efficient Electrochemical Oxygen Evolution. *Advanced Functional Materials* **2023**, 2215051.

90.Mtangi, W.; Tassinari, F.; Vankayala, K.; Vargas Jentzsch, A.; Adelizzi, B.; Palmans, A. R.; Fontanesi, C.; Meijer, E.; Naaman, R., Control of electrons' spin eliminates hydrogen peroxide formation during water splitting. *Journal of the American Chemical Society* **2017,** *139* (7), 2794-2798.

91.King, W. H., Piezoelectric sorption detector. *Analytical Chemistry* **1964,** *36* (9), 1735-1739.

92.Sauerbrey, G., Verwendung von Schwingquarzen zur Wägung dünner Schichten und zur Mikrowägung. *Zeitschrift für physik* **1959,** *155*, 206-222.

93.Schneider, T. W.; Buttry, D. A., Electrochemical quartz crystal microbalance studies of adsorption and desorption of self-assembled monolayers of alkyl thiols on gold. *Journal of the American Chemical Society* **1993,** *115* (26), 12391-12397.

94.Herrero, E.; Buller, L. J.; Abruña, H. D., Underpotential deposition at single crystal surfaces of Au, Pt, Ag and other materials. *Chemical Reviews* **2001,** *101* (7), 1897-1930.

95.Bohannan, E. W.; Huang, L.-Y.; Miller, F. S.; Shumsky, M. G.; Switzer, J. A., In situ electrochemical quartz crystal microbalance study of potential oscillations during the electrodeposition of Cu/Cu2O layered nanostructures. *Langmuir* **1999,** *15* (3), 813-818.

96.Langmuir, I., The adsorption of gases on plane surfaces of glass, mica and platinum. *Journal of the American Chemical society* **1918,** *40* (9), 1361-1403.

97.Masel, R. I., *Principles of adsorption and reaction on solid surfaces*. John Wiley & Sons: 1996; Vol. 3.

2.0 Enantiospecificity of Cysteine Adsorption on a Ferromagnetic Surface: Is it Kinetically or Thermodynamically Controlled?

This work was published as Lu, Y., Bloom, B. P., Qian, S., Waldeck, D. H. *The Journal of Physical Chemistry Letters*, **2021**, 12, 7854-7858. The author of the dissertation performed the design of the experiments, the electrochemical quartz crystal microbalance measurement, data analysis and participated in writing the manuscript. The supporting information for this chapter can be found in Appendix A.

This work uses electrochemical quartz crystal balance methods to demonstrate that the enantiospecific adsorption of chiral molecules (cysteine is used as a model) on a ferromagnetic surface arises from the kinetics of adsorption and not from a thermodynamic stabilization. Measurements of the Gibbs free energy of adsorption for different chiral forms of cysteine and different electrode magnetization states show no significant differences, whereas measurements of the adsorption and desorption kinetics reveal a strong dependence, implying that the magnetization state of the electrode surface can be used to distinguish enantiomeric forms of cysteine. In addition, the enantioselectivity is shown to depend sensitively on the solution pH and the charge state of the chiral adsorbate.

2.1 Introduction

Enantiopurity has been long known to affect the efficacy of pharmaceuticals[1] as well as chemical agents in other applications, such as agriculture.[2] This fact has driven the development of methods for chiral resolution including an array of chromatographic techniques and the crystallization of diastereomeric salts.[3-5] A recent study by Banerjee-Ghosh *et al.*[6] showed that magnetized metal surfaces could be used to resolve a racemic solution of oligopeptides in a flow cell, for which the elution time of the oligopeptide depends on the magnetization direction of the magnetized surface and the handedness of the enantiomer. The enantiospecific interaction of a chiral molecule with a magnetic substrate originates from the chiral induced spin selectivity (CISS) effect,[7-9] Because charge polarization of a chiral molecule's electron cloud is accompanied by a spin polarization,[10] an enantiospecific preference manifests when the spin polarized chiral molecule is aligned favorably with that of the magnetized substrate. In a racemic solution, the two enantiomers exhibit opposite spin polarizations upon charge polarization and hence interact differently with a magnetized surface. Later extensions of this phenomenon demonstrated enantioselective electrochemical reduction (and oxidation) of a racemate,[11-12] the generation of pure conglomerates,[13-14] and rate-dependent polymerization[15] on magnetized surfaces. Collectively, these studies illustrate that magnetic substrates and chiral molecules exhibit enantiospecific interactions which may be useful for enantioselective separation and synthesis.

Despite the remarkable proof-of-concept shown using CISS for enantiomeric resolution, a greater fundamental understanding of the principles which govern enantiospecificity at magnetic interfaces is required to assess the potential of this technique for real-world applications. This study uses an electrochemical quartz crystal microbalance (EQCM) method to examine the adsorption of the chiral amino acid cysteine on a magnetized ferromagnetic substrate. The experiments described herein show that the enantioselectivity for cysteine arises from kinetic effects, rather than thermodynamic differences, and that the adsorption process is the determining factor for successful enantioseparation. Moreover, these studies illustrate that the enenatiospecificity is sensitive to the molecular orientation and ionization state of the cysteine. The EQCM method thus provides a useful tool for identifying and optimizing the conditions for CISS-mediated chiral resolution.

2.2 Results and discussion

A scheme of the EQCM experimental method is shown in Figure 1a. The EQCM monitors the resonant frequency of a quartz crystal, which is coated with a metal film (100 nm Ni/10 nm Au) electrode, to quantify the adsorption and desorption of cysteine on the electrode surface as a function of electrode potential (and time).[16] During the experiment a 0.54 T magnet was used to magnetize the Ni film electrode; North (South) denotes the geometry in which the North (South) pole of the magnet was pointing toward the electrolyte and normal to the Ni film surface (See supplemental information for more details). Figure 1b shows EQCM data for a 1 μg/mL solution of L-cysteine in a pH 8 phosphate buffer. The top panel of 1b shows a cyclic voltammogram and the bottom panel shows the corresponding frequency change of the quartz crystal. Scanning the voltage cathodically reveals a current peak at -0.8 V and a concomitant frequency increase that corresponds to the reductive desorption of L-cysteine from the electrode surface. A subsequent anodic voltage scan reveals a broad current peak and concomitant decrease in the QCM frequency, which arise from the oxidative adsorption of L-cysteine onto the electrode. A similar behavior for alkanethiols on gold EQCM electrodes were shown previously.[17-18] The frequency shift of -1.0 Hz corresponds to a mass change of 1.4 ng, or ~7×10^12 cysteine molecules.

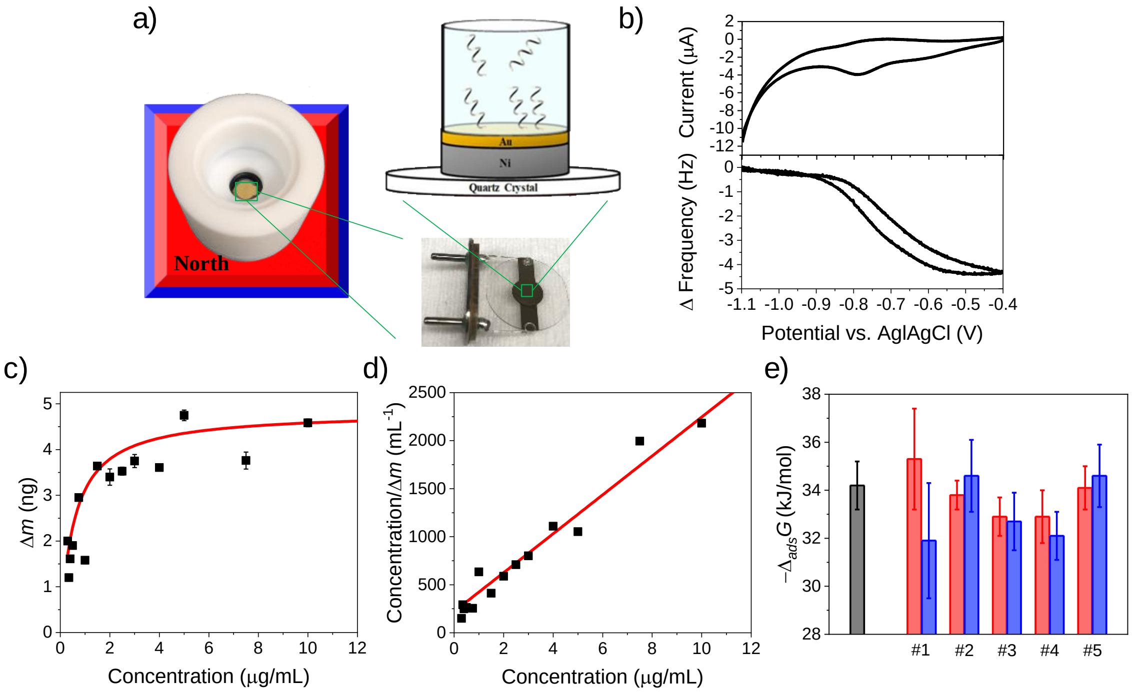

Figure 2.1 Panel a) shows an image and the scheme for the electrochemical quartz crystal microbalance (EQCM) measurements. A custom-made quartz crystal (100 nm Ni /10 nm Au) which is magnetized by a permanent magnet is used to monitor the adsorption of cysteine from solution. Panel b) shows a cyclic voltammogram (top) and corresponding frequency change (bottom) for the electrode in contact with a 10 µg/mL L-cysteine solution in pH 8 phosphate-buffer. Panel c) shows an adsorption isotherm of L-cysteine using the change in mass, Δm, from the EQCM measurements at different cysteine concentrations. The red line is a Langmuir isotherm fit to the data. Panel d) shows a linearized form of the data in panel c). Panel e) shows a histogram of the calculated $\Delta_{ads}G$ for different EQCM electrodes (#1 through #5) under North (red) and South (blue) applied magnetic field. Studies without a magnetic field on an Au electrode are shown in black. The error bars are associated with error in the linearized isotherm fit.

To elucidate the effect of Ni magnetization on the thermodynamics of cysteine adsorption, the change in mass, Δm, as a function of cysteine concentration, c_{cys}, from 0.25 µg/mL to 10 µg/mL, was monitored in a pH 8 phosphate buffer; see Figure 2.1c and d. The data were fit by a Langmuir adsorption model[19-20] to obtain a value of $\Delta_{ads}G$ (see Appendix A.3 & A.4). For $c_{cys} >$ 5 µg/mL the surface coverage of cysteine is largely saturated. Figure 2.1e shows a histogram plot of $\Delta_{ads}G$ for L-cysteine on different electrodes for different magnetization conditions; the height of the histogram gives the $\Delta_{ads}G$ values and the abscissa lists the trials using different EQCM electrodes. Note, the ordinate scale is expanded to make the error and variation in $\Delta_{ads}G$ more apparent. The average $\Delta_{ads}G$ for North (red) and South (blue) applied magnetization across the multiple trials is -33.8 ± 1.1 kJ/mol and -33.2 ± 1.5 kJ/mol, respectively. The $\Delta_{ads}G$ values determined under an applied magnetic field are in reasonable agreement for that on a nonmagnetic Au electrode (black, -34.2 ± 1.0 kJ/mol) and consistent with other literature reports.[21-22] These data indicate that the magnetic field orientation does not significantly change the $\Delta_{ads}G$ for L-cysteine. Similar experiments were performed for D-cysteine and found to be within error to those of L-cysteine; see Supplementary Information. Thus, the adsorption equilibrium does not change significantly with the molecules' handedness (D- versus L-forms) or the substrate magnetization direction.

Time-dependent QCM measurements, for different magnetization conditions of the electrode, were used to monitor the desorption and adsorption kinetics of cysteine. Based on the voltammogram (Figure 2.1b), the applied potential for desorption was set to be -0.8 V or more and that for adsorption of cysteine was set to be -0.5 V. The applied voltage was jumped between these two values and the QCM response was collected as a function of time after the potential jump. Small deviations from the set potentials caused little to no change in the time response. Figure 2.2 shows the observed QCM frequency response (black) upon application of the described voltage sequence (blue). A total of 150 cycles at the two different applied potentials was acquired and the QCM response for each 5 s time period were fit by an exponential profile to obtain the adsorption and desorption rate constants; see Appendix A.5& A.6 for more details. The fits to the desorption transient signals provide the desorption rate constant k_{des} directly; and the fits to the adsorption transients provide the effective adsorption rate constant k'_{ads}, which is given by $k'_{ads} = k_{ads} \cdot c_{cys}$ where k_{ads} is the adsorption rate constant (see Appendix A6 for more details). Figure 2.2 (right) shows histograms of k_{des} (top) and k'_{ads} (bottom) of a 1 μg/mL D-cysteine solution with a North (red) and South (blue) applied magnetic field. The bin size for the histograms is 0.1 s^{-1} for desorption and 0.05 s^{-1} for adsorption. The histograms were fit by a Gaussian distribution to obtain the average and standard deviation of the mean rate constant (values are reported in Table A.1). A significant dependence on the magnetization is observed for the D-cysteine adsorption process, the adsorption rate is higher for a South magnetized electrode than for a North magnetized electrode, whereas the desorption processes is more similar under the two different magnetizations.

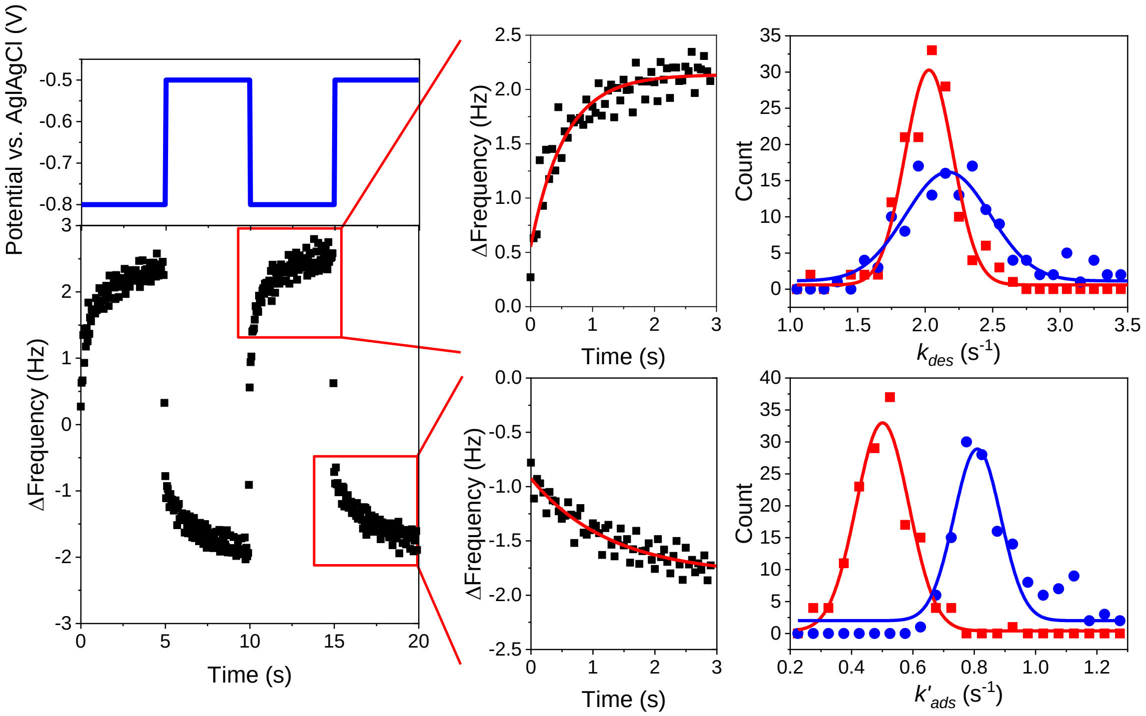

Figure 2.2 Chronoamperometry data (left) for a 1 μg/mL solution of D-cysteine. The applied potentials are shown in blue (top) and the frequency response is shown in black (bottom). The middle graphs show an expanded plot of the desorption (top) and adsorption (bottom) fits by an exponential decay or growth (red line) for determining the rate constant. The histograms on the right comprise >150 fits of the desorption (top) and

adsorption (bottom) processes under a North magnetic field (red) and South magnetic field (blue). A best fit of the data using a Gaussian distribution is shown as a solid line.

The adsorption kinetics of D-cysteine and L-cysteine were studied at a series of different concentrations from 1 μg/mL to 5 μg/mL (see Table A.1 and Figure A.3). The adsorption rate for L-cysteine displays a faster effective rate constant under North magnetization than it does under South magnetization, whereas the reverse is true for D-cysteine. The asymmetry in the adsorption rates and the inverse behavior of the enantiomers is consistent with a CISS mediated effect.**Error! Bookmark not defined.** To quantify the asymmetry, we define a polarization parameter, P as

$$P = \frac{k'_{ads,N} - k'_{ads,S}}{k'_{ads,N} + k'_{ads,S}} \cdot 100\%$$

Note that P corresponds closely to an enantiomeric excess *ee*. Figure 3 plots the experimentally determined P values as a function of L-cysteine (green) and D-cysteine (purple) concentration in Figure 2.3. Measurements with the achiral molecule mercaptopropionic acid (black) in solution gives a zero polarization. For L-cysteine, the polarization reaches a maximum value of 33.3% at 1 μg/mL and decreases to 4.6% at 5 μg/mL, whereas for D-cysteine the polarization is maximum at 1 μg/mL (−23.6%) and decreases to ~−2.3%% at 5 μg/mL. Solution concentrations of cysteine below 1 μg/mL resulted in mass changes that were too noisy to accurately fit and obtain kinetic information. These data demonstrate that the adsorption rate of D-cysteine and L-cysteine onto a ferromagnetic substrate depends on the magnetic field direction and the molecular handedness at low concentrations, however as the concentration of cysteine in the solution increases, the polarization in the adsorption kinetics decreases and becomes hard to discern. Thus, the enantioseparation of racemates reported by Banerjee-Ghosh *et al.*[6] is likely dictated by the adsorption kinetics.

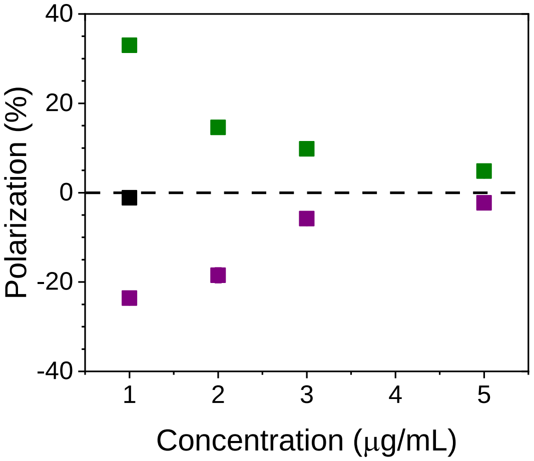

Figure 2.3 The polarization in adsorption rate constant for MPA (black), L-cysteine (green), and D-cysteine (purple) at different concentrations.

It is well known that solution conditions can affect cysteine's adsorption behavior. At intermediate pHs, where the zwitterionic form of cysteine exists, the binding geometry of cysteine has been shown to depend on the applied potential and scan rate; a process which changes under more acidic or basic conditions.[23-24] Cysteine can also dimerize to form cystine, a disulfide, in which the packing density and organization differ.[23] Also, Benesh *et al*. showed that the similar ionization constants for the nitrogen and sulfur moieties lead to charge isomerization.[25] Moreover, studies of chiral imprinting by organic ligands on nanoparticles have demonstrated that the handedness of the induced chirality can be strongly dependent on ligand packing and binding geometry.[26-28] In aggregate, these different phenomena illustrate the potential complexity of the substrate-cysteine interaction during adsorption, which could impact the observed P values; e.g., the molecular adsorption of cysteine rotamers[29-30] could give rise to opposite P values.

Figure 2.4 shows measurements of P for 1 μg/mL solutions of L-cysteine and L-cysteine methyl ester as a function of the solution pH. For cysteine (Figure 2.4a), P is large and positive at pH 8 (33%), but quickly transitions to a negative value as the pH increases to 8.56 (−15%) before asymptotically decreasing toward zero as the pH becomes large; see Table A.2 for the rate constants. The crossover from positive to negative polarizations is concomitant with the $pK_a = 8.3$ of the sulfur moiety of cysteine in solution[31] and suggests that the enantiospecificity is sensitive to the geometry and structure of the adsorbate. This inference is substantiated by the data for L-cysteine methyl ester which has a $pK_a = 6.6$ for its thiol group.[31] Figure 2.4b, shows that P for the methyl ester form is strongly negative at pH 6.6, but increases to ~7% at pH 7 before falling asymptotically toward zero at pH 10. Interestingly, P for cysteine methyl ester is negative at low pH whereas P for cysteine itself is positive at low pH. We posit that this behavior is rooted in the charge state of the adsorbate. Indeed, previous studies have shown that the charge polarization of a chiral molecule is linked to its CISS response;**Error! Bookmark not defined.**,[32-33] however a more elaborate investigation involving different cysteine derivatives is required to better understand this effect. The pH studies illustrate the important need to understand how solution conditions and adsorbate ionization state can impact its enantiospecific adsorption, if it is to be used for separations.

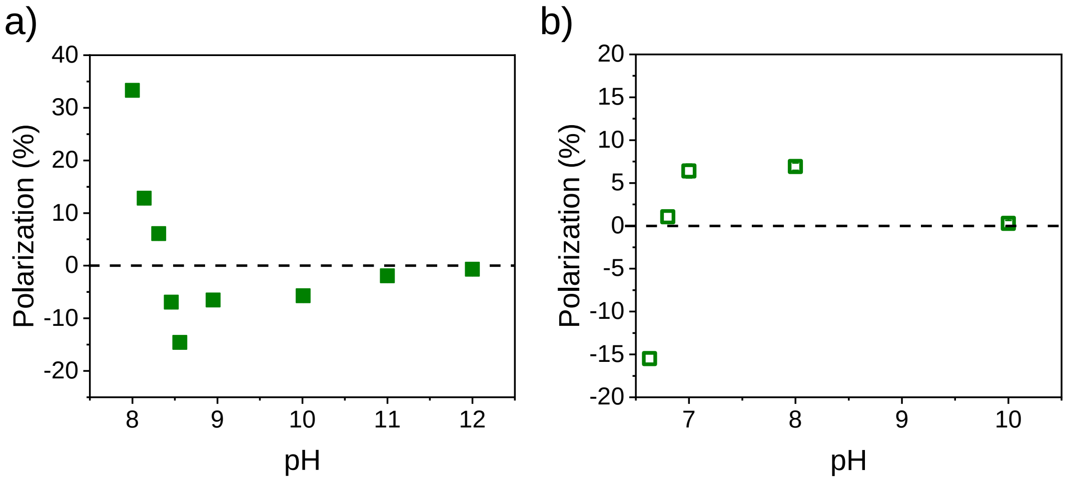

Figure 2.4 The polarization is plotted as a function of the solution pH for L-cysteine (panel a) and L-cysteine methyl ester (panel b).

2.3 Conclusion

This work shows that the enantiospecific interaction of cysteine with a magnetized ferromagnetic substrate is kinetically controlled and depends sensitively on the solution conditions (ionization state of the cysteine). Measurements of the adsorption isotherm show that the Gibbs free energy of adsorption $\Delta_{ads}G$ on an Au coated ferromagnetic electrode does not change with the cysteine chirality or the electrodes magnetization state. In contrast, the kinetics for the adsorption show a significant dependence on the magnetic field direction and the handedness of the molecule. Concentration and pH studies of the adsorption polarization reveal the importance of molecular binding geometry for successful enantiomeric resolution.

2.4 Reference

1.Williams, K.; Lee, E., Importance of drug enantiomers in clinical pharmacology. *Drugs* **1985,** *30* (4), 333-354.

2.Garrison, A. W.; Schmitt-Kopplin, P.; Avants, J. K., Analysis of the enantiomers of chiral pesticides and other pollutants in environmental samples by capillary electrophoresis. In *Capillary electrophoresis*, Springer: 2008; pp 157-170.

3.Nguyen, L. A.; He, H.; Pham-Huy, C., Chiral drugs: an overview. *International journal of biomedical science: IJBS* **2006,** *2* (2), 85.

4.Okamoto, Y.; Ikai, T., Chiral HPLC for efficient resolution of enantiomers. *Chemical Society Reviews* **2008,** *37* (12), 2593-2608.

5.Ward, T. J.; Ward, K. D., Chiral separations: fundamental review 2010. *Analytical chemistry* **2010,** *82* (12), 4712-4722.

6.Banerjee-Ghosh, K.; Dor, O. B.; Tassinari, F.; Capua, E.; Yochelis, S.; Capua, A.; Yang, S.-H.; Parkin, S. S.; Sarkar, S.; Kronik, L., Separation of enantiomers by their enantiospecific interaction with achiral magnetic substrates. *Science* **2018,** *360* (6395), 1331-1334.

7.Naaman, R.; Paltiel, Y.; Waldeck, D. H., Chiral induced spin selectivity gives a new twist on spin-control in chemistry. *Accounts of Chemical Research* **2020,** *53* (11), 2659-2667.

8.Naaman, R.; Paltiel, Y.; Waldeck, D. H., Chiral molecules and the spin selectivity effect. *The journal of physical chemistry letters* **2020,** *11* (9), 3660-3666.

9.Naaman, R.; Paltiel, Y.; Waldeck, D. H., Chiral molecules and the electron spin. *Nature Reviews Chemistry* **2019,** *3* (4), 250-260.

10.Ghosh, S.; Mishra, S.; Avigad, E.; Bloom, B. P.; Baczewski, L. T.; Yochelis, S.; Paltiel, Y.; Naaman, R.; Waldeck, D. H., Effect of Chiral Molecules on the Electron's Spin Wavefunction at Interfaces. *The Journal of Physical Chemistry Letters* **2020,** *11* (4), 1550-1557.

11.Bloom, B.; Lu, Y.; Metzger, T.; Yochelis, S.; Paltiel, Y.; Fontanesi, C.; Mishra, S.; Tassinari, F.; Naaman, R.; Waldeck, D., Asymmetric reactions induced by electron spin polarization. *Physical Chemistry Chemical Physics* **2020**.

12.Metzger, T. S.; Mishra, S.; Bloom, B. P.; Goren, N.; Neubauer, A.; Shmul, G.; Wei, J.; Yochelis, S.; Tassinari, F.; Fontanesi, C., The Electron Spin as a Chiral Reagent. *Angewandte Chemie International Edition* **2020,** *59* (4), 1653-1658.

13.Tassinari, F.; Steidel, J.; Paltiel, S.; Fontanesi, C.; Lahav, M.; Paltiel, Y.; Naaman, R., Enantioseparation by crystallization using magnetic substrates. *Chemical science* **2019,** *10* (20), 5246-5250.

14.Bhowmick, D.; Sang, Y.; Santra, K.; Halbauer, M.; Capua, E.; Paltiel, Y.; Naaman, R.; Tassinari, F., Simultaneous High-Purity Enantiomeric Resolution of Conglomerates Using Magnetic Substrates. *Crystal growth & design* **2021,** *21* (5), 2925-2931.

15.Tassinari, F.; Amsallem, D.; Bloom, B. P.; Lu, Y.; Bedi, A.; Waldeck, D. H.; Gidron, O.; Naaman, R., Spin-dependent enantioselective electropolymerization. *The Journal of Physical Chemistry C* **2020,** *124* (38), 20974-20980.

16.King, W. H., Piezoelectric sorption detector. *Analytical Chemistry* **1964,** *36* (9), 1735-1739.

17.Qu, D.; Morin, M., An EQCM study of the oxidative deposition of alkylthiolates on gold. *Journal of Electroanalytical Chemistry* **2001,** *517* (1-2), 45-53.

18.Qu, D.; Morin, M., The kinetics of the electroformation of a self-assembled monolayer of butanethiols on gold. *Journal of Electroanalytical Chemistry* **2002,** *524*, 77-80.

19.Adamson, A., Physical Chemistry of Surfaces, 5th edn Wiley. *New York* **1990**.

20.Swenson, H.; Stadie, N. P., Langmuir’s theory of adsorption: A centennial review. *Langmuir* **2019,** *35* (16), 5409-5426.

21.Yang, W.; Gooding, J. J.; Hibbert, D. B., Characterisation of gold electrodes modified with self-assembled monolayers of L-cysteine for the adsorptive stripping analysis of copper. *Journal of Electroanalytical Chemistry* **2001,** *516* (1-2), 10-16.

22.Hager, G.; Brolo, A. G., Adsorption/desorption behaviour of cysteine and cystine in neutral and basic media: electrochemical evidence for differing thiol and disulfide adsorption to a Au (1 1 1) single crystal electrode. *Journal of Electroanalytical Chemistry* **2003,** *550*, 291-301.

23.Brolo, A. G.; Germain, P.; Hager, G., Investigation of the adsorption of L-cysteine on a polycrystalline silver electrode by surface-enhanced Raman scattering (SERS) and surface-enhanced second harmonic generation (SESHG). *The Journal of Physical Chemistry B* **2002,** *106* (23), 5982-5987.

24.Hager, G.; Brolo, A. G., Protonation and deprotonation of cysteine and cystine monolayers probed by impedance spectroscopy. *Journal of Electroanalytical Chemistry* **2009,** *625* (2), 109-116.

25.Benesch, R. E.; Benesch, R., The acid strength of the-SH group in cysteine and related compounds. *Journal of the American Chemical Society* **1955,** *77* (22), 5877-5881.

26.Kuznetsova, V. A.; Mates-Torres, E.; Prochukhan, N.; Marcastel, M.; Purcell-Milton, F.; O'Brien, J.; Visheratina, A. K.; Martinez-Carmona, M.; Gromova, Y.; Garcia-Melchor, M., Effect of chiral ligand concentration and binding mode on chiroptical activity of CdSe/CdS quantum dots. *ACS nano* **2019,** *13* (11), 13560-13572.

27.Choi, J. K.; Haynie, B. E.; Tohgha, U.; Pap, L.; Elliott, K. W.; Leonard, B. M.; Dzyuba, S. V.; Varga, K.; Kubelka, J.; Balaz, M., Chirality inversion of CdSe and CdS quantum dots without changing the stereochemistry of the capping ligand. *ACS nano* **2016,** *10* (3), 3809-3815.

28.Bloom, B. P.; Graff, B. M.; Ghosh, S.; Beratan, D. N.; Waldeck, D. H., Chirality control of electron transfer in quantum dot assemblies. *Journal of the American Chemical Society* **2017,** *139* (26), 9038-9043.

29.Harding, M. t.; Long, H., The crystal and molecular structure of L-cysteine. *Acta Crystallographica Section B: Structural Crystallography and Crystal Chemistry* **1968,** *24* (8), 1096-1102.

30.Noszál, B.; Visky, D.; Kraszni, M., Population, acid− base, and redox properties of N-acetylcysteine conformers. *Journal of medicinal chemistry* **2000,** *43* (11), 2176-2182.

31.Burner, U.; Obinger, C., Transient-state and steady-state kinetics of the oxidation of aliphatic and aromatic thiols by horseradish peroxidase. *FEBS letters* **1997,** *411* (2-3), 269-274.

32.Kumar, A.; Capua, E.; Kesharwani, M. K.; Martin, J. M.; Sitbon, E.; Waldeck, D. H.; Naaman, R., Chirality-induced spin polarization places symmetry constraints on biomolecular interactions. *Proceedings of the National Academy of Sciences* **2017,** *114* (10), 2474-2478.

33.Fransson, J., Charge redistribution and spin polarization driven by correlation induced electron exchange in chiral molecules. *Nano letters* **2021,** *21* (7), 3026-3032.

3.0 Spin-based chiral separations and the importance of molecule-solvent interactions

This work was published as Lu, Y., Qiu, T., Bloom, B. P., Subotnik, J. E., Waldeck, D. H. *The Journal of Physical Chemistry C*, **2023**. The author of the dissertation performed the design of the experiments, the electrochemical quartz crystal microbalance measurement, optical measurements, data analysis and participated in writing the manuscript. The supporting information for this chapter can be found in Appendix B.

This work uses magneto-electrochemical quartz crystal microbalance methods to study the enantiospecific adsorption of chiral molecules onto a ferromagnetic substrate. The effect of solution conditions, pH and solvent isotope composition, indicate that the kinetics of the enantiomeric adsorption depend strongly on the charge state and geometry of the adsorbate, whereas no thermodynamic contributions to enantiospecificity are found. Density functional theory calculations reveal that an interplay between the adsorbate and solvent molecules is important for defining the observed enantiospecific preference with an applied magnetic field, however it remains unclear if intermolecular vibrational couplings contribute to the phenomenon.

3.1 Introduction

The chiral induced spin selectivity (CISS) effect refers to the fact that chiral molecules and chiral materials (even if they are closed shell) display spin-dependent electronic responses. Early work on CISS emphasized the preference for electron propagation of a given spin through a chiral molecule with a given handedness.[1-3] However, the discovery that charge polarizing chiral molecules gives rise to a net spin polarization,[4] expands the implications and possible applications of CISS beyond that of simple spin filtering. For instance, Banerjee-Ghosh *et al.* showed that chiral molecules exhibit enantiospecific interactions with a magnetized ferromagnetic substrate and this process can be used for enantioselective separation from racemic solutions.[5] More recently, Safari *et al.*[6] showed that the enantiospecific adsorption could occur at single molecule level in ultra-high vacuum condition. In related work, we, and others, have leveraged the enantiospecific interactions of chiral molecules with ferromagnetic substrates to perform electrochemically driven enantioselective redox reactions,[7-9] to separate racemic solutions through substrate-driven crystallization,[10-11] and to affect the helicity of polymers during electropolymerization.[12-13]

In our previous work,[14] magnetic electrochemical quartz crystal microbalance (EQCM) methods revealed that the enantiospecific adsorption of L- and D-cysteine on a magnetized ferromagnetic substrate is a kinetically controlled process rather than a thermodynamic one under ambient conditions. In addition, the enantiospecificity was found to depend strongly on the solution pH conditions. Because the binding geometry and ionization state of the molecule changes with pH,[15] the variations in selectivity were hypothesized to arise from changes in the adsorbate's binding geometry. Indeed, Clever *et al.*[16] have recently demonstrated the importance of molecular dipole moments in controlling the sign of the polarization in CISS-based measurements on oligopeptides, underscoring the importance of a molecule's dipole moment direction relative to the surface. In other work, Tassinari *et al.*[11] showed that D-asparagine (L-asparagine) preferentially crystallized on a ferromagnetic substrate with application of a North (South) magnetic field while the enantiopreference was reversed for glutamic acid; L-glutamic acid preferentially crystalized on a ferromagnetic substrate with a North magnetic field and D-glutamic acid with a South magnetic field. These studies indicate that the enantiopreference is sensitive to the interaction conditions between the molecule and substrate and thus may vary on a molecule-to-molecule basis. That being said, not all studies have shown enantiospecific adsorption on ferromagnetic surfaces; Radetic *et al.*[17] did not observe an enantiopreference in the adsorption of D- and L-aspartic acid on magnetized Ni (100) surfaces under ultra-high vacuum conditions. To fully exploit spin-mediated enantiospecificity for guiding chemical reactions, separations, and other processes, it is clear that a more rigorous understanding of the physical properties which dictate enantioselectivity must be made. In particular, one essential question that remains unresolved is the effect of nuclear vibrations on spin selectivity as encapsulated through non-Born Oppenheimer Berry forces; calculations on model Hamiltonians[18] have suggested that such effects can be substantial as far as promoting CISS even with small spin-orbit couplings, but such calculations have not yet been run on realistic systems or Hamiltonians.

In this work, the enantiospecific adsorption of cysteine and N-acetyl cysteine methyl ester on a magnetized ferromagnetic substrate in H_2O and D_2O solutions was investigated and found to correlate with the geometry of the adsorbate on the substrate, the adsorbate's ionization state (as determined by its pKa value), and the solution conditions. Density-functional theory (DFT) calculations corroborate these findings by revealing the importance of solvent interactions for achieving large differences in the adsorption kinetics of a pair of enantiomers.

3.2 Results and Discussion

The effective adsorption rate of cysteine under different magnetization states (North versus South) was measured using time-dependent magnetic EQCM measurements, as described in our previous work;[14] see Figure 3.1A for a scheme of the experimental method and method section for additional experimental details. Briefly, a quartz crystal was coated with a 100 nm Ni /10 nm Au film and used as the working electrode in a three-electrode electrochemical cell. The potential of the working electrode was varied, causing adsorption and desorption of the chiral molecule adlayer, and the time-dependent frequency response of the quartz crystal was recorded to quantify the mass change. A 0.54 T permanent magnet was placed underneath the quartz crystal for the entirety of the experiment to magnetize the electrode (see Figure 3.1A; North (South) denotes which magnetic pole is pointing toward the electrolyte along the normal to the Ni film's surface). The effect of the magnetization direction on the adsorption kinetics was then monitored. Figure 3.1B shows a graphical representation of the potential sequence (top), and the resulting change in frequency recorded by the quartz crystal (bottom) used for cysteine; the potential was cycled between -0.8 V, to initiate cysteine desorption, and -0.5 V, to induce adsorption, in 5s intervals. The frequency response within the first 3 s for each desorption (top) and adsorption (bottom) process is shown in Figure 3.1C and then fit to an exponential growth or decay (red line). The time constant generated from the fit was then used to calculate an effective adsorption rate constant, k'_{ads}, and a histogram of the rates from >150 adsorption events was compiled. The histograms were then fit by a Gaussian distribution to obtain an average k'_{ads} and standard deviation. Figure 3.2A shows representative histograms for 8 μM D-cysteine in a pH 8 buffer solution in H_2O, under North (red) and South (blue) applied magnetic fields. The difference in peak positions of the Gaussian distributions shows the significant dependence of the adsorption of D-cysteine on the magnetization state of the electrode.

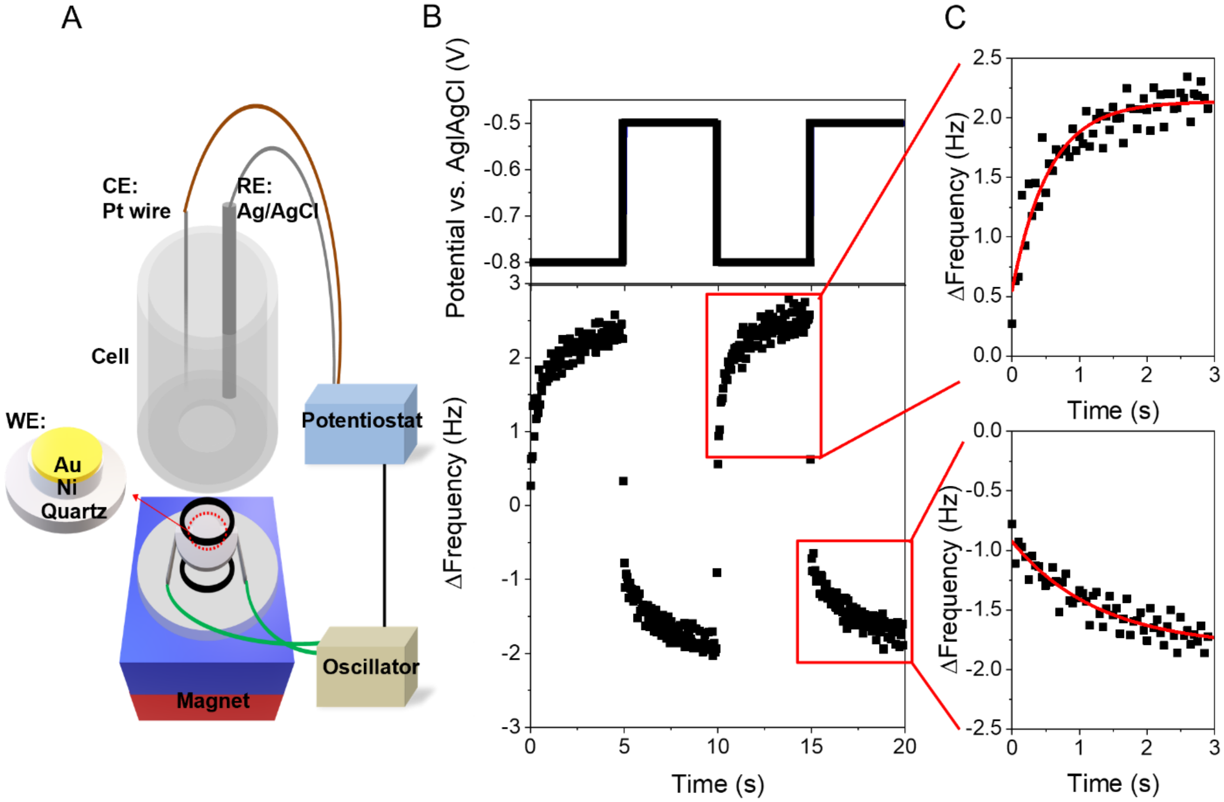

Figure 3.1 (A) Illustration of the EQCM setup in which a permanent magnet is placed underneath the quartz crystal electrode during measurements. The inset shows a zoomed in rendering of the working electrode composition. (B) Representative chronoamperometry potential sequence (top) and corresponding frequency response of the quartz crystal electrode (bottom) used for an 8 µM solution of D-cysteine in a pH 8 buffer solution. (C) Expanded plot of the frequency response upon desorption (top) and adsorption (bottom) of D-cysteine. The red line is an exponential fit to the data used for extracting the effective rate constants.

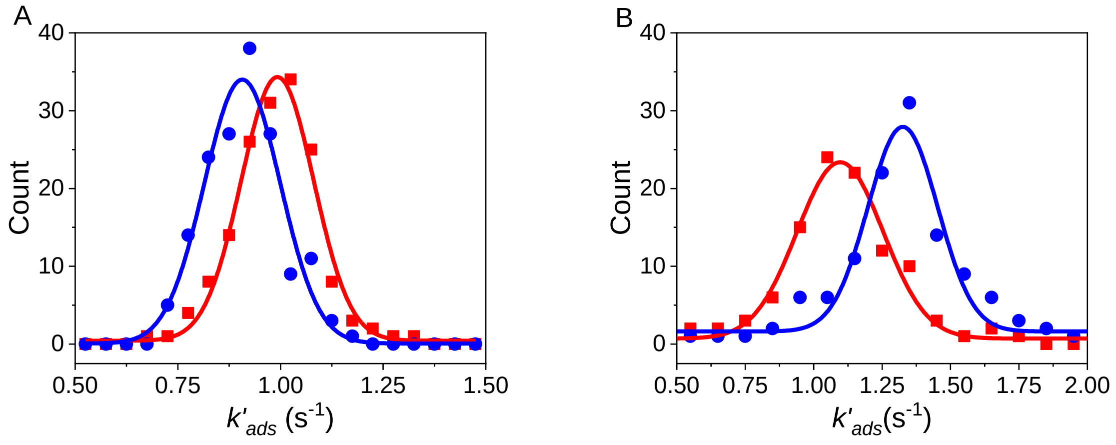

Figure 3.2 Histogram of the effective adsorption rate constant of an 8 μM D-cysteine under a North magnetic field (red) and a South magnetic field (blue) in H_2O (A) and D_2O (B) at pH* = 8.5. A best fit to the data using a Gaussian distribution is shown by a solid line.

To experimentally explore the importance of vibrational contributions, a solution isotope dependence on the adsorption behavior of cysteine was investigated. Figure 3.2 shows histograms of k'_{ads} for 8 μM D-cysteine in H_2O (A) and D_2O (B) at pH* = 8.5, where pH* represents the reading from a pH meter. Thus, the pH in H_2O is the same as pH*, but the pD in D_2O is calculated by pH* + 0.45 in accordance with established protocols[19]. Interestingly, for pH* = 8.5, k'_{ads} of D-cysteine is higher for a North magnetized electrode (red) than for a South magnetized electrode (blue) in H_2O, however the opposite is true in D_2O; k'_{ads} is higher (lower) for a South (North) magnetized electrode.

To determine if the difference in adsorption behavior with solvent is rooted in a thermodynamically driven process, the Gibbs free energy for the adsorption of cysteine, $\Delta_{ads}G$, in D_2O was measured; see Figure B.3 and corresponding discussion. The average $\Delta_{ads}G$ of D-cysteine with a North magnetic field was -34.2 ± 1.4 kJ and for a South magnetic field was -34.6 ± 1.3 kJ, whereas the average $\Delta_{ads}G$ for L-cysteine was -34.0 ± 1.1 kJ and -34.2 ± 1.0 kJ with a North and South magnetic field, respectively. These results are consistent with the $\Delta_{ads}G$ of D- and

L-cysteine in H_2O, reported in our previous work[14] and indicate that the solvent isotope does not significantly affect the thermodynamics of cysteine adsorption at pH* = 8.5. To further explore the effect of isotope and solution conditions on k'_{ads}, a series of different pH/pD were measured. The difference between the effective rate constant under North and South magnetization were quantified through a polarization parameter, P, defined as

$$P = \frac{k'_{ads,N} - k'_{ads,S}}{k'_{ads,N} + k'_{ads,S}} \cdot 100\%$$

where $k'_{ads,N}$ and $k'_{ads,S}$ correspond to the adsorption rate constant under North and South applied magnetic fields, respectively.

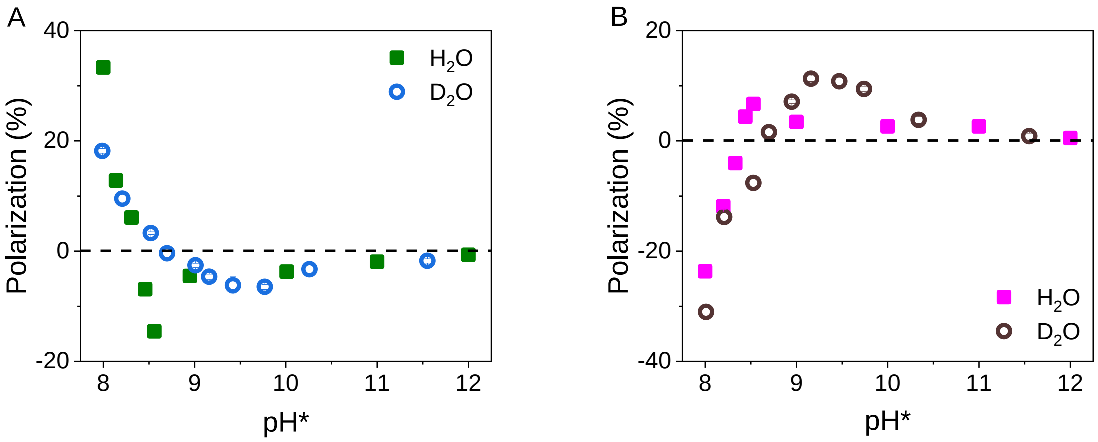

Figure 3.3 Polarization in adsorption rate constant in different pH* solutions. L-cysteine (A) in H_2O (green square) and D_2O (blue circle) and D-cysteine (B) in H_2O (purple square) and D_2O (brown circle).

Figure 3.3 shows P for solutions of 8 μM L-cysteine (Panel A) and D-cysteine (Panel B) in H_2O (squares) and D_2O (circles) as a function of pH*. The L-cysteine and D-cysteine enantiomers display an opposite sign in the polarization at each pH* in both H_2O and D_2O solutions. The asymmetry in adsorption rates, as well as the inverse behavior of the enantiomers, is consistent with a CISS-mediated phenomenon.[20] In H_2O at pH = 8, the P is large and positive (33%) for L-cysteine, whereas the P is large and negative (-24%) for D-cysteine. As the pH is increased, the P

for both L- and D-cysteine quickly transition to an opposite sign, reaching -15.6% for L-cysteine and 6.7% for D-cysteine at pH = 8.6, then decrease to zero at high pH. In D_2O at pH* = 8, *P* for both L- and D-cysteine have a maximum value (18.5% and -31% respectfully), then gradually transition to a *P* with the opposite sign, reaching a maximum value at ~pH* = 9.3 (-6.9% for L-cysteine and 13.8% for D-cysteine), then decrease to zero as the pH* is increased farther. The crossover of the *P* for both D- and L-cysteine in H_2O occurs at around pH* = 8.3, while in D_2O it shifts to a higher pH* value, ~ 8.6 (corresponding to pD = 9.05). The two crossover points correlate with the solvent-dependent pKa value of the sulfur moiety of cysteine; ~8.3 and ~8.9 in H_2O and D_2O, respectively.[21-23]

Although the form of the polarization versus pH* curves are qualitatively the same in H_2O and D_2O, the *P* value undergoes a much sharper crossover at the thiol pKa value in H_2O than in D_2O. This change in shape may arise from the tautomerization equilibria involving sulfhydryl groups, which are subject to an inverse solvent deuterium isotope effect,[23] whereby the zwitterion is preferentially stabilized in D_2O relative to H_2O -- as reflected in a larger pKa window between pK_{12} and pK_{13} in D_2O relative to H_2O; see Scheme 3.1. When the pH is greater than 8.7 in H_2O, or pD is greater than 9.6 in D_2O, the non-zwitterionic form of cysteine dominates. Compared to the zwitterionic form of cysteine, the non-zwitterionic form has a smaller dipole moment,[24] which may result in a smaller CISS response, effectively decreasing the polarization.[25] Thus, the differences in cysteine pKa values could explain differences in polarization for H_2O and D_2O at pH* = 8.5 in Figure 3.2; the dramatic crossover for H_2O compared to the elongated crossover in D_2O creates differences in the sign of the *P* at intermediate pH*. That being the case, this hypothetical situation is almost certainly more complicated on the electrode surface, where due to the electrical double layer and the reduced mobility of the solvent molecules, the local electric field and geometries play important roles. In particular, our simulations below suggest that the proton from the thiol group is activated when S binds to the Au surface, and a stable local solvation ring structure is formed with this proton participated. In this sense, Scheme 3.1 is understood as a measure of species in the solution where the adsorbates on the surface is in equilibrium with but does not necessarily represent the adsorbates themselves.

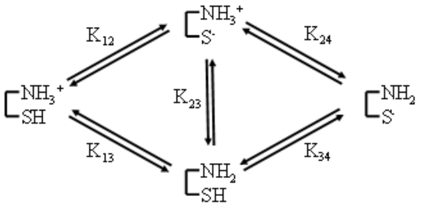

	pK_{12}	pK_{13}	pK_{24}	pK_{34}
H_2O	8.3	8.7	11.0	10.6
D_2O	8.9	9.6	11.5	10.8

Scheme 3.1 The general ionization scheme (left) and a table of ionization constants (right) for cysteine in H_2O and D_2O. The data are taken from reference[21, 23, 26]

Previous research[5-6] indicates that the CISS properties of a molecule are often dictated by the enantiomer under investigation and correlate strongly with the sign and magnitude of a molecule’s circular dichroism (CD) spectrum, yet our experiments reveal that a change in polarization is observed for the same molecule under different pH* conditions. To ensure that a change in the handedness of the molecule is not responsible for the different CISS responses, CD spectra of L- and D-cysteine were measured under different pH* conditions; see Figure B.5. While the CD intensity decreases and the peak modestly red shifts as pH* increases, the sign of the CD signal does not change. Thus, we conclude that the change in polarization must arise from changes in the surface-cysteine interaction at different pH* rather than any interconversion or racemization of the cysteine enantiomers.

The geometry and packing density of chiral organic ligands on nanoparticle surfaces have been shown in previous works to affect the resulting chirality of the nanomaterial [27-29]and therefore we posit that a similar mechanism could give rise to the changes in polarization with pH* here. From the form of the Rosenfeld equation, which relates the rotatory strength to a product of the electronic and magnetic transition dipole moments,[30] it is clear that the chiroptical response of the cysteine adsorbate and its electronic imprint on the metal substrate can change with adsorbate configuration. Given the low signal-to-noise, experimental CD spectra could not be obtained. While a theoretical determination of the pH dependent chiroptical response of an adsorbate on a metal surface is possible in principle, it requires a significant development of DFT (or even better, TD-DFT) methods to be accurate enough and is beyond the scope of the current work.[31] Instead, differences in the geometry of the cysteine adsorbates on the surface were modeled using DFT and correlated with the data.

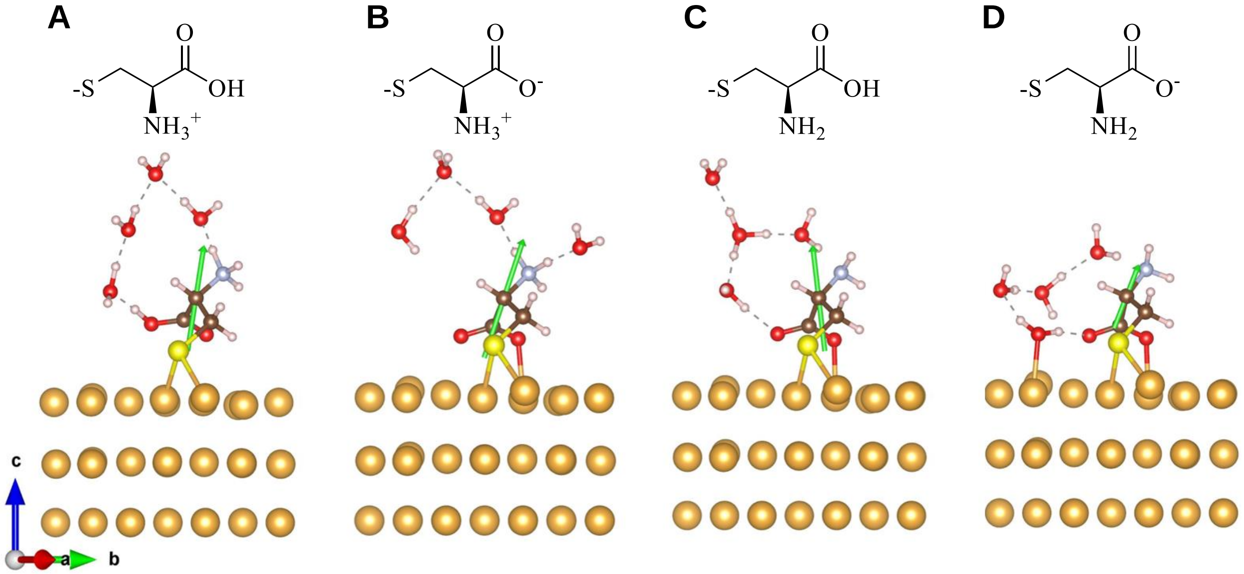

Figure 3.4 Adsorbate geometries and corresponding dipole moments (green arrow) are shown for DFT calculations determining the most energetically favorable adsorption geometries of an L-cysteine molecule on the surface of Au(111) in H_2O. The red, gray, brown, and white spheres indicate oxygen atoms, nitrogen atoms, carbon atoms, and hydrogen atoms, respectively. Panel A shows the zwitterionic form of cysteine with a deprotonated thiol group; panel B shows a thiolate bound form of zwitterionic cysteine; panel C shows a tautomer of the species in panel B; and panel D shows a thiolate bound anionic form of cysteine.

While the gold used in this study is considered polycrystalline, it is important to note that the predominantly exposed facet is Au(111); see Figure B9 and corresponding discussion in appendix B.6 for more details. Now, as discussed above, it would appear that our results are sensitive to pH because changing pH implies deprotonating the SH group, and yet in practice, the SH can always deprotonate at a metal surface. Nevertheless, from the data, it would appear that multiple charge states are visited during the course of the experiment. Furthermore, it seems unlikely that, at the pH's and voltage studied here, the cysteine moiety ever has more than a (-2) charge. Therefore, in our simulations below, we will allow for the possibility that the COO group (which is normally deprotonated) can in fact accept be neutral and protonated at a metal surface, where solvation is more difficult to achieve because of sterics and the Au-S bond generates protons. Figure 4 shows the optimized geometry of the four possible ionization states of cysteine, between pH 8 and 12, in the presence of H_2O on a Au (111) surface. The geometries of the cysteine adsorbate (neglecting solvent) of the four ionization states are all very similar, however the distance between the carboxyl group and the Au surface in panel A differs substantially from that of the other three states (panels B, C, and D); see Table 3.1 for the distance of the carboxyl group's oxygen to the gold surface. The structure in panel A shows a strong interaction between the cysteine and the solvent molecules as well, which gives rise to a ring-like system of four H-bonded water molecules. As the ionization state changes, analogous to increasing the pH of the solution, the water molecules in cysteine's first solvation shell reorganize, causing the ring system to begin to break down.

Table 3.1 Closest distance between the oxygen in the carboxyl group to the Au surface.

	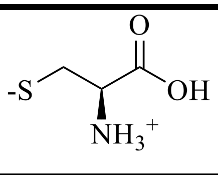	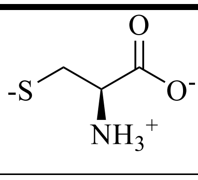	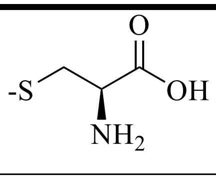	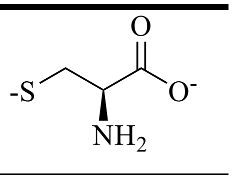
Distance (Å)	2.66	2.26	2.22	2.21

Table 3.2 The projection of the magnitude of dipole moment in Cartesian coordinates x, y, and z direction for different adsorption configurations of L-cysteine. Note that the lattice vector a, b, and c of the simulation cell constitute a 60° hexagonal cell with a in x direction and c in z direction.

	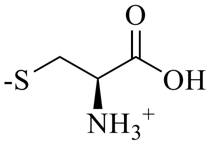	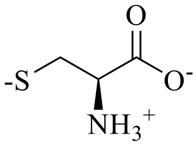	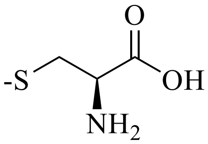	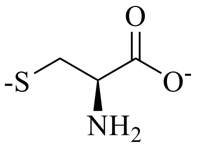
x	4.46	3.50	0.45	2.95
y	1.14	6.67	-3.02	3.92
z	20.69	22.68	20.77	12.52

The change in geometric structure and hydrogen bonding network correlate with the change in the sign of *P* shown in Figure 3. Consider the case of L-cysteine; at pH 8, the adsorption configuration is that of panel A in Figure 3.4. Because of the formation of the stable 4-H_2O ring between the carboxyl group and the amine group, the carboxyl group interacts only weakly with the Au substrate giving rise to the highest polarization value. As the pH increases, however, the population of adsorbate geometries shifts from that of panel 3.4A to that of panel 3.4B and the polarization switches sign (goes from positive to negative). In this pH range, the adsorbed cysteine is zwitterionic and its binding geometry changes significantly, which increases and rotates the molecule’s dipole moment. The ring structure is partially destroyed, the carboxyl group loses its strong interaction with the solvent and instead interacts with the Au substrate. Presumably, these structural and electrostatic changes correlate with changes in the molecule’s chiral imprint on the surface such that the polarization value becomes more negative. As the pH further increases, the adsorbate structures in panels 3.4C and 3.4D become more important, the dipole moment decreases (Table 3.2), the ring structure is distorted, and the carboxyl group interacts more strongly with the Au substrate. Presumably, the distribution of adsorption conformations is such that no significant net polarization is found at high pH and the *P* gradually decreases back to zero. The drop of out-of-plane dipole moment magnitude in panel 3.4D (also the last column in Table 3.2) is caused by the absence of a positive charge center and hence a weaker charge separation arises, as compared with the other three states (panel 3.4A, 3.4B, and 3.4C). The out-of-plane dipole moment direction, however, does not change (i.e., points along the surface normal) through the whole process, which indicates that the sign change in polarization does not arise from the dipole moment direction but some other effect of the change in binding geometry. Substituting D_2O for H_2O in the calculations does not change the ionization state dependent structural geometry of the cysteine adsorbate or the H-bonding network (D-bonding network for D_2O) significantly. The higher mass for the deuterated solvent is known to affect the manifold of vibrational states, i.e., intermolecular vibrational couplings are more important for H_2O than for D_2O with a subsequent increase in vibrational energy relaxation.[32-33] While solvent isotope may affect the strength of coupling between solvent molecules and cysteine, discernable differences in the magnitude of *P* for H_2O and D_2O are lacking which suggests these effects are too weak to elicit a change under the current experimental conditions.

The effect of solvent interactions and ionization state on *P* were further explored through experimental studies using N-acetyl-L-cysteine methyl ester as the adsorbate in H_2O and D_2O solutions. Note, that the carboxylate and the amino groups are both blocked from protonation and their hydrogen bonding interaction with the solvent is weaker; only the thiol group can be deprotonated and its pKa in solution is ~8.5.[34] Figure 3.5 shows the *P* for 8 μM solutions of N-acetyl-L-cysteine methyl ester in H_2O (green, squares) and D_2O (blue, circles) as a function pH*. When pH* = 7, the polarization has a positive value of ~10% in both H_2O and D_2O; and as the pH* increases to ~8.5 the polarization gradually decreases to around 0. In contrast to L- and D-cysteine, the *P* for N-acetyl-L-cysteine methyl ester does not change sign as pH* increases past the pKa associated with deprotonation of the sulfur. In addition, no discernable differences in the *P* for H_2O and D_2O solutions are evident, i.e., no solvent isotope effect manifests. Figure 6 shows corresponding DFT calculations for the two different possible ionization states of N-acetyl-L-cysteine methyl ester; *i.e*., before and after deprotonation. The optimized geometries show that similar to cysteine adsorbed on the Au surface, the proton from the thiol group of N-acetyl-L-cysteine methyl ester dissociates and bonds to an intra-molecular oxygen before the deprotonation. Nevertheless, no specific local solvation structure changes are observed in the deprotonation process, suggesting a weaker interaction to the solvent, interestingly coincide with a smaller magnitude for the polarization than that of cysteine and no obvious difference between H_2O and D_2O.

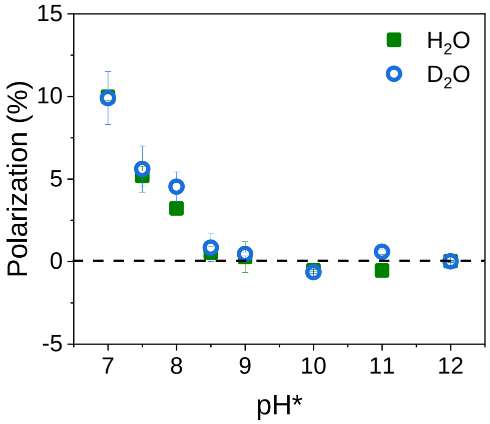

Figure 3.5 Polarization in adsorption rate constant of N-acetyl-L-cysteine methyl ester in H_2O (green square) and D_2O (blue circle) at different pH* values.

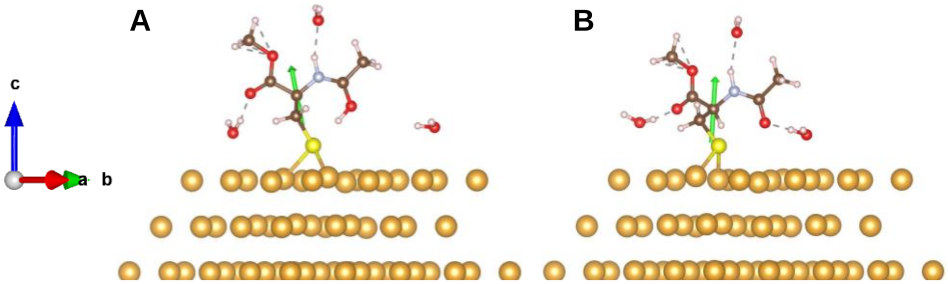

Figure 3.6 DFT calculations for the most stable adsorption geometry of N-acetyl-L-cysteine methyl ester in H2O on Au. The red, gray, brown, and white spheres correspond to oxygen, nitrogen, carbon, and hydrogen atoms, respectively. Panel A: before the deprotonation of sulfur; panel B: after the deprotonation of sulfur.

3.3 Conclusion

This work uses a combination of electrochemistry experiments and DFT calculations to examine the effects of geometric structure, ionization state, dipole orientation, and molecule-solvent interactions on the enantiospecific adsorption of chiral molecules on magnetized ferromagnetic surfaces. Our studies suggest that geometric changes in the adsorbate, brought on by changes in the solution pH, are responsible for changes in the preferred substrate magnetization that is observed for the adsorption of L-cysteine. While DFT calculations suggest that solvent interactions may be important, solvent isotope studies imply that solvent vibrational contributions to the polarization are small and negligible under the current experimental conditions, with the exception of deviations in adsorbate population arising from changes in pKa values for H_2O and D_2O. Collectively, these studies illustrate some of the considerations necessary for understanding the spin exchange interactions between ‘simple’ chiral molecules and ferromagnetic surfaces which elicit a chiral induced spin selectivity response.

3.4 Methods

3.4.1 Adsorption Kinetic Study with EQCM System:

The EQCM experiments were performed using a 7.9995 MHz quartz crystal with an EQCM cell attachment and a 430A potentiostat (CH Instruments). The surface area of the crystal is 0.205 cm^2 and is coated with 100 nm of nickel and 10 nm polycrystalline gold as the working electrode (CH Instruments). The counter electrode was Pt wire and the reference electrode was a saturated Ag/AgCl electrode.

The quartz crystal was first incubated in the cysteine solution for 1h to allow the system to equilibrate before applying a potential. Cyclic voltammograms (CVs) and frequency response of the quartz were recorded for 30 cycles crystal, to ensure that surface was stable and the desorption and adsorption process was reversible. Chronoamperometry experiments were performed immediately after the CV acquisition with an initial potential of -0.8 V corresponding to reductive desorption of cysteine and then a more positive potential, -0.5 V, corresponding to oxidative adsorption. A 5 s pulse width was applied during the experiment and >150 cycles was performed to build up the statistics for the histogram plots.

3.4.2 Adsorption Isotherm Study with EQCM System:

Cyclic voltammetry and QCM measurements were used to build the data for the adsorption isotherms. The data were collected by scanning from -0.4 V to - 1.1 V versus saturated Ag|AgCl at a scan rate = 25 mV/s. Unless specified all measurements were made in a pH 8 phosphate buffer solution. The frequency change from the 30th cycle, corresponding to the oxidative adsorption of cysteine on a gold substrate, was converted to a change in mass (Δm) according to the Sauerbrey equation by a factor of - 1.4 ng / Hz. The excessive amount of cycles was necessary to allow the instrument to reach equilibrium and give consistent results. Next, the mass change (Δm) was plotted versus concentration and fit to a Langmuir – Freundlich isotherm model.

3.4.3 Optical Measurement:

The optical data were collected in a 1 cm quartz cuvette. Absorbance spectroscopy was performed using an Agilent model 8453 spectrometer. Circular dichroism (CD) spectra were measured by using a JASCO J-810 CD spectrometer with a scan rate of 50 nm/min and a bandwidth of 1 nm. Each sample was scanned 3 times and the average of the three curves reported. Phosphate buffer with different pHs were used as blank solutions for baseline subtraction for different pH conditions.

3.4.4 Calculation Methods:

DFT calculations were performed using QUANTUM ESPRESSO (version 6.7.0).[35] The generalized gradient approximation (GGA) of Perdew, Burke, and Ernzerhof (PBE)[36] was used to treat electron exchange and correlation, with the D3 dispersion correction applied.[37] The pseudopotentials for the elements Au, C, H, O, N, and S were chosen from the SSSP efficiency PBE pseudopotential database (version 1.1.2).[38] For the system of interest, the plane-wave energy cutoff was tested and set to 65Ry such that the pseudopotential error is less than 10 meV / atom. For cysteine adsorption and deprotonation, a slab model of the *p* (3 × 3) Au(111) surface with four Au layers and ~18 Å of vacuum space were generated; for N-acetyl-L-cysteine methyl ester adsorption and deprotonation, a slab model of the *p* (4 × 4) Au(111) surface with three Au layers and ~18 Å of vacuum space were generated. For all calculations, the bottom one layer of Au atoms was fixed and the rest of the atoms were allowed to relax. A dipole correction[39] was added in the direction perpendicular to the Au surface. The Brillouin zone was sampled using a 4 × 4 × 1 shifted *k*-point grid. Explicit water molecules were added to each system near the hydrophilic functional groups, i.e., -SH, $-NH_x$, and -COO(H). Besides the charge caused by deprotonation, a total of 3 electrons per cell were removed from the system for all cysteine-related calculations to mimic the electrode potential such that the cysteine molecule can reasonably adsorb on the Au surface. The dipole moment of the system (adsorbates + water molecules) is calculated using the nuclear charge and the Löwdin charge of all atoms except Au. In cases where the system is not neutral, the center of the net charge is chosen as the origin to calculate the dipole moment.

3.5 Reference

1.Naaman, R.; Waldeck, D. H., Chiral-induced spin selectivity effect. *The journal of physical chemistry letters* **2012,** *3* (16), 2178-2187.

2.Naaman, R.; Paltiel, Y.; Waldeck, D. H., Chiral induced spin selectivity and its implications for biological functions. *Annual review of biophysics* **2022,** *51*, 99-114.

3.Waldeck, D.; Naaman, R.; Paltiel, Y., The spin selectivity effect in chiral materials. *APL materials* **2021,** *9* (4), 040902.

4.Kumar, A.; Capua, E.; Kesharwani, M. K.; Martin, J. M.; Sitbon, E.; Waldeck, D. H.; Naaman, R., Chirality-induced spin polarization places symmetry constraints on biomolecular interactions. *Proceedings of the National Academy of Sciences* **2017,** *114* (10), 2474-2478.

5.Banerjee-Ghosh, K.; Ben Dor, O.; Tassinari, F.; Capua, E.; Yochelis, S.; Capua, A.; Yang, S.-H.; Parkin, S. S.; Sarkar, S.; Kronik, L., Separation of enantiomers by their enantiospecific interaction with achiral magnetic substrates. *Science* **2018,** *360* (6395), 1331-1334.

6.Safari, M. R.; Matthes, F.; Ernst, K.-H.; Bürgler, D. E.; Schneider, C. M., Enantiospecific adsorption on a ferromagnetic surface at the single-molecule scale. *arXiv preprint arXiv:2211.12976* **2022**.

7.Metzger, T. S.; Mishra, S.; Bloom, B. P.; Goren, N.; Neubauer, A.; Shmul, G.; Wei, J.; Yochelis, S.; Tassinari, F.; Fontanesi, C., The electron spin as a chiral reagent. *Angewandte Chemie* **2020,** *132* (4), 1670-1675.

8.Bloom, B.; Lu, Y.; Metzger, T.; Yochelis, S.; Paltiel, Y.; Fontanesi, C.; Mishra, S.; Tassinari, F.; Naaman, R.; Waldeck, D., Asymmetric reactions induced by electron spin polarization. *Physical Chemistry Chemical Physics* **2020,** *22* (38), 21570-21582.

9.Metzger, T. S.; Siam, R.; Kolodny, Y.; Goren, N.; Sukenik, N.; Yochelis, S.; Abu-Reziq, R.; Avnir, D.; Paltiel, Y., Dynamic spin-controlled enantioselective catalytic chiral reactions. *The Journal of Physical Chemistry Letters* **2021,** *12* (23), 5469-5472.

10.Bhowmick, D.; Sang, Y.; Santra, K.; Halbauer, M.; Capua, E.; Paltiel, Y.; Naaman, R.; Tassinari, F., Simultaneous High-Purity Enantiomeric Resolution of Conglomerates Using Magnetic Substrates. *Crystal growth & design* **2021,** *21* (5), 2925-2931.

11.Tassinari, F.; Steidel, J.; Paltiel, S.; Fontanesi, C.; Lahav, M.; Paltiel, Y.; Naaman, R., Enantioseparation by crystallization using magnetic substrates. *Chemical science* **2019,** *10* (20), 5246-5250.

12.Tassinari, F.; Amsallem, D.; Bloom, B. P.; Lu, Y.; Bedi, A.; Waldeck, D. H.; Gidron, O.; Naaman, R., Spin-dependent enantioselective electropolymerization. *The Journal of Physical Chemistry C* **2020,** *124* (38), 20974-20980.

13.Bhowmick, D. K.; Das, T. K.; Santra, K.; Mondal, A. K.; Tassinari, F.; Schwarz, R.; Diesendruck, C. E.; Naaman, R., Spin-induced asymmetry reaction—The formation of asymmetric carbon by electropolymerization. *Science Advances* **2022,** *8* (31), eabq2727.

14.Lu, Y.; Bloom, B.; Qian, S.; Waldeck, D., Enantiospecificity of Cysteine Adsorption on a Ferromagnetic Surface: Is It Kinetically or Thermodynamically Controlled? *The Journal of Physical Chemistry Letters* **2021,** *12* (32), 7854-7858.

15.Maryasov, A.; Dzuba, S.; Salikhov, K., Spin-polarization effects on the phase relaxation induced by dipole-dipole interactions. *Journal of Magnetic Resonance (1969)* **1982,** *50* (3), 432-450.

16.Clever, C.; Wierzbinski, E.; Bloom, B. P.; Lu, Y.; Grimm, H. M.; Rao, S. R.; Horne, W. S.; Waldeck, D. H., Benchmarking Chiral Induced Spin Selectivity Measurements ‐ Towards Meaningful Comparisons of Chiral Biomolecule Spin Polarizations. *Israel Journal of Chemistry* **2022**, e202200045.

17.Radetic, M.; Gellman, A. J., Enantiomer Adsorption in an Applied Magnetic Field: D ‐ and L ‐ Aspartic Acid on Ni (100). *Israel Journal of Chemistry* **2022**, e202200028.

18.Wu, Y.; Subotnik, J. E., Electronic spin separation induced by nuclear motion near conical intersections. *Nature communications* **2021,** *12* (1), 700.

19.Krężel, A.; Bal, W., A formula for correlating pKa values determined in D2O and H2O. *Journal of inorganic biochemistry* **2004,** *98* (1), 161-166.

20.Naaman, R.; Paltiel, Y.; Waldeck, D. H., Chiral molecules and the electron spin. *Nature Reviews Chemistry* **2019,** *3* (4), 250-260.

21.Burner, U.; Obinger, C., Transient-state and steady-state kinetics of the oxidation of aliphatic and aromatic thiols by horseradish peroxidase. *FEBS letters* **1997,** *411* (2-3), 269-274.

22.Noszal, B.; Guo, W.; Rabenstein, D. L., Rota-microspeciation of serine, cysteine, and selenocysteine. *The Journal of Physical Chemistry* **1991,** *95* (23), 9609-9614.

23.Creighton, D. J.; Schamp, D. J., Solvent isotope effects on tautomerization equilibria of papain and model thiolamines. *FEBS letters* **1980,** *110* (2), 313-318.

24.Zimmermann, T.; Chval, Z.; Burda, J. V., Cisplatin interaction with cysteine and methionine in aqueous solution: computational DFT/PCM study. *The Journal of Physical Chemistry B* **2009,** *113* (10), 3139-3150.

25.Evers, F.; Aharony, A.; Bar‐Gill, N.; Entin‐Wohlman, O.; Hedegård, P.; Hod, O.; Jelinek, P.; Kamieniarz, G.; Lemeshko, M.; Michaeli, K., Theory of chirality induced spin selectivity: Progress and challenges. *Advanced Materials* **2022,** *34* (13), 2106629.

26.Grunwald, E.; Chang, K.; Skipper, P.; Anderson, V., Kinetics of bifunctional proton transfer. 2. Lysine and cysteine in aqueous solutions. *The Journal of Physical Chemistry* **1976,** *80* (13), 1425-1431.

27.Choi, J. K.; Haynie, B. E.; Tohgha, U.; Pap, L.; Elliott, K. W.; Leonard, B. M.; Dzyuba, S. V.; Varga, K.; Kubelka, J.; Balaz, M., Chirality inversion of CdSe and CdS quantum dots without changing the stereochemistry of the capping ligand. *ACS nano* **2016,** *10* (3), 3809-3815.

28.Kuznetsova, V. A.; Mates-Torres, E.; Prochukhan, N.; Marcastel, M.; Purcell-Milton, F.; O’Brien, J.; Visheratina, A. K.; Martinez-Carmona, M.; Gromova, Y.; Garcia-Melchor, M., Effect of chiral ligand concentration and binding mode on chiroptical activity of CdSe/CdS quantum dots. *ACS nano* **2019,** *13* (11), 13560-13572.

29.Bloom, B. P.; Graff, B. M.; Ghosh, S.; Beratan, D. N.; Waldeck, D. H., Chirality control of electron transfer in quantum dot assemblies. *Journal of the American Chemical Society* **2017,** *139* (26), 9038-9043.

30.Eyring, H.; Walter, J.; Kimball, G., Quantum Chemistry John Wiley h Sons. *Inc., New York I* **1944,** *960*, 371.

31.Wang, X.; Yan, Y., Optical activity of solids from first principles. *Physical Review B* **2023,** *107* (4), 045201.

32.De Marco, L.; Carpenter, W.; Liu, H.; Biswas, R.; Bowman, J. M.; Tokmakoff, A., Differences in the vibrational dynamics of H2O and D2O: observation of symmetric and antisymmetric stretching vibrations in heavy water. *The Journal of Physical Chemistry Letters* **2016,** *7* (10), 1769-1774.

33.Perakis, F.; Widmer, S.; Hamm, P., Two-dimensional infrared spectroscopy of isotope-diluted ice Ih. *The Journal of chemical physics* **2011,** *134* (20), 204505.

34.Beedle, A. E.; Mora, M.; Davis, C. T.; Snijders, A. P.; Stirnemann, G.; Garcia-Manyes, S., Forcing the reversibility of a mechanochemical reaction. *Nature Communications* **2018,** *9* (1), 3155.

35.Giannozzi, P.; Andreussi, O.; Brumme, T.; Bunau, O.; Nardelli, M. B.; Calandra, M.; Car, R.; Cavazzoni, C.; Ceresoli, D.; Cococcioni, M., Advanced capabilities for materials modelling with Quantum ESPRESSO. *Journal of physics: Condensed matter* **2017,** *29* (46), 465901.

36.Perdew, J. P.; Burke, K.; Ernzerhof, M., Generalized gradient approximation made simple. *Physical review letters* **1996,** *77* (18), 3865.

37.Ehrlich, S.; Moellmann, J.; Reckien, W.; Bredow, T.; Grimme, S., System - dependent dispersion coefficients for the DFT - D3 treatment of adsorption processes on ionic surfaces. *ChemPhysChem* **2011,** *12* (17), 3414-3420.

38.Prandini, G.; Marrazzo, A.; Castelli, I. E.; Mounet, N.; Marzari, N., Precision and efficiency in solid-state pseudopotential calculations. *npj Computational Materials* **2018,** *4* (1), 72.

39.Bengtsson, L., Dipole correction for surface supercell calculations. *Physical Review B* **1999,** *59* (19), 12301.

4.0 Beyond Stereoisomeric Effects: Exploring the Importance of Intermolecular Electron Spin Interactions in Biorecognition

This work was published as Lu, Y., Joy, M., Bloom, B. P., Waldeck, D. H. *The Journal of Physical Chemistry Letters*, **2023**, 14, 7032-7037. The author of the dissertation performed the design of the experiments, the electrochemical quartz crystal microbalance measurement, the optical measurement, data analysis and participated in writing the manuscript. The supporting information for this chapter can be found in Appendix C.

This work shows that electron spin polarization and stereoisomeric effects make comparable contributions to the enantioselective binding of amino acids. Magneto-electrochemical quartz crystal microbalance methods are used to study the adsorption of chiral amino acids onto a monolayer film of chiral molecules which are spin-polarized by an underlying ferromagnetic substrate. The direction of the electron spin polarization, affects both the kinetics and thermodynamics for the enantiospecific adsorption of the amino acids. Comparison of these data with the circular dichroism (CD) spectra of the amino acid adsorbates shows that the CD spectrum of the interacting group provides a good figure-of-merit for predicting the contributions of electron spin to the intermolecular interaction. These findings demonstrate the importance of electron spin in enantioselective intermolecular interactions between chiral amino acids and represent a paradigm shift for how one should view selectivity in biorecognition.

4.1 Introduction

Chiral molecules comprise the fundamental building blocks of life and appear essentially in an enantiopure form (homochiral); e.g., sugars are primarily dextrorotatory and amino acids are levorotatory.[1-2] Although the emergence of homochirality in nature remains an enigma, it is well known that enantiomeric purity has important consequences for biochemical processes;[3-4] e.g., despite possessing the same molecular structure, the ‘wrong’ enantiomer can have detrimental effects.[5] Such behavior is particularly important in pharmacological applications and ongoing research efforts aim to improve enantioselective synthesis[6-8] and chiral resolution strategies.[9-11] Conventional wisdom maintains that enantioselectivity in molecular recognition by biomolecules arises from differences in the three-dimensional binding geometries and their charge distributions;[12-14] however these considerations do not consider the role that the molecules’ electron spin polarization may play in these processes.

Research over the past 20 years shows that chiral molecules can spin polarize electrons upon transport and charge redistribution, owing to the chiral induced spin selectivity (CISS) effect,[15-17] and that CISS-mediated processes occur in biological systems.[17-20] The CISS effect refers to the phenomenon in which electrons with a defined spin orientation preferentially transmit through chiral molecules and materials, whereas transport of electrons with the opposite spin orientation are inhibited. Note, the preferred spin transport depends sensitively on the enantiomeric form of the molecule, or enantiomorph of the material, through which it traverses.[21] Because the charge polarization of a chiral molecule is accompanied by a net spin polarization,[22] we posit that electron spin polarizations ought to manifest in biomolecular intermolecular interactions.

This work uses magneto-electrochemical quartz crystal microbalance (mEQCM) methods to study the adsorption kinetics of amino acids onto magnetized ferromagnetic surfaces, which are coated with N-acetyl cysteine (NAC) self-assembled monolayer (SAM) films of chiral molecules. NAC is a known drug applied in a wide range of pathologies and immobilized NAC can achieve a better performance in the bioreactions.[23] Here, the amino acids represent common biological adsorbates and the SAM/ferromagnetic electrode is an analogue for a biomacromolecule possessing spin polarization. We show that the intermolecular binding is enantio- and spin-specific and that chiroptical features of the adsorbate are a good predictor for determining the sign of the spin selectivity. These findings elucidate new features of the mechanism underlying the enantiopure crystallization from racemic mixtures[24] and enhance our understanding for the enantiospecific adsorption of chiral molecules onto magnetized ferromagnetic surfaces.[25] More generally, these studies demonstrate the importance of spin considerations in chiral intermolecular interactions.

4.2 Results and discussion

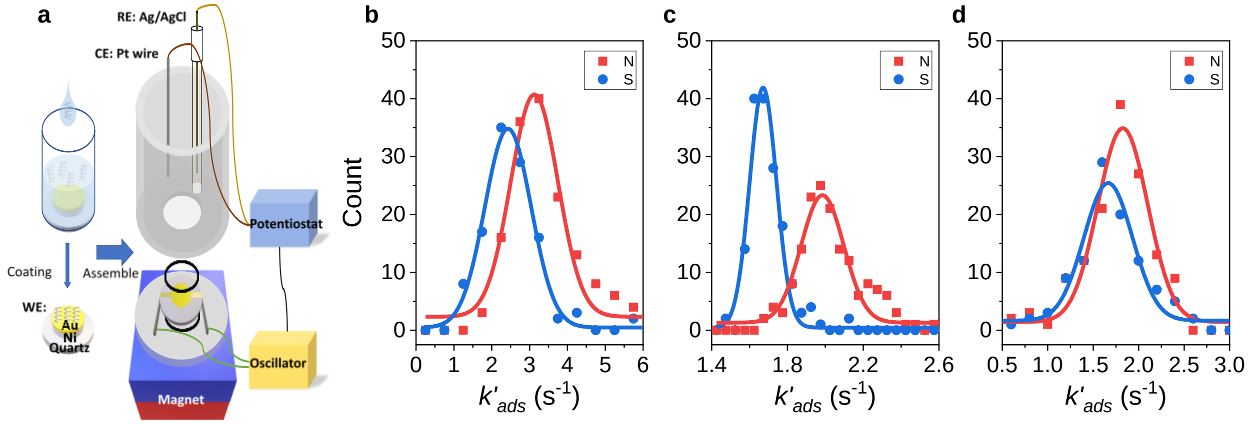

Figure 4.1 Determination of adsorption rate constants. (a) Schematic illustration of the mEQCM set up. (b), (c), & (d) Histograms for the adsorption rate constant of L-leucine methyl ester (L-LeuME) onto Ni/Au film

electrodes coated with L-n-acetyl cysteine (L-NAC), mercaptopropionic acid (MPA), and D-NAC monolayer films, respectively, under North magnetic field (red) and South magnetic field (blue). Note, the solid line is a Gaussian fit to the data.

To probe the spin-dependence in the binding of amino acids, we prepared self-assembled films of an amino acid analogue on a ferromagnetic surface and studied the binding of amino acids to that film as a function of its magnetization state, following similar methods to that established in our previous work.[25] Briefly, an external magnetic field was applied to the underside of the electrode with its North or South pole oriented normal to the electrode surface and chronoamperometric techniques were used to monitor the change in mass, and hence the kinetics for the adsorption; see Figure 4.1a for a schematic illustration of the set up and section 4.4 for additional experimental details. Here, the adsorption kinetics of leucine methyl ester, LeuME, onto n-acetyl cysteine, NAC, self-assembled monolayer (SAM) coated Ni/Au electrodes (100 nm Ni/ 10 nmAu/ NAC) electrodes was studied. An applied bias potential of -0.4V was used to facilitate adsorption of LeuME onto the electrode and then the potential was jumped to 0V to initiate desorption. Note, Figure C.1 shows control experiments which demonstrate that under these potential conditions the NAC remains on the electrode surface and only adsorption / desorption of LeuME occurs.

Figure 4.1 shows histograms of the measured adsorption rate constants of L-LeuME onto L-NAC (Figure 4.1b), mercaptopropionic acid, MPA, as an achiral control (Figure 4.1c), and D-NAC (Figure 4.1d) coated electrodes for the cases of a North magnetized electrode (red) and a South magnetized electrode (blue). For all three SAM compositions the adsorption rate constant for L-Leu ME is faster when the magnetization is oriented North rather than South. Conversely, the opposite is true, South is faster than North, when D-LeuME is used as the adsorbate; see Figure C.5. The dissymmetry in the magnetization dependence of the adsorption rate constant with the amino acid's enantiomeric form is consistent with a CISS-mediated effect.[26] To quantify the magnitude of the dissymmetry in adsorption rate constant with magnetization, a polarization parameter P was defined as Eq. (1)

$$P = \frac{k'_{ads,N} - k'_{ads,S}}{k'_{ads,N} + k'_{ads,S}} \cdot 100\% \qquad \text{Eq (1)}$$

where $k'_{ads,N}$ and $k'_{ads,S}$ correspond to the average adsorption rate constant, determined by the maximum of a gaussian fit to the histogram data, under North and South magnetizations of the electrode, respectively.

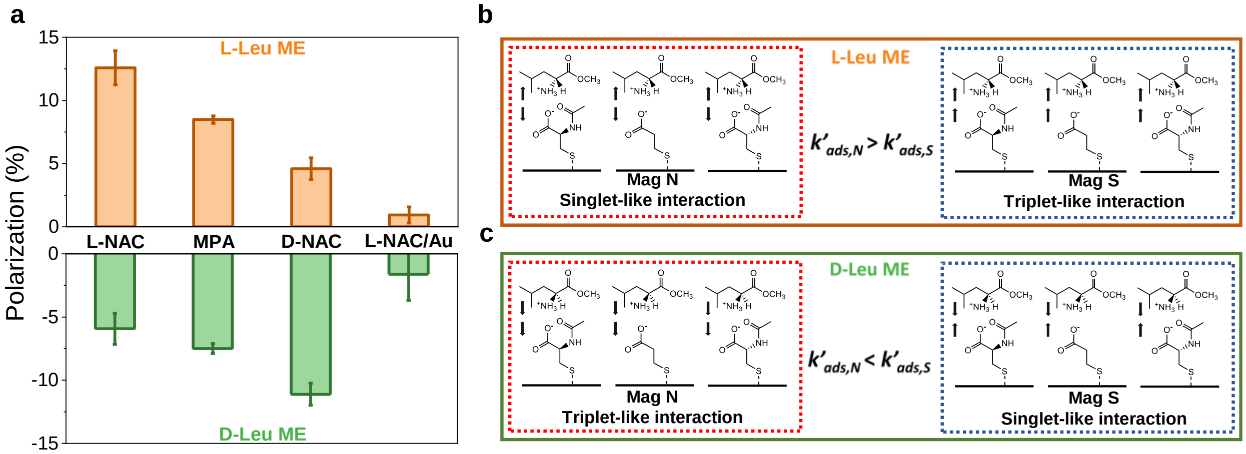

Figure 4.2 Spin mediated asymmetry in adsorption kinetics. (a) Polarization in adsorption rate constant for L-LeuME (orange) and D-LeuME (green) enantiomers on three different monolayer films: L-NAC, MPA, and D-NAC on NiAu substrates, and for L-NAC coated on an Au substrate as a control experiment. The error bars represent the uncertainty and were obtained by propagating the error from Eq (1), using the standard deviation of the mean of the rate constant as an error measure. (b) Mechanistic scheme illustrating the emergence of an intermolecular 'singlet' adsorption interaction between L-LeuME with different SAMs under a North magnetic field and a 'triplet' adsorption interaction under South magnetic field. (c) Mechanistic scheme illustrating the emergence of an intermolecular 'triplet' adsorption interaction between L-LeuME with different SAMs under a North magnetic field and a 'singlet' adsorption interaction under South magnetic field. See text for a more detailed discussion of the mechanism.

Figure 4.2 shows *P* values for L-LeuME (orange) and D-LeuME (green) on L-NAC, D-NAC, and MPA SAM-coated Ni/Au electrodes, and L-NAC coated Au electrodes as a control experiment. For these data, the sign of *P* is determined by the chirality of the adsorbate, however the magnitude of *P* changes with the enantiomeric form of the SAM relative to the adsorbate. Note that *P* for the achiral SAM has a nearly equal magnitude for the two different LeuMe adsorbates, albeit with opposite signs. These data reveal the effect of spin polarization, which is driven by the magnetized film electrode, on the binding to MPA, which should not have a stereoisomeric preference for one amino acid enantiomer over the other. In contrast, the L-NAC films show a larger magnitude of *P* for the binding of L-LeuME than it does for D-LeuME; and correspondingly the homochiral binding of D-NAC with D-LeuME has a larger magnitude of *P* than its heterochiral analogue of D-NAC with L-LeuME but with different signs. While the difference in the sign of *P* is controlled by the spin polarization preference of the analyte amino acid, the magnitude of the *P* is affected by the spin polarization created in the SAM by the magnetized electrode,[19] the spin-induced charge redistribution in the chiral SAMs,[27] and the stereoisomeric interactions between the amino acid and the chiral SAM.[28]

The scheme in Figure 4.2 shows a proposed mechanism for the spin- and enantio-specific adsorption of L-LeuME onto the three SAM electrodes. As L-LeuME approaches the negatively charged L-NAC SAM-coated magnetized surface, charge redistribution of the L-LeuME molecule's electron cloud occurs. Because of the CISS effect, the induced charge polarization gives rise to an accompanying spin polarization across the molecule, with spin up electrons accumulating at the $-NH_3^+$ terminus. As the L-LeuME nears the SAM, electron exchange interactions increase between the spin polarized $-COO^-$ in L-NAC, determined by the magnetization of the substrate, and the spin polarized $-NH_3^+$ in L-LeuME, determined by the handedness of the molecule. The attractive interaction is stronger when the excess spin density at the surface of the SAM is opposite to that of the excess spin density presented by the molecule in solution. Thus, the L-LeuME, in which the -NH_3^+ terminus adopts an ‘up’ spin, interacts with the North magnetized surface, net spin down, with a singlet-like interaction (pairing) and displays faster adsorption kinetics; see Figure 4.2b, left. Conversely, when the surface of the electrode is South magnetized, the spins at the surface possess the same orientation as that on the L-Leu ME -NH_3^+ terminus, ‘up’ spins, giving rise to a triplet-like interaction and slower adsorption kinetics; see Figure 4.2b, right. Note that the use of ‘singlet-like’ and ‘triplet-like’ refer to the spin-spin interaction alignment and not specifically to singlet and triplet states. Because the excess spin density at the surface of the electrode is always defined by the applied magnetic field direction, the L-Leu ME always adsorbs faster with North magnetization than South magnetization; and the opposite is true for D-Leu ME; see Figure 4.2c. Control experiments on an L-NAC coated Au diamagnetic electrode, show only weak differences in the adsorption rate with magnetization, *i.e.* $k'_{ads,N}$ and $k'_{ads,S}$ of L-LeuME (or D-LeuME) are nearly equal. All together these data reveal the pronounced effect that spin can have on the adsorption kinetics.

The magnitude of the excess spin polarization, and hence the magnitude of P, depends on the amount of spin density emanating from the ferromagnetic electrode through the SAM. Previous work on chiral SAM-coated ferromagnetic electrodes shows that changing the electrode’s magnetization, North versus South, generates a change in the surface charge that also depends on the handedness of the SAM; *i.e.* spin polarization elicits a change in charge polarization.[27] For our system, L-NAC (D-NAC) SAMs facilitate spin ‘down’ (‘up’) electrons more favorably than spin ‘up’ (‘down’) electrons which implies that the surface charge and double layer potential drop is likely larger under a North (South) magnetic field. This magnetization-dependent change in surface charge should accompany the standard stereoisomeric differences that manifest for homochiral/heterochiral effects on the intermolecular interaction energies.

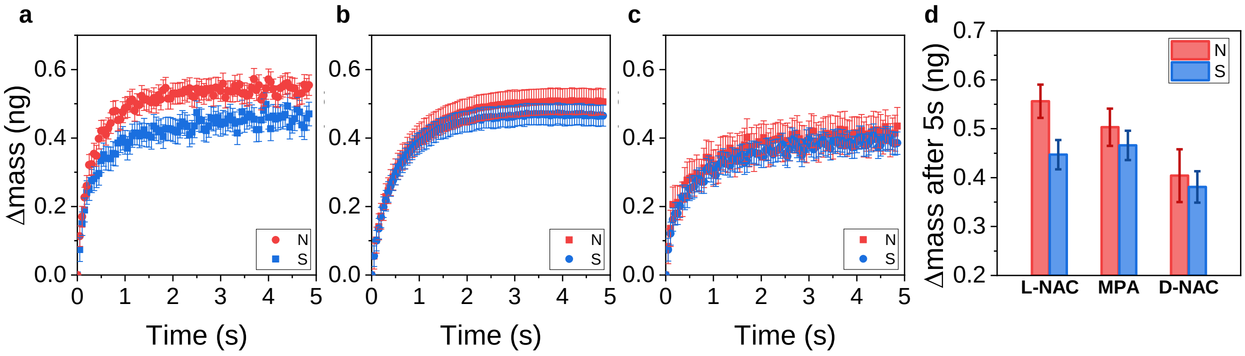

Figure 4.3 Magnetic field effects on amount of adsorption. (a), (b), & (c) Average mass change during the adsorption of L-LeuME onto Ni/Au substrate coated with L-NAC, MPA, and D-NAC, respectively, under North magnetic field (red) and South magnetic field (blue). The error bars represent the standard deviation of the mean of the mass across multiple measurements. (d) The average mass change at 5s on different monolayer films: L-NAC, MPA, and D-NAC on Ni/Au substrate. The error bars represent the standard deviation of the mean of the mass.

To test this hypothesis, we compared the change in mass of L-LeuME at 5s, after the adsorption process has largely concluded. Figure 4.3 reports these data for L-NAC, MPA, and D-NAC coated electrodes as a function of magnetization. For the different SAM compositions, a difference in adsorbate mass was observed under North and South applied magnetic fields; and the average mass, $(m_{north} + m_{south})/2$, adsorbed on the three SAMs is different, see Table C.1. Homochiral ensembles exhibited the largest average change in mass and the largest mass asymmetry with magnetic field, whereas the heterochiral assemblies exhibited the smallest average mass and the smallest mass asymmetry with magnetic field. The achiral SAMs were intermediate between the homochiral and heterochiral cases. Previously, the enantiospecific adsorption of chiral molecules onto a bare ferromagnetic substrate was determined to be a kinetically controlled process.[25, 29] For the biomimetic system used here, the experiments reveal both kinetic and thermodynamic contributions to the enantiospecific binding, suggesting a synergy between the spin polarization emanating from the ferromagnetic electrode and the CISS response of the chiral NAC film.

Figure 4.4a illustrates the stereoisomeric effect on the intermolecular interaction, where more molecules can adsorb for homochiral ensembles compared to heterochiral ensembles. Figure 4b illustrate the combination of stereoisomeric and spin effect. The largest mass change, strongest intermolecular adsorption, occurs for homochiral ensembles under a certain magnetic field direction; i.e. L-LeuME with L-NAC SAMs under North magnetic field . Magnetization of the substrate affects the surface charge and this effect operates in concert with the stereoisomeric effects on the binding. These effects act over long times and can give rise to the total mass change that is observed. The chiral films also display a spin polarization, giving rise to singlet-like vs. triplet-like interactions between the L-LeuME and the L-NAC layer; and these may operate primarily on the rate of adsorption. Thus, the combined system of chiral SAMs and ferromagnetic substrates can display both kinetic and thermodynamic differences; i.e. North magnetization (Figure 4.4b(i)) of the Ni/Au/L-NAC interfaces gives rise to higher adsorption rate constants and to higher amounts of adsorbed L-LeuME than does South magnetization (Figure 4.4b(ii)). For heterochiral assemblies the intermolecular interaction energies should be weaker. For Ni/Au/D-NAC interfaces the North magnetized electrode produces a lower excess spin density in the ‘down’ direction than it does for the L-NAC case, and this leads to a smaller shift in the interfacial charge. These effects combine with stereoisomeric differences to reduce the overall spin-dependent adsorption, as compared to the homochiral case.

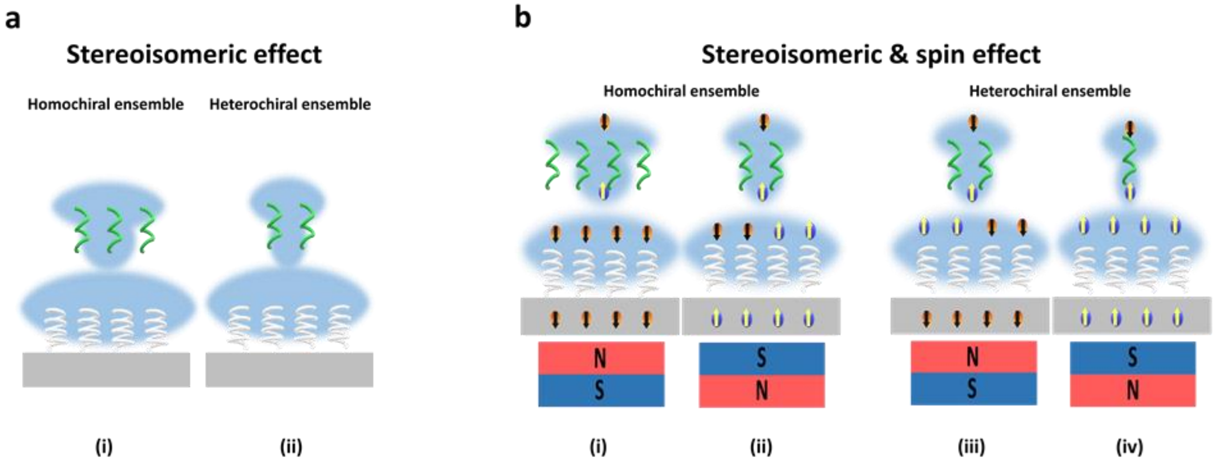

Figure 4.4 Stereoisomeric and spin effect contributions to adsorption. (a) schematic representation of stereoisomeric effect for the intermolecular interaction for homochiral ensemble and heterochiral ensemble. (b) schematic representation of stereoisomeric and spin effect for the intermolecular interaction between for homochiral ensemble and heterochiral ensemble under North and South magnetic fields. The size of the electron cloud, blue, represents the magnitude of the charge density. Spin down electrons are depicted as orange and spin up electrons depicted as blue.

To assess the universality of the findings for the LeuME to NAC SAM system, additional experiments were performed using L-NAC as the SAM with other levorotatory amino acids. The polarizations from these studies are reported in Table 4.1. Experiments showed that L-phenylalanine, L-tryptophan, L-histidine, L-proline, and L-tyrosine amino acids exhibit negative polarizations in adsorption rate constants, whereas L-leucine, L-isoleucine, L-serine, L-alanine, and L-leucine methyl ester amino acids display positive polarizations. Table 1 also reports findings for the achiral amino acid glycine for which no net polarization is observed.

Table 4.1 The polarization in adsorption rate constant of L-amino acids onto L-NAC SAMs and the peak sign of CD spectra of L-amino acids in the 190 nm - 200 nm band. The error in polarization is the uncertainty calculated from Eq (1) with the standard deviation of the mean of the rate.

	Polarization	Sign of CD at 190 nm ~ 200 nm
L-Phenylalanine (L-Phe)	-12.64±0.94%	–

L-Tryptophan (L-Trp)	-7.56±0.17%	−
L-Histidine (L-His)	-12.6±1.75%	−
L-Leucine (L-Leu)	2.97±0.28%	+
L-Isoleucine (L-Ile)	2.68±1.10%	+
L-Serine (L-Ser)	3.80±0.62%	+
L-Alanine (L-Ala)	1.90±0.39%	+
L-Proline (L-Pro)	-5.93±0.51%	−
L-Tyrosine (L-Tyr)	-6.90±0.36%	−
L-Leucine Methyl Ester (L-LeuME)	12.59±1.35%	+
Glycine (Gly)	0.88 ± 0.58%	N/A

Because earlier work on spin-dependent electron transfer rates and spin-filtering of electron currents by chiral molecules has shown a correlation of the measured spin polarization with the system's chiroptical response,[30] the polarization data for the adsorbate binding were compared with the circular dichroism (CD) spectra for each amino acid (see Figure C.13). Table 1 reports the sign of the CD signal between 190-200 nm, with a majority contribution corresponding to a high intensity π-π* transition associated with the π orbitals of the carbonyl bond as well as contributions from the amine.[31-32] Interestingly, for amino acids displaying a negative *P* in the adsorbate kinetics the CD signals between 190-200 nm are negative; whereas for amino acids showing a positive *P* in the adsorbate kinetics the CD signals between 190-200 nm are positive. It is important to appreciate that different features in the CD spectra can emerge for the different amino acids (associated with constraints of the molecular backbone,[33] aggregation through hydrophobic aromatic side chains,[31] and peak shifts arising from electronic effects[31, 34]), however the correlation of the sign of the *P* with the sign of the CD signal associated with the interacting moieties persists.

4.3 conclusion

This work shows that the intermolecular interactions between a biomolecular analogue and chiral molecules is enantiospecific and strongly sensitive to electron spin effects. The spin-dependent exchange interactions manifest as changes in both the kinetically driven adsorption process, *i.e.*, singlet-like vs. triplet-like interactions control the adsorption rate constant, as well the thermodynamically controlled surface energies, leading to differences in the amount of adsorbate on the different spin polarized surfaces. The spin-dependent phenomena are shown to occur in conjunction with traditional changes in intermolecular interaction energies associated with homo and heterochiral architectures. The findings show that the spin polarization effects are comparable, even stronger, than the stereoisomeric effects. Lastly, we demonstrate that the sign of the CD signals of the adsorbate's interacting functional group can be used as a good metric for predicting the sign of the enantioselective binding, *i.e.* the identity of the preferred enantiomer. Collectively, these findings imply that spin constraints during biorecognition may impart selectivity in the adsorbate type and binding geometry of the adsorbate in nature and necessitates a paradigm shift in how one should view selectivity in biorecognition.

4.4 method

4.4.1 Magnetic electrochemical quartz crystal microbalance (mEQCM).

The mEQCM experiments were performed using a 7.9995 MHz quartz crystal in an EQCM cell attachment and a 430A potentiostat (CH Instruments). The surface area of the crystal is 0.205

cm^2 and is coated with 100 nm of nickel and 10 nm polycrystalline gold as the working electrode area (CH Instruments). The counter electrode was a Pt wire and the reference electrode was a saturated Ag/AgCl electrode. Magnetic field studies placed a permanent magnet, 0.54 T (K&J Magnetics) underneath the working electrode during the experiment.

4.4.2 Self-assembled Monolayer Formation and Stability measurement.

The quartz crystal working electrodes were incubated in a 50 mM solution of L-NAC (or D-NAC) in 0.1 M phosphate buffer at pH 9 overnight. Then the electrode was rinsed three times with phosphate buffer and water to remove any loosely, physisorbed material. The electrodes were then blown dry with a stream of Argon. Linear sweep voltammetry (LSV) and QCM measurements were used to study the stability of the L- and D-NAC SAMs. Here, the SAM coated quartz crystal working electrode was incubated in a 0.1 M phosphate buffer (pH 9) electrolyte solution for 30 min, to allow the QCM frequency to stabilize. Next the electrode was scanned from 0 V to – 0.9 V versus saturated Ag|AgCl at a scan rate = 25 mV/s and the change in mass was monitored.

4.4.3 Adsorption study with mEQCM.

The SAM coated quartz crystal was first incubated in a 0.1 M phosphate buffer (pH 9) electrolyte solution containing a 150 µM of an amino acid and allowed to equilibrate for 30 minutes. Next, linear sweep voltammetry and QCM measurements were performed to determine the desorption and re-adsorption of the amino acid onto the NAC SAM coated film; the data were collected by scanning from -0 V to – 0.8 V versus saturated Ag|AgCl at a scan rate = 25 mV/s. Upon determination of the potentials required for adsorption and desorption, the SAM coated quartz crystal was incubated for an additional 30 min to allow the system to equilibrate and then chronoamperometry experiments were performed. Take for example L-Leu ME; An initial potential of -0.4 V corresponding to reductive adsorption of L-Leu ME was applied and then a more positive potential, 0 V, corresponding to oxidative desorption. The applied voltage was jumped between these two values and the QCM response was collected as a function of time after the potential jump. A 5 s pulse width was applied during the experiment and >150 cycles were performed to calculate the average mass change for thermodynamic analysis and to build up the statistics for histogram plots to perform a kinetic analysis of the adsorption and desorption process.

4.4.4 Optical Measurements.

Absorbance spectroscopy was performed using an Agilent model 8453 spectrometer and Circular dichroism (CD) spectra were measured using a JASCO J-810 CD spectrometer with a scan rate of 20 nm/min and a bandwidth of 1 nm. For the CD measurements each sample was scanned three times and the average of the three curves is reported. The absorbance and circular dichroism data were collected in a 2 mm quartz cuvette containing 2 mM phosphate buffer (pH 9) and 0.5mM concentration of amino acid.

4.5 Reference

1.Bada, J. L., Origins of homochirality. *Nature* **1995,** *374* (6523), 594-595.

2.Rosenberg, R. A.; Mishra, D.; Naaman, R., Chiral Selective Chemistry Induced by Natural Selection of Spin‐Polarized Electrons. *Angewandte Chemie* **2015,** *127* (25), 7403-7406.

3.Mason, S. F., Origins of biomolecular handedness. *Nature* **1984,** *311* (5981), 19-23.

4.Blackmond, D. G., Asymmetric autocatalysis and its implications for the origin of homochirality. *Proceedings of the National Academy of Sciences* **2004,** *101* (16), 5732-5736.

5.Lorenz, H.; Seidel‐Morgenstern, A., Processes to separate enantiomers. *Angewandte Chemie International Edition* **2014,** *53* (5), 1218-1250.

6.Silverio, D. L.; Torker, S.; Pilyugina, T.; Vieira, E. M.; Snapper, M. L.; Haeffner, F.; Hoveyda, A. H., Simple organic molecules as catalysts for enantioselective synthesis of amines and alcohols. *Nature* **2013,** *494* (7436), 216-221.

7.Walsh, M. P.; Phelps, J. M.; Lennon, M. E.; Yufit, D. S.; Kitching, M. O., Enantioselective synthesis of ammonium cations. *Nature* **2021,** *597* (7874), 70-76.

8.Li, M.-L.; Pan, J.-B.; Zhou, Q.-L., Enantioselective synthesis of amino acids from ammonia. *Nature Catalysis* **2022,** *5* (6), 571-577.

9.Shukla, N.; Gellman, A. J., Chiral metal surfaces for enantioselective processes. *Nature Materials* **2020,** *19* (9), 939-945.

10.Fang, Y.; Ghijsens, E.; Ivasenko, O.; Cao, H.; Noguchi, A.; Mali, K. S.; Tahara, K.; Tobe, Y.; De Feyter, S., Dynamic control over supramolecular handedness by selecting chiral induction pathways at the solution–solid interface. *Nature chemistry* **2016,** *8* (7), 711-717.

11.Shen, J.; Okamoto, Y., Efficient separation of enantiomers using stereoregular chiral polymers. *Chemical reviews* **2016,** *116* (3), 1094-1138.

12.Peluso, P.; Chankvetadze, B., Recognition in the domain of molecular chirality: From noncovalent interactions to separation of enantiomers. *Chemical Reviews* **2022,** *122* (16), 13235-13400.

13.Zehnacker, A.; Suhm, M. A., Chirality recognition between neutral molecules in the gas phase. *Angewandte Chemie International Edition* **2008,** *47* (37), 6970-6992.

14.Hamankiewicz, P.; Granda, J. M.; Jurczak, J., Influence of the size and geometry of the anion binding pocket of sugar–urea anion receptors on chiral recognition. *Tetrahedron Letters* **2013,** *54* (41), 5608-5611.

15.Naaman, R.; Paltiel, Y.; Waldeck, D. H., Chiral induced spin selectivity and its implications for biological functions. *Annual review of biophysics* **2022,** *51*, 99-114.

16.Waldeck, D.; Naaman, R.; Paltiel, Y., The spin selectivity effect in chiral materials. *APL materials* **2021,** *9* (4), 040902.

17.Naaman, R.; Paltiel, Y.; Waldeck, D. H., Chiral induced spin selectivity gives a new twist on spin-control in chemistry. *Accounts of Chemical Research* **2020,** *53* (11), 2659-2667.

18.Liu, Y.; Xiao, J.; Koo, J.; Yan, B., Chirality-driven topological electronic structure of DNA-like materials. *Nature materials* **2021,** *20* (5), 638-644.

19.Naaman, R.; Paltiel, Y.; Waldeck, D. H., Chiral molecules and the electron spin. *Nature Reviews Chemistry* **2019,** *3* (4), 250-260.

20.Michaeli, K.; Kantor-Uriel, N.; Naaman, R.; Waldeck, D. H., The electron's spin and molecular chirality–how are they related and how do they affect life processes? *Chemical Society Reviews* **2016,** *45* (23), 6478-6487.

21.Naaman, R.; Waldeck, D. H., Chiral-induced spin selectivity effect. *The journal of physical chemistry letters* **2012,** *3* (16), 2178-2187.

22.Kumar, A.; Capua, E.; Kesharwani, M. K.; Martin, J. M.; Sitbon, E.; Waldeck, D. H.; Naaman, R., Chirality-induced spin polarization places symmetry constraints on biomolecular interactions. *Proceedings of the National Academy of Sciences* **2017,** *114* (10), 2474-2478.

23.Costa, F.; Sousa, D. M.; Parreira, P.; Lamghari, M.; Gomes, P.; Martins, M. C. L., N-acetylcysteine-functionalized coating avoids bacterial adhesion and biofilm formation. *Scientific reports* **2017,** *7* (1), 1-13.

24.Tassinari, F.; Steidel, J.; Paltiel, S.; Fontanesi, C.; Lahav, M.; Paltiel, Y.; Naaman, R., Enantioseparation by crystallization using magnetic substrates. *Chemical science* **2019,** *10* (20), 5246-5250.

25.Lu, Y.; Bloom, B.; Qian, S.; Waldeck, D., Enantiospecificity of Cysteine Adsorption on a Ferromagnetic Surface: Is It Kinetically or Thermodynamically Controlled? *The Journal of Physical Chemistry Letters* **2021,** *12* (32), 7854-7858.

26.Ben Dor, O.; Yochelis, S.; Radko, A.; Vankayala, K.; Capua, E.; Capua, A.; Yang, S.-H.; Baczewski, L. T.; Parkin, S. S. P.; Naaman, R., Magnetization switching in ferromagnets by adsorbed chiral molecules without current or external magnetic field. *Nature communications* **2017,** *8* (1), 1-7.

27.Ghosh, S.; Mishra, S.; Avigad, E.; Bloom, B. P.; Baczewski, L.; Yochelis, S.; Paltiel, Y.; Naaman, R.; Waldeck, D. H., Effect of chiral molecules on the electron’s spin wavefunction at interfaces. *The journal of physical chemistry letters* **2020,** *11* (4), 1550-1557.

28.Liu, Z.; Li, X.; Masai, H.; Huang, X.; Tsuda, S.; Terao, J.; Yang, J.; Guo, X., A single-molecule electrical approach for amino acid detection and chirality recognition. *Science Advances* **2021,** *7* (10), eabe4365.

29.Banerjee-Ghosh, K.; Ben Dor, O.; Tassinari, F.; Capua, E.; Yochelis, S.; Capua, A.; Yang, S.-H.; Parkin, S. S.; Sarkar, S.; Kronik, L., Separation of enantiomers by their enantiospecific interaction with achiral magnetic substrates. *Science* **2018,** *360* (6395), 1331-1334.

30.Bloom, B. P.; Graff, B. M.; Ghosh, S.; Beratan, D. N.; Waldeck, D. H., Chirality control of electron transfer in quantum dot assemblies. *Journal of the American Chemical Society* **2017,** *139* (26), 9038-9043.

31.Amdursky, N.; Stevens, M. M., Circular dichroism of amino acids: following the structural formation of phenylalanine. *ChemPhysChem* **2015,** *16* (13), 2768-2774.

32.Rodger, A.; Norden, B., Circular dichroism of biomolecules. *Circular Dichroism and Linear Dichroism* **1997**, 15-32.

33.Madison, V.; Schellman, J., Location of proline derivatives in conformational space. I. Conformational calculations; optical activity and NMR experiments. *Biopolymers: Original Research on Biomolecules* **1970,** *9* (5), 511-567.

34.Cassim, J. Y.; Yang, J. T., Effect of molecular aggregation on circular dichroism and optical rotatory dispersion of helical poly-L-glutamic acid in solution. *Biochemical and Biophysical Research Communications* **1967,** *26* (1), 58-64.

5.0 Asymmetric Reactions Induced By Electron Spin Polarization

This work was taken from the published work: Bloom, B.; Lu, Y.; Metzger, T.; Yochelis, S.; Paltiel, Y.; Fontanesi, C.; Mishra, S.; Tassinari, F.; Naaman, R.; Waldeck, D., Asymmetric reactions induced by electron spin polarization. *Physical Chemistry Chemical Physics* **2020,** *22* (38), 21570-21582. The author of the dissertation performed the design of and the enantioselective electropolymerization from achiral monomers experiments and participated in writing the manuscript. The supporting information for this chapter can be found in Appendix D.

Two enantioselective electrochemical reactions that have used polarized electron spins as a chiral reagent are described; enantioselective electroreduction to resolve an enantiomer from a racemic mixture and an oxidative electropolymerization to generate a chiral polymer from achiral monomers. A complementary approach that has used spin-polarized, but otherwise achiral, molecular films to enantiospecifically associate with one enantiomer from a racemic mixture is also discussed. Each of these reaction types use magnetized films to generate the spin polarized electrons and the enantiospecificity can be selected by choice of the magnetization direction, North pole versus South pole. Possible paths for future research in this area and its compatibility with existing methods based on chiral electrodes are discussed.

5.1 Introduction

5.1.1 Electric field induced spin polarization

In addition to spin-filtering via the CISS effect, recent studies show that charge polarization of a chiral molecule is accompanied by spin polarization. That is, a rearrangement of the electron distribution within a chiral molecule can generate both an electrostatic moment (transient electric dipole) and a spin moment (transient magnetic moment). Kumar *et al*. showed this phenomenon by measuring the spin polarization created in a monolayer film of chiral molecules as a function of a bias voltage applied on the monolayer.[1] Using a Hall bar device, as the working electrode in an electrochemical cell, they adsorbed a monolayer film of oligopeptides on the electrode surface and measured the magnetization that is generated as the double layer of the electrode is charged and discharged. Importantly, they showed that the sense of the magnetization, the sign of excess spin associated with each electric pole of the molecules in the layer, depends on the enantiomeric form of the chiral molecule. This effect can play an important role in collisions between chiral molecules or between chiral molecules and ferromagnetic surfaces. It is important to appreciate, that this spin polarization is a transient effect; however the collision times between molecules are typically much shorter than the spin depolarization time (sub-nanoseconds versus microseconds)[2-3] so that the spin polarization during the collision can be defined according to the handedness of the molecule through many collisions.

Consider a chiral molecule in a singlet state; the application of an electric field on the molecule or the molecule's interaction (or collision) with other molecules, causes an electronic rearrangement (induced electron polarization), and this charge reorganization is accompanied by transient partial spin polarization (see Figure. 5.1A). The spin polarization is such that one excess spin density is associated with one pole of the induced electric dipole and the opposite excess spin density is associated with the opposite pole of the induced electric dipole. Which spin is associated with which electric pole depends on the handedness of the molecule,[1] and the total spin of the system is still zero. The anisotropic spin density can affect the interaction energy between chiral molecules, and it is enantiospecific.

The schematic diagram in Figure. 5.1A(ii) illustrates an enantiospecific mechanism for the instantaneous dipole – induced dipole force (dispersion force) acting between two, closed shell, chiral molecules. The blue shaded region indicates the electron cloud of the molecule and the helix shows the molecular chirality (either left-handed or right-handed). For homochiral molecules interacting head-to-tail, their electron clouds in the overlap region (represented by the dashed circle) have opposite spin orientations (indicated by the red circles with arrows); Figure. 5.1A(iii). This interaction can be viewed as having singlet character so that Pauli exclusion (electrons in the same spatial orbital must be spin paired) is satisfied. Conversely, Figure. 5.1A(iv) shows a heterochiral interaction between two chiral molecules. In this case, the excess spin densities for the two molecules have the opposite sense (shown in the diagram by outward and inward red arrows, respectively), so that the spin orientations are aligned (display a triplet character) as the molecules collide. Because the singlet surface is less repulsive than the triplet one, an enantiospecific interaction is created. This spin interaction is a relatively short-range effect (resulting from the exchange interaction for electrons in orbitals) and only becomes important for molecules in intimate "contact", overlapping electron clouds. This schematic example makes it clear that a difference in energy exists between homochiral versus heterochiral interactions, even without inclusion of steric effects. Moreover, in chiral structures, much of the total energy difference can result from the Pauli exclusion. Namely, the difference in energy is mostly determined by the spin-exchange energy, and it can easily exceed the available thermal energy (kT) at room temperature.

5.1.2 Interaction of chiral molecules with ferromagnetic surfaces

The CISS effect implies that chiral molecules will interact enantiospecifically with a ferromagnetic surface, and the scheme in Figure. 5.1B illustrates a mechanism for it. As a chiral molecule approaches an electrode surface, it becomes charge-polarized and spin-polarized, which affects the nascent bond formation. If the electrode is magnetized perpendicular to the surface (along the surface normal), then it will have a spin-dependent interaction with the spin-polarized chiral molecules. That is, the excess of electron spins oriented along the surface normal will bind preferentially to chiral molecules whose spin polarization is opposite to that of the surface (singlet-like) than to the aligned case (triplet-like). As before, for fermions the exchange interaction is governed by the Pauli exclusion principle, which requires that two electrons have opposite spins in order to occupy the same spatial orbital. The phenomenon is very much like the case of the two interacting chiral molecules (Figure. 5.1A), except now one of the chiral molecules is replaced by an electrode surface whose spin orientation is controlled by its magnetization direction; and the orbitals are forming a bond, chemisorption. From these considerations, it follows that molecules of one enantiomer have a propensity to bind more readily than the other with a magnetized (spin-polarized) ferromagnetic electrode, because their spin polarization is already favorable. Banerjee-Ghosh, et al.[4] showed that the adsorption rate of chiral molecules onto a structurally achiral, but magnetized, substrate was enantiospecific. They showed that changing the magnetization direction of the ferromagnetic surface from Up to Down changed whether the left- or right-handed enantiomer adsorption was preferred, and that the selectivity required a direct interaction with the magnetized surface. In 2019, Tassinari et al.[5] extended these ideas to the enantiospecific crystallization of amino acids with magnets, generating enantiopure (>80%) crystals. See recent review articles on CISS and enantio-separations.[6] It is important to appreciate that this effect is not a magnetic field effect, but rather it depends on the molecule's electron cloud overlapping with the electron density in the magnet (an exchange energy effect). The spin polarization, which accompanies charge polarization and the enantiospecificity that arises from it, has important implications for chiral separations and for chemical reactions of chiral molecules.

These features of chiral molecule/ferromagnetic surface interactions were confirmed recently in three different reports. Ghosh et al.[7] used Kelvin probe measurements to show that the electron penetration (tunneling) from a ferromagnetic electrode into adsorbed chiral molecules depends on the ferromagnet's magnetization direction, the magnetization strength, and the handedness and length of the chiral molecules. They observed contact potential differences as large as 100 mV for the two different enantiomeric forms on magnetized Co film electrodes. The interaction depends sensitively on whether the magnetization of the Co films was oriented along the surface normal, or not. In a separate study, Ziv et al. probed the enantiospecificity by measuring the interaction force between a chiral oligopeptide and a ferromagnetic surface using atomic force microscopy. In their study, they found a difference in the interaction energy, on the order of 100 meV (about 10 kJ mol−1), for a ferromagnetic substrate magnetized in opposite directions.[8] This value is consistent with former calculations[4] and is much larger than thermal energy fluctuations at room temperature, therefore it should dominate the interaction of chiral molecules in the short range. Weiss and co-workers showed that the photoinduced ionization of chiral molecules,[9] which are adsorbed on ferromagnetic surfaces, display a binding energy shift that changes with the enantiomeric form of the molecule and the direction of magnetization. Together, these studies make a compelling case that magnetized electrodes, which are structurally achiral, can interact enantiospecifically with chiral molecules.

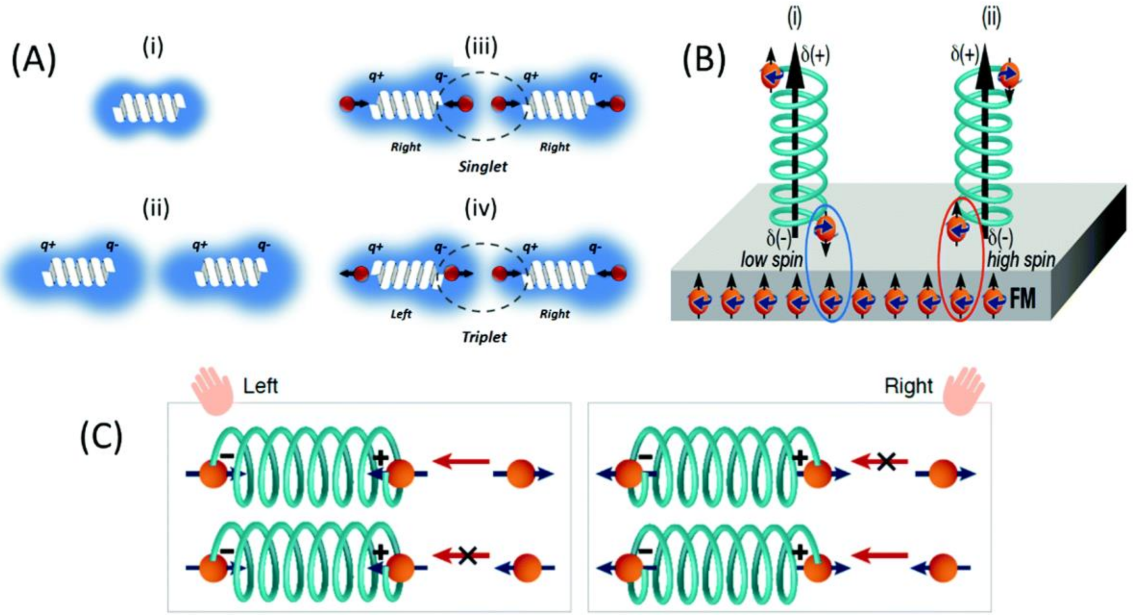

Figure 5.1 Schematics for the manifestations of the chiral induced spin dependent charge polarization effect in different systems. (A) The diagram shows the electron distribution (blue cloud) in a closed-shell, chiral molecule which does not have a dipole moment before (i) and after (ii) it interacts with another such molecule. The interaction creates an asymmetry in the electrons' charge distribution, resulting in an "induced dipole" in each molecule. (iii) This diagram illustrates the induced dipole interaction of two such molecules with the same handedness. As charge q transfers from one side of the molecule to the other, it generates a spin polarization (represented by a red ball and black arrow) of the same spin in the two molecules. Because the induced-dipoles of the two molecules are oriented head-to-tail the spin polarization at the interface of the two molecules is opposite, antiparallel, indicated by the dotted circle region. This is characterized as a singlet interaction. For two interacting molecules of opposite chirality (iv), the interaction between the molecules is characterized by two spins parallel to each other (dotted circle region) and is assigned as a triplet interaction. (Reproduced from ref. [1] with permission from the National Academy of Sciences). (B) The scheme illustrates the process occurring when a right-handed (i) or left-handed (ii) chiral molecule approaches a ferromagnetic substrate. The spin alignment at the group pointing towards the surface and the magnetization direction of the surface determine the interaction (Reproduced from ref.[4] with permission from American Association for the Advancement of

Science). (C) This scheme illustrates the spin polarization induced enantioselective reaction mechanism. When an electron approaches a chiral molecule, charge rearrangement occurs and the molecule becomes charge polarized with the electron attracted to the positive pole of the molecule. Depending upon the molecule's handedness (i left-handed and ii right-handed) and the spin orientation of the electron, the interaction is more favored or less favored.

5.1.3 Enantioselectivity on magnetized electrodes

An important chemical manifestation of the CISS effect is illustrated schematically by Figure. 5.1C; a process that can be described as a spin-polarization induced enantioselective reaction. As an electron approaches a molecule, charge rearrangement occurs within the molecule to accommodate the presence of the negatively charged electron. For chiral molecules, this charge polarization generates a spin polarization that depends on the enantiomeric form of the molecule. If the electron that is approaching the chiral molecule is spin polarized, *e.g.* coming from a magnetized ferromagnetic substrate, it interacts selectively with the excess spin density on the positive pole of the chiral molecule; if the spins are aligned antiparallel it is singlet-like and if they are parallel it is triplet-like. Because the excess spin density on the chiral molecule's positive pole depends on its enantiomeric form, the interaction is again enantiospecific. This proposed mechanism implies that the electron's helicity (spin direction along the electron velocity vector) provides the ‘chiral bias’.

Metzger *et al.*[10] reported three examples of enantioselective reactions at magnetized electrodes: the kinetic resolution of a racemate via electroreduction, the enantioselective adsorption onto an achiral spin-polarized host site, and the electropolymerization of chiral films from achiral monomer units.

5.2 Kinetic-resolution by electroreduction

This study used an achiral magnetized working electrode (Figure. 5.2) to selectivity decompose one enantiomer of camphorsulphonic acid over the other.[10] A diagram illustrating the electrochemical cell design used in these studies is shown in Figure. 5.2A, and Figure. 5.2B shows the overall electrochemical reaction in which a racemic solution of camphorsulfonic acid (CSA) was enantioselectively reduced to produce isoborneol. Figure. 5.2C and D show cyclic voltammograms taken for pure enantiomers of CSA under different (Up (red) and Down (blue)) magnetizations. Figure. 5.2C reveals a larger faradaic current for the *S*-enantiomer when the magnetization is polarized Up as compared to that when it is polarized Down. In contrast, Figure. 5.2D shows that the faradaic current for the *R*-enantiomer is lower when the magnetization is Up than when it is Down. From these data, it is clear that the current, *i.e*. reaction efficiency, for each enantiomer depends on the magnetization state of the electrode. Experiments in which the substrate was coated with a 1-hexanethiol self-assembled monolayer gave similar results and imply that the enantioselectivity is associated with the helicity of the electron, rather than an enantiospecific surface-confined interaction between the molecule and the ferromagnetic electrode.

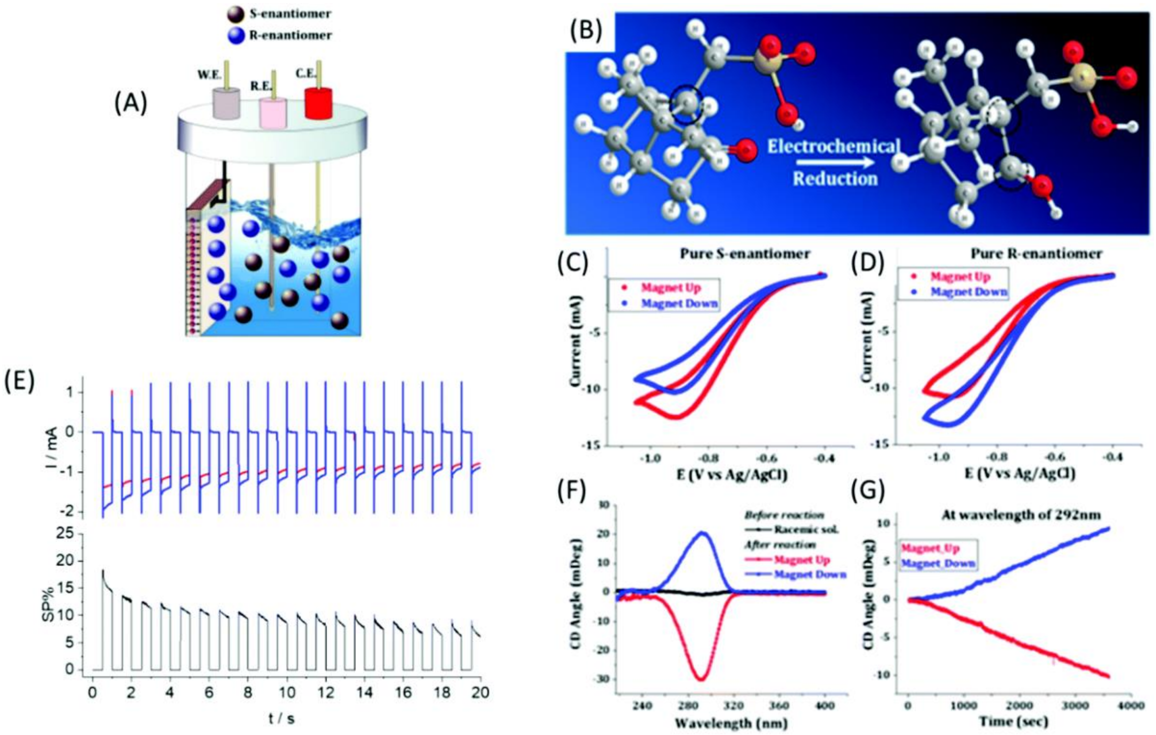

Figure 5.2 The electrochemical reaction cell is illustrated, in which the magnetized ferromagnetic electrode has spins oriented normal to the electrode surface. The *R*- and *S*-enantiomer (blue and grey spheres) are in the solution. (B) The electroreduction reaction is the conversion of camphorsulfonic acid (CSA) to 10-mercaptoborneol on magnetized nickel electrodes. (C and D) Cyclic voltammograms are shown for (*S*)- and (*R*)-CSA with a Ni electrode magnetized in the Up (red) and Down (blue) orientation. (E) The measured current–time profile is shown for an *S*-CSA solution at −0.9 V with pulses of 0.5 s duration when the magnet is pointing up (red) or down (blue). In the bottom plot the difference in the polarization as a percentage (SP%) is plotted. (F) Circular dichroism (CD) spectra of the solution following electroreduction is shown for the magnetic electrode pointing Up (red) or Down (blue); the black spectrum shows the CD of the racemate mixture before the reaction. (G) The change in the CD peak at 292 nm as a function of reaction time for the magnet oriented Up (red) and Down (blue) is shown. (Reproduced from ref.[11] with permission from John Wiley and Sons).

The unreacted CSA in the solution was quantified using mass spectrometry, NMR, and circular dichroism spectroscopy. The changes in the CD spectrum at 292 nm (Figure. 5.2F), which corresponds to a change in the enantiomeric excess of the solution were found to depend on the orientation of the applied external magnetization during the electroreduction. When the electrode is magnetized Up (red), the CD signal is negative; and when the electrode is magnetized Down (blue), the CD signal is positive. Figure. 5.2G shows the change in the intensity of the CD peak at 292 nm as a function of time, for the two different magnetization directions. An enantiomeric excess of 10–15% was achieved following 6 hours of electroreduction.

Figure. 5.2E shows the current resulting from the application of a pulsed-potential waveform which was used for the reduction of a 20 mM *S*-CSA solution. In contrast to the data in the other panels, the data in panel 5.2E have not been previously published. The potential was stepped between −0.9 V and 0.0 V vs. Ag|AgCl every 0.5 s, with an external magnetic field oriented Up (red) or Down (blue) parallel to the electrode's surface normal. A difference in the current was observed for the two magnet orientations. For the *S* enantiomer, the current remains higher for the Down magnetization of the electrode (magnetization vector pointing towards the solution) than for the Up direction, but the difference in the currents decreases as the reaction proceeds. In fact, the enantioselectivity, as measured by the polarization ($\mathrm{SP} = \frac{I_{down} - I_{up}}{I_{down} + I_{up}} \times 100$ is the spin polarization percentage) decreases with time, when I_{down} and I_{up} are the currents measured with the magnetic pole pointing Up or Down respectively. Thus, both the overall reaction yield (total current) and the enantioselectivity (SP%) decrease with time. XPS analysis of the electrode, following the reaction, indicates that the sulfonate on some of the CSAs are reduced to thiols which can bind to the electrode's surface and cause a decrease in the reaction yield and the enantioselectivity.

As shown by the data in Figure. 5.2E, electrode fouling and degradation of the spin selectivity over time will be an important consideration for practical applications. For the CSA system, the decrease in spin selectivity arises from the electrode being coated with thiols that reduce the spin polarization of the electrons ejected from the magnetic substrate. One expects that an important limitation on the enantioselectivity of the electrochemical process will be the extent of spin polarization of the electrons ejected from the electrode in the reduction process, or the spin polarization of the electrons injected into the electrode for an oxidation process.

5.3 Enantioselective adsorption with achiral host sites

Another approach towards asymmetric synthesis is to use a ferromagnetic substrate to control enantioselective association of chiral molecules with an achiral self-assembled monolayer film that is spin-polarized. In one example, the achiral self-assembled monolayer (SAMs of carboxyalkanethiols) were spin polarized by a magnetized ferromagnetic substrate (Ni (50 nm)/Au (10 nm)) because of the proximity effect.[12] In ref.[10], the enantiospecific adsorption of 1-amino-2-propanol was used to collect an enantiomeric excess of about 20% by applying up and down magnetizations of the substrate. The same effect was observed for achiral naphthylthiol SAMs adsorbed on Au/Ni ferromagnetic substrates and exposed to solutions of 1-phenylethanol in ethanol, indicating that the enantiospecificity manifests for π–π interactions. Figure. 5.3 presents the IR transmission spectrum and the association rate (inset) for Up and Down magnetization of the substrate. The spectrum is taken at the O–H stretching mode, 3340 cm^{-1}. The data show that the association rate depends on the magnetization direction; the Down magnetization displays significantly more association.

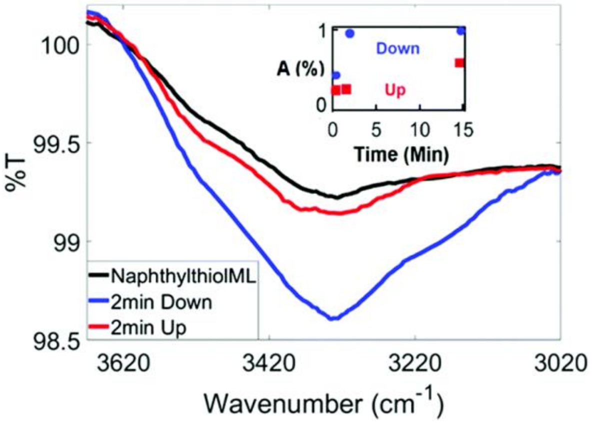

Figure 5.3 The *π*–*π* bonding association rate of *R*-1-phenylethanol to a naphthylthiol monolayer film for Up and Down magnetization of the Ni/Au substrate. FTIR is used to monitor the association process *via* the O–H stretching mode at 3340 cm^{-1}, the association process can be followed. After 2 minutes, for down magnetization (blue) a full layer was created, while for Up magnetization (red) small changes were measured as compared to the SAM only (black). The inset shows the rate for Up (red) and Down (blue) at different times.

5.4 Enantioselective electropolymerization from achiral monomers

Asymmetric electrochemical reactions with spin polarized electrons do not require that the reactant molecules possess chirality, because the electron's helicity can evoke chirality in the reaction products. Figure. 5.4 shows data for the growth of chiral polymers from achiral monomers. In this case, a Ni/Au ferromagnetic electrode is used to electropolymerize achiral monomers into a chiral polymer that is probed by circular dichroism spectroscopy of the polymer film. Panels A, B, and C, show absorbance spectra of electropolymerized pyrenecarboxylic acid, carbazole, and 3,4-ethylenedioxythiophene thin films respectively; and panels D, E, and F show their corresponding circular dichroism spectra. The handedness of the polymer thin film is determined by the orientation of the magnet (Up (red) or Down (blue)) that is used to magnetize the electrode. Note that the polypyrene data shown in panels A and D are taken from ref. 10, and the data for polycarbazole and PEDOT are unpublished data; see Appendix D for details on those experiments.

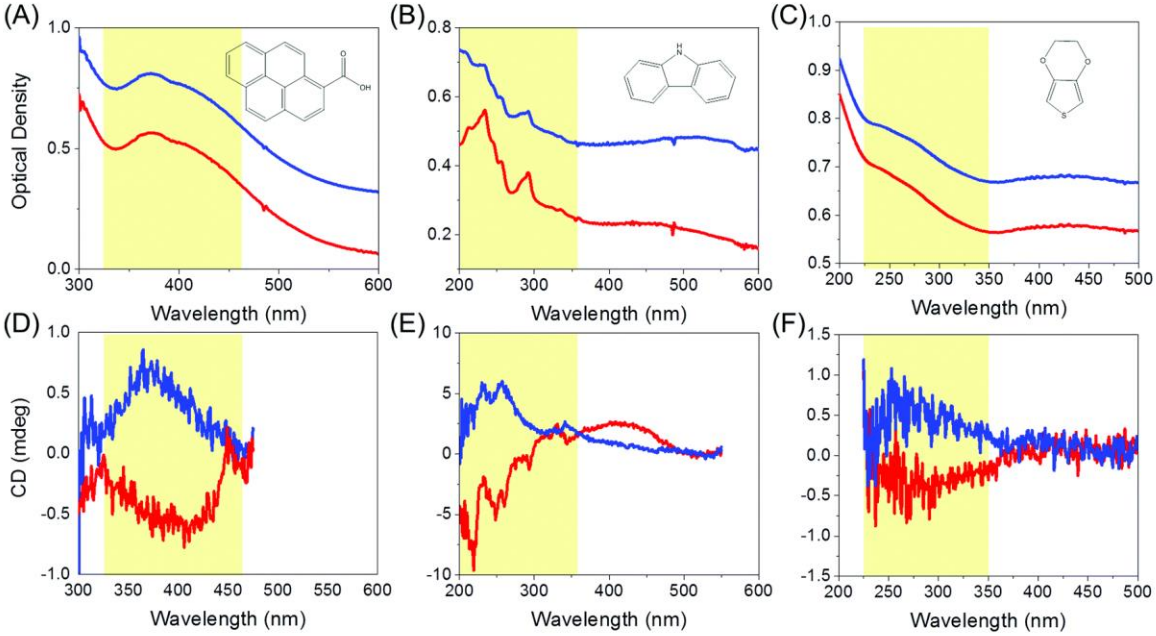

Figure 5.4 Absorbance (A, B and C) and circular dichroism (D, E and F) spectra of electropolymerized thin films using pyrenecarboxylic acid (left), carbazole (middle), and 3,4-ethylenedioxythiophene (right) monomers with a magnetic field applied Up (red) or Down (blue) during polymerization. The inset shows the molecular structure of the monomer and the absorbance spectra in the upper panels are offset from one another for clarity. The yellow highlighted region illustrates the electronic transitions in which chirality is present. (The data in panels A and D) are reproduced from ref.[10] with permission from John Wiley and Sons), whereas the other data are new (see text).

Although a mechanism for how chirality manifests in these electrochemical polymerization reactions has not yet been elucidated, it is possible to make a conjecture based on the CISS effect and spin-dependent charge polarization ideas. All three monomers have been reported to form a radical cation intermediate upon electro-oxidation.[13] Given that the monomers are not chiral, the polymerization at early time likely creates equal amounts of right- and left-handed dimers (and small *n*-mers) at the surface, but as the reaction proceeds the electron's helicity and the delocalization of the spin-polarized electrons from the substrate into the small *n*-mers could control the reactivity of the different enantiomers. Thus, the propagation of the polymerization reaction would depend on the orientation of the electron spin, which is controlled by the electrode's magnetic moment direction, and would favor the formation of one enantiomer over the other in a manner that depends on the electrode's magnetization. The chirality indicates regularity in the polymer's secondary structure and thus, can be viewed as an additional order parameter controlled by spin injection. The precise control over orientation can facilitate improved charge-carrier mobility which may be important in optoelectronic and electronic applications.[11]

The electropolymerization reactions have some additional constraints on the enantiomeric excess (ee) that will need to be considered. For example, the initial stage of generating the radical cation and its association with the substrate, or not, will strongly affect the efficiency and enantioselectivity of the process. While the presentation in Figure. 5.4 is intended to show the generality of the approach, it is evident that the carbazole data display a much more significant circular dichroism signal than is found for the other two monomers. Moreover, the thickness of the film is likely to place an important constraint on the ee for these reactions. As the film thickness grows, the likelihood of electron scattering and spin depolarization increases; thus, one expects that the enantioselectivity will degrade as the electrons being extracted from the growing polymer randomize their spins more effectively.

These findings imply that the introduction of enantioselectivity into chemical reactions by the electron spin is general and point to the possibility of synthesizing complex chiral structures with multiple chiral centers on surfaces using several steps while controlling both the electric and magnetic fields of the surface. This can be achieved by multiple stages of association each done under different magnetic field and electric field orientations of the substrate.

5.5 Synopsis and future directions

The two chemical reaction classes described above, spin-selective chemistry on chiral electrodes and enantioselective (asymmetric) electro-organic reactions on magnetized electrodes, originate from the enantiospecificity that arises from the spin selective interaction of chiral molecules with electrons, the CISS effect.

5.5.1 Spin-selective chemistry

In nature, many redox reactions occur *via* multiple electron processes. In these cases, the relative spin of the electrons involved may determine the reaction paths and/or the production of by-products. The water splitting reaction, discussed above, is one example. It can be expected that by controlling the spin of the electrons one will be able to increase the efficiency of multi-electron redox reactions and define better the product. Possible candidates for such studies are for example CO_2 reduction and hydrocarbon redox processes.

Spin constraints on chemical reactions has a long history, however it is rare that those studies include chiral molecules.[14-16] The importance of the electron spin in understanding radical pair formation and recombination is well appreciated, and Wasielewski has explored the importance of spin effects in a range of different model systems.[17] In photosynthesis, which contains chiral constituents, the radical pair formation in the photosynthetic reaction (PSI) generates a non-Boltzmann spin distribution (is spin polarized).[18] What role CISS might contribute to this phenomenon is not yet certain, but experiments show that spin polarization exists in the charge transfer of PSI assemblies on electrodes.[19] Many other biochemical and enzymatic reactions necessarily involve chiral molecules but their study from the viewpoint of CISS is largely unexplored.

5.5.2 Asymmetric reactions

The studies of enantioselective reactions with magnetized electrodes promise a wholly new approach for asymmetric synthesis in which the chiral bias in the reaction comes from the electron spin. This feature is shown most explicitly in the electropolymerization studies, in which none of the reactants possess structural chirality, but is also evident in the other two examples given above. Importantly, these studies demonstrate how chirality can emerge from an achiral system and may offer yet another alternative explanation for the origin of homochirality and its prevalence in biological systems. More generally, these studies show that magnetized ferromagnetic substrates can be used to break the symmetry of chemical reactions and create products with an enantiomeric excess.

At this time only a few cases of spin-induced asymmetric electrochemical processes have been demonstrated. While the CISS based mechanism described in Figure. 5.2 implies that the phenomenon should be general, much needs to be explored and learned before the breadth and implications of this approach will become wholly clear. Even in cases where the enantioselectivity is not very high, it may prove possible to enhance the enantiomeric enrichment by amplification methods.[20-21] The approach of using spin polarized electrons from a magnetized electrode is general and its coupling with other ways of introducing chiral bias should be possible. Thus, this approach may improve the performance of existing chiral electrodes, by using a magnetic electrode material and providing the appropriate magnetic field to raise their enantioselectivity.

5.5.3 What is needed to realize the field's promise?

Many basic issues about what parameters affect the enantioselectivity and how to quantify them remain to be elucidated. The question is complex because it involves several entangled processes: the electrochemical reaction (including the role of the double layer and the diffusion rate), the spin selectivity of the elementary electrochemical redox steps, and the possible secondary reactions of the products produced in the initial stages of the process. For example, consider the enantioselective reactions with racemic mixtures, like that shown in Figure. 5.2. For such reaction processes, there is a growing increase in concentration of the "unfavored enantiomer" with time, as a result of depletion of the favored enantiomer by the enantiospecific electrochemical reaction. Hence, eventually the kinetics are expected to become nonspecific, and an inherent limit will be placed on the enantiomeric excess that can be achieved. The limit depends of course on the extent of spin specificity in the fundamental electrochemical steps, but for the system considered in Figure. 5.2 it seems that an ee exceeding 20% is not realistic. The situation is wholly different for the case in which a chiral product can be generated from an achiral one, like the case of the polymerization described above. In this case the ee depends mainly on the spin selectivity of the redox process.

A better understanding of the intrinsic spin selectivity of the redox process and the CISS effect will prove to be key in advancing this area. Establishing structure–function relationships for the CISS effect will provide key guidance for making progress. While theoretical models for the CISS effect have made significant progress over the past decade and make important qualitative predictions, quantitative comparisons with measured spin-filtering responses of molecules reveal a significant gap in our theoretical description/understanding.[22] Theory and experiment have both shown that the CISS response increases with the length of helical molecules (over the range of a few nm), but other connections are lacking. For example, experiment shows a correlation between a molecule's chiro-optical response and its CISS response, but the theory has not yet been developed for this. Even ‘simple’ questions, such as how the CISS response scales with the number of chiral centers, or the importance of axial chirality, remain to be addressed by a comparison of theory and experiment. These various issues, and more, must be studied in detail in order to understand how to optimize the ee for electrochemical reactions.

In addition to a deeper theoretical understanding of CISS for molecules, it will prove important to have a deeper and predictive understanding of molecule/ferromagnetic surface interactions, the ‘spinterface’.[23]90 A term more popular in the physics and spintronics communities, the spinterface refers to the spin-dependent orbital interactions of molecules and ferromagnetic surfaces that can give rise to spin-polarized electron transport, even with achiral molecules.[24] The interaction of chiral molecules with ferromagnetic surfaces promise to reveal additional complexities arising from the rich (complex), spinterface interactions in combination with the CISS response.

Beyond a better chemical understanding of the reaction mechanism and process variables, it will be important to create stronger and more chemically robust magnetic electrodes. In addition to creating magnetic films with strong magnetization (large energy differences in the spin sublevels), the magnetic electrodes must be chemically stable in the working electrochemical cell conditions and the spin polarization has to be out-of-plane. Such considerations limit the materials that can be used, and this will be a future challenge for this nascent research field.

The elements described above, including improved control over process variables, better magnetized film electrodes, structure–function relationships for CISS, and a deeper understanding of ferromagnetic-molecule orbital interactions, will provide the foundation for developing this new area. A promising feature of the CISS-based approach is its generality and compatibility with established strategies for introducing chiral bias in electrochemical reactions. Progress on these fronts will enable the improvement of electrosynthetic methods that increase ee and reveal whether it will be possible to introduce multiple chiral elements into electrosynthesis in a controlled way. Even if the ability to further develop molecular complexity is limited, spin-selective electrosynthesis promises to become an important tool in the synthetic chemist's toolbox for obtaining pure enantiomers. From a wider point of view, CISS considerations may prove to be important for expanding our understanding of biochemical processes and the effects of chiral molecular compounds in chemical biology.

5.6 Reference

1.Kumar, A.; Capua, E.; Kesharwani, M. K.; Martin, J. M.; Sitbon, E.; Waldeck, D. H.; Naaman, R., Chirality-induced spin polarization places symmetry constraints on biomolecular interactions. *Proceedings of the National Academy of Sciences* **2017,** *114* (10), 2474-2478.

2.Prisner, T.; Rohrer, M.; MacMillan, F., Pulsed EPR spectroscopy: biological applications. *Annual review of physical chemistry* **2001,** *52* (1), 279-313.

3.Kawai, A.; Shibuya, K., Electron spin dynamics in a pair interaction between radical and electronically-excited molecule as studied by a time-resolved ESR method. *Journal of Photochemistry and Photobiology C: Photochemistry Reviews* **2006,** *7* (2-3), 89-103.

4.Banerjee-Ghosh, K.; Ben Dor, O.; Tassinari, F.; Capua, E.; Yochelis, S.; Capua, A.; Yang, S.-H.; Parkin, S. S.; Sarkar, S.; Kronik, L., Separation of enantiomers by their enantiospecific interaction with achiral magnetic substrates. *Science* **2018,** *360* (6395), 1331-1334.

5.Tassinari, F.; Steidel, J.; Paltiel, S.; Fontanesi, C.; Lahav, M.; Paltiel, Y.; Naaman, R., Enantioseparation by crystallization using magnetic substrates. *Chemical science* **2019,** *10* (20), 5246-5250.

6.Naaman, R.; Paltiel, Y.; Waldeck, D. H., Chirality and spin: A Different perspective on enantioselective interactions. *Chimia* **2018,** *72* (6), 394-394.

7.Ghosh, S.; Mishra, S.; Avigad, E.; Bloom, B. P.; Baczewski, L.; Yochelis, S.; Paltiel, Y.; Naaman, R.; Waldeck, D. H., Effect of chiral molecules on the electron's spin wavefunction at interfaces. *The journal of physical chemistry letters* **2020,** *11* (4), 1550-1557.

8.Ziv, A.; Saha, A.; Alpern, H.; Sukenik, N.; Baczewski, L. T.; Yochelis, S.; Reches, M.; Paltiel, Y., AFM - Based Spin - Exchange Microscopy Using Chiral Molecules. *Advanced Materials* **2019,** *31* (40), 1904206.

9.Abendroth, J. M.; Cheung, K. M.; Stemer, D. M.; El Hadri, M. S.; Zhao, C.; Fullerton, E. E.; Weiss, P. S., Spin-dependent ionization of chiral molecular films. *Journal of the American Chemical Society* **2019,** *141* (9), 3863-3874.

10.Metzger, T. S.; Mishra, S.; Bloom, B. P.; Goren, N.; Neubauer, A.; Shmul, G.; Wei, J.; Yochelis, S.; Tassinari, F.; Fontanesi, C., The electron spin as a chiral reagent. *Angewandte Chemie* **2020,** *132* (4), 1670-1675.

11.Chu, P.-H.; Kleinhenz, N.; Persson, N.; McBride, M.; Hernandez, J. L.; Fu, B.; Zhang, G.; Reichmanis, E., Toward precision control of nanofiber orientation in conjugated polymer thin films: Impact on charge transport. *Chemistry of Materials* **2016,** *28* (24), 9099-9109.

12.Leutenantsmeyer, J. C.; Kaverzin, A. A.; Wojtaszek, M.; Van Wees, B. J., Proximity induced room temperature ferromagnetism in graphene probed with spin currents. *2D Materials* **2016,** *4* (1), 014001.

13.Waltman, R.; Bargon, J., Electrically conducting polymers: a review of the electropolymerization reaction, of the effects of chemical structure on polymer film properties, and of applications towards technology. *Canadian Journal of Chemistry* **1986,** *64* (1), 76-95.

14.Usharani, D.; Janardanan, D.; Li, C.; Shaik, S., A theory for bioinorganic chemical reactivity of oxometal complexes and analogous oxidants: the exchange and orbital-selection rules. *Accounts of Chemical Research* **2013,** *46* (2), 471-482.

15.Buchachenko, A.; Lawler, R. G., New possibilities for magnetic control of chemical and biochemical reactions. *Accounts of Chemical Research* **2017,** *50* (4), 877-884.

16.Steiner, U. E.; Ulrich, T., Magnetic field effects in chemical kinetics and related phenomena. *Chemical Reviews* **1989,** *89* (1), 51-147.

17.Wasielewski, M. R., Energy, charge, and spin transport in molecules and self-assembled nanostructures inspired by photosynthesis. *The Journal of organic chemistry* **2006,** *71* (14), 5051-5066.

18.Thurnauer, M. C.; Katz, J. J.; Norris, J. R., The triplet state in bacterial photosynthesis: Possible mechanisms of the primary photo-act. *Proceedings of the National Academy of Sciences* **1975,** *72* (9), 3270-3274.

19.Carmeli, I.; Kumar, K. S.; Heifler, O.; Carmeli, C.; Naaman, R., Spin selectivity in electron transfer in photosystem I. *Angewandte Chemie International Edition* **2014,** *53* (34), 8953-8958.

20.Soai, K.; Sato, I., Asymmetric autocatalysis and its application to chiral discrimination. *Chirality: The Pharmacological, Biological, and Chemical Consequences of Molecular Asymmetry* **2002,** *14* (7), 548-554.

21.Mathew, S. P.; Iwamura, H.; Blackmond, D. G., Amplification of enantiomeric excess in a proline‐mediated reaction. *Angewandte Chemie International Edition* **2004,** *43* (25), 3317-3321.

22.Naaman, R.; Paltiel, Y.; Waldeck, D. H., Chiral molecules and the spin selectivity effect. *The journal of physical chemistry letters* **2020,** *11* (9), 3660-3666.

23.Bergenti, I.; Dediu, V., Spinterface: A new platform for spintronics. *Nano Materials Science* **2019,** *1* (3), 149-155.

24.Oppeneer, P. M.; Panchmatia, P. M.; Sanyal, B.; Eriksson, O.; Ali, M. E., Nature of the magnetic interaction between Fe-porphyrin molecules and ferromagnetic surfaces. *Progress in Surface Science* **2009,** *84* (1-2), 18-29.

6.0 Conclusion

This work shown in dissertation has explored the fundamental aspects of the Chiral Induced Spin Selectivity (CISS) effect on the enantiospecific spin exchange interaction between chiral molecules and magnetized ferromagnetic substrate. The projects discussed here are important for realizing CISS-based enantiomeric resolution, including enantioseparation and enantiosynthesis, and provide a new aspect of understanding homochirality and the origin of life.

Chapter 2 explores the fundamental principles which underpin the enantiospecficity of chiral molecules to magnetized ferromagnetic surfaces. Our work utilizes mEQCM method to probe the behavior of chiral molecule (cysteine) adsorption on ferromagnetic surfaces. Adsorption Isotherm measurements show that the free energy of adsorption does not change with cysteine chirality or the electrode magnetization state; e.g. it is not thermodynamic in origin. Conversely, the kinetics for adsorption show a significant dependence on the magnetic field direction and the handedness of the molecule. Concentration and pH dependence studies of the adsorption polarization illustrate that the separation efficiency is sensitive to the molecular binding geometry. This experiment defines the parameters important for realizing CISS-based enantiomeric resolution; a crucial process that will help determine if this technique is to become commercially viable.

Chapter 3 continues to explores the effect of ionization state, geometric structure, dipole orientation, and molecule-solvent interactions on the enantiospecific adsorption of chiral molecule on magnetized ferromagnetic surfaces using mEQCM method in conjunction with DFT calculations. Our studies suggest that geometric changes in the adsorbate, controlled by varying the solution pH, result in distinct changes in the asymmetry of effective adsorption rate constants with applied magnetization; i.e. the preferred applied magnetization for a large effective adsorption rate constant changes with pH. These findings are corroborated by pH-dependent DFT calculations which reveal changes in solvent-molecule interactions and adsorbate binding geometry. This work begins to bridge the knowledge gap between proof-of-principle separation measurements and the development of predictive measures for realizing spin-mediated chiral resolution.

Chapter 4 investigates the implications of electron spin pairing on the intermolecular interactions of biorecognition mimics. This work uses mEQCM method to probe the intermolecular interactions between chiral molecules; the adsorption of amino acids onto chiral N-acetyl-cysteine self-assembled monolayer coated ferromagnetic substrate. It shows that the spin-dependent exchange interactions is both kinetically and thermodynamically controlled, i.e. singlet-like vs. triplet-like interactions control the adsorption rate constant, as well as thermodynamically controlled surface energies, leading to differences in the amount of adsorbate on the different spin polarized surfaces. The spin-dependent phenomena occur in conjunction with traditional changes in intermolecular interaction energies associated with homochiral and heterochiral architectures. Moreover, the sign of the circular dichroism response of the adsorbate's interacting functional group is shown to be a good metric for predicting the spin preference of the interactions. These fundamental studies ought to be of great interest to the community of scientists attempting to elucidate a unified theory for the CISS effect and more broadly to the fields of biology and life-processes, as well as enantioseparations and pharmacology.

Chapter 5 describes two enantioselective chemical reactions and one enantioselective adsorption on magnetized ferromagnetic electrodes. The enantiospecificity arises from the spin selective interaction of chiral molecules with electrons, the CISS effect. The findings presented here demonstrate that it is possible to control the enantiospecificity in chemical reactions and intermolecular interactions of chiral molecules by manipulating the spin orientation. The spin polarization can be considered as a chiral bias which is able to induce asymmetry in both reduction and oxidation reactions. It provides a new strategy to perform enantioselective reactions from racemic or even achiral molecules.

Appendix A

Appendix A.1 EQCM system

The EQCM experiments were performed using a 7.9995 MHz quartz crystal with an EQCM cell attachment and a 430A potentiostat (CH Instruments). The surface area of the crystal is 0.205 cm^2 and is coated with 100 nm of nickel and 10 nm polycrystalline gold as the working electrode area (CH Instruments). The counter electrode was Pt wire and the reference electrode was a saturated Ag/AgCl electrode.

Appendix A.2 Underpotential deposition of Pb

To ensure the quartz crystal was functioning appropriately, underpotential deposition (UPD) experiments using lead were performed using a 5 mM of $Pb(ClO_4)_2$, 10 mM of $HClO_4$ and 0.1 M of $KClO_4$ solution, see Figure A.1. Cyclic voltammograms (left panel) from 0.24 V to -0.45 V versus saturated Ag|AgCl in tandem with the QCM showed that lead deposits and gives rise to a cathodic peak at -0.31 V and an anodic peak -0.2 V. The frequency change (right panel) was correlated to the mass of the UPD (63 ng) and corresponds to a coverage of $1.5 \times 10^{19}\ \mathrm{mol/cm^2}$, in agreement with other reports. The UPD measurements indicate that the EQCM is functioning accurately.

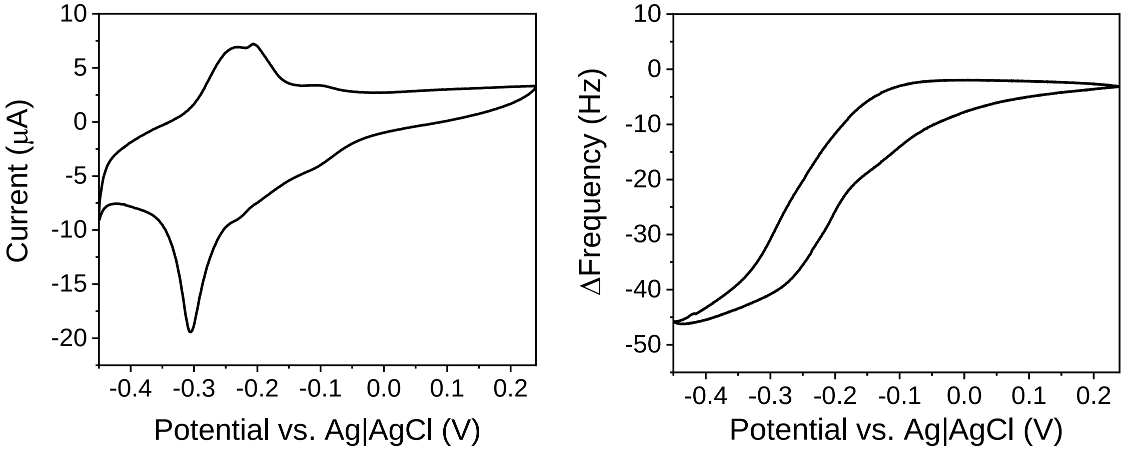

Figure A.1 The voltametric (left) and frequency (right) response of the QCM during the deposition of Pb.

Appendix A.3 Adsorption Isotherm

Cyclic voltammetry and QCM measurements were used to build the data for the adsorption isotherms. The data were collected by scanning from -0.4 V to - 1.1 V versus saturated Ag|AgCl at a scan rate = 25 mV/s. Unless specified all measurements were made in a pH 8 phosphate buffer solution. The frequency change from the 30th cycle, corresponding to the oxidative adsorption of cysteine on a gold substrate, was converted to a change in mass (Δm) according to the Sauerbrey equation by a factor of - 1.4 ng / Hz. The excessive amount of cycles was necessary to allow the instrument to reach equilibrium and give consistent results. Next, the mass change (Δm) or concentration/Δm was plotted versus concentration and fit to a Langmuir – Freundlich isotherm model or a linear isotherm.

Appendix A.4 Linearization derivation of isotherm.

Assuming that the adsorption is a reversible chemical reaction, the general form of adsorption isotherm can be expressed in a linear form:

$$\frac{c_{cys}}{\Delta m} = c_{cys} \cdot \frac{1}{\Delta m_{max}} + \frac{1}{K_{ads} \cdot \Delta m_{max}}$$

Thus, the maximum adsorption amount and the adsorption equilibrium constant K_{ads} can be calculated by the slope and intercept value of the linear plot. From the K_{ads}, the Gibbs free energy of the adsorption can be calculated by:

$$K_{ads} = \frac{1}{c_{solvent}} \cdot \exp\left(\frac{-\Delta_{ads}G}{RT}\right)$$

where $c_{solvent}$ is the concentration of the solvent, which is usually close to the concentration of pure solvent for low concentration solutions. Figure S2 shows a standard (left) and linearized (right) Langmuir isotherm for D-cysteine. The average $\Delta_{ads}G$ was found to be -34.3 ± 1.2 kJ/mol, -34.0 ± 1.0 kJ/mol and -34.2 ± 1.5 kJ/mol in three separate trials.

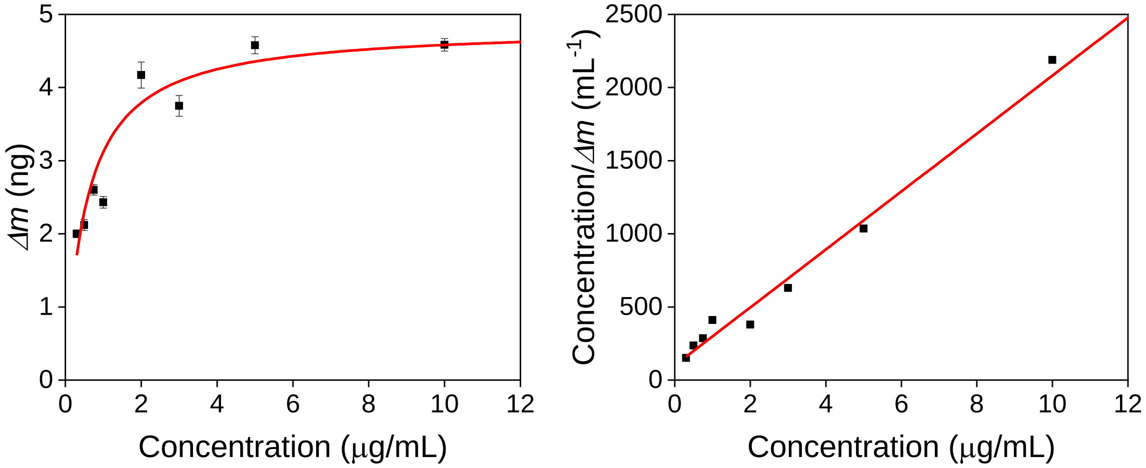

Figure A.2 The left panel shows an adsorption isotherm of D-cysteine using the change in mass determined from the cyclic voltammetry measurements at different cysteine concentrations. The red line is a Langmuir isotherm fit to the data. Right panel shows a linearized Langmuir isotherm plot of the same data in left panel.

Appendix A.5 Kinetic Experiments

The quartz crystal was first incubated in the cysteine solution for 1h to allow the system to equilibrate before applying a potential. Cyclic voltammograms (CVs) were recorded for 30 cycles (condition: - 0.4 V ~ - 1.1 V versus saturated Ag|AgCl, scan rate = 25 mV/s), as well as the frequency response of the quartz crystal, to ensure the surface was stable and the desorption and adsorption process was reversible. The chronoamperometry experiments were performed immediately after the CV acquisition with an initial potential of -0.8 V corresponding to reductive desorption of cysteine and then a more positive potential, -0.5 V, corresponding to oxidative adsorption. A 5 s pulse width was applied during the experiment and >150 cycles was performed to build up the statistics for the histogram plots. Unless specified, all measurements were made in a pH 8 phosphate buffer solution. The experiments with cysteine methyl ester used the same general procedure as cysteine, however in some instances additional time was required for the system to equilibrate. For these studies, an additional 30 CV cycles were collected.

Appendix A.6 Kinetic model derivation

Assuming a simple Langmuir model, the desorption rate can be written as

$$r_{des} = -\frac{d\theta}{dt} = k_{des} \cdot \theta \text{ or } \theta(t) = \theta_{t=0} \cdot \exp\left(-k_{des} \cdot t\right)$$

where θ is the concentration of adsorbed cysteine on the surface (filled surface sites or coverage) and k_{des} is the desorption rate constant. Thus, the rate constant extracted from the exponential fits for the desorption data correspond to k_{des}. For the case of adsorption, we can write the rate as

$$r_{ads} = \frac{d\theta}{dt} = k_{ads} \cdot c_{cys} \cdot (1-\theta) = k'_{ads} \cdot (1-\theta)$$

where c_{cys} is the concentration of cysteine in solution, k_{ads} is the adsorption rate constant and k'_{ads} is the effective adsorption rate constant.

To quantify the rates for the desorption and adsorption processes, the time responses of the QCM frequency were fit to an exponential growth equation $y = A \cdot e^{t/\tau_1} + y_0$ for desorption and an exponential decay equation $y = A \cdot e^{-t/\tau_2} + y_0$ for adsorption, where A, y_0, and τ_1 and τ_2 were adjusted for a best fit to the data. Then the desorption rate constant $k_{des} = \frac{1}{|\tau_1|}$, and the effective adsorption rate constant $k'_{ads} = \frac{1}{|\tau_2|}$.

Appendix A.7 Histogram of different concentrations

Figure S3 shows a histogram of k'_{ads} for D-cysteine (left) and L-cysteine (right) at different concentrations under a North (red) or South (blue) magnetic field. A summary of the rate data are shown in Table S1. These data were used to construct the polarization plot shown in the main text in Figure 3. Table S2 and S3 summarize the pH dependent rate data for L-cysteine and L-cysteine methyl ester.

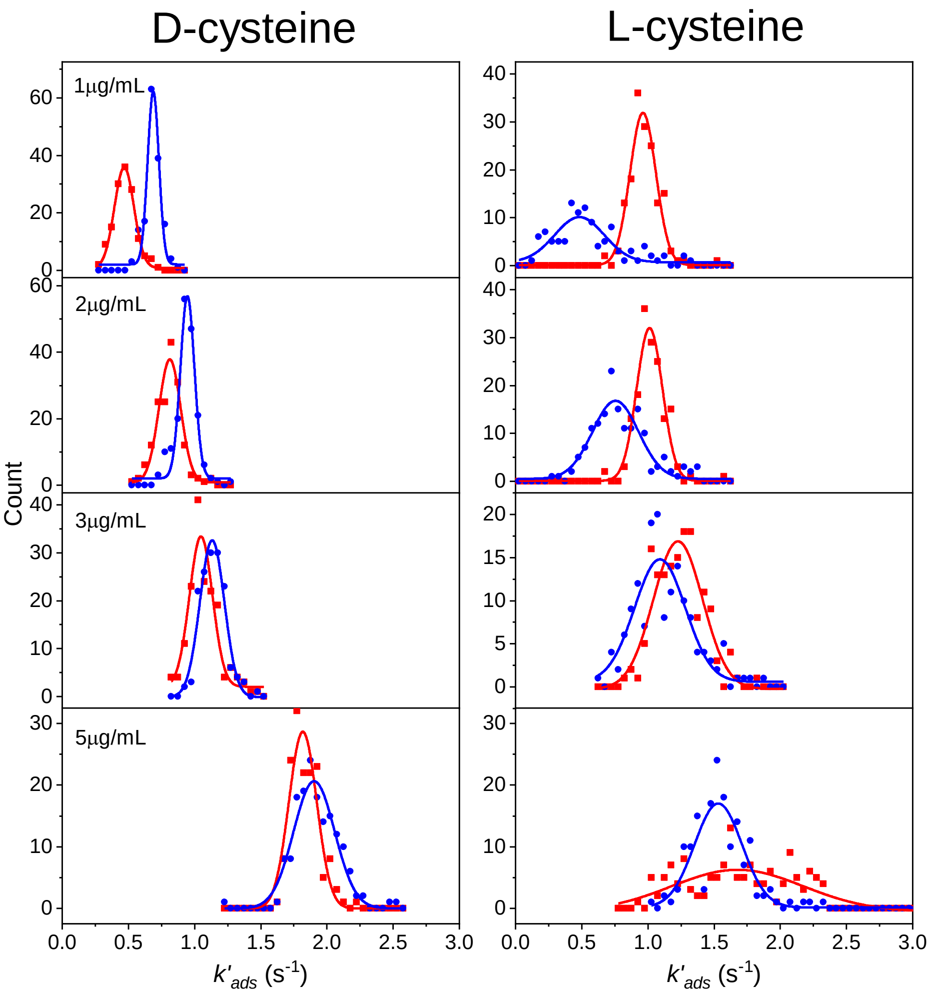

Figure A.3 The histogram of the adsorption rate of D-cysteine (left) and L-cysteine (right) under a North magnetic field (red) and South magnetic field (blue) at different concentrations. A best fit of the data using a Gaussian distribution is shown as a solid line.

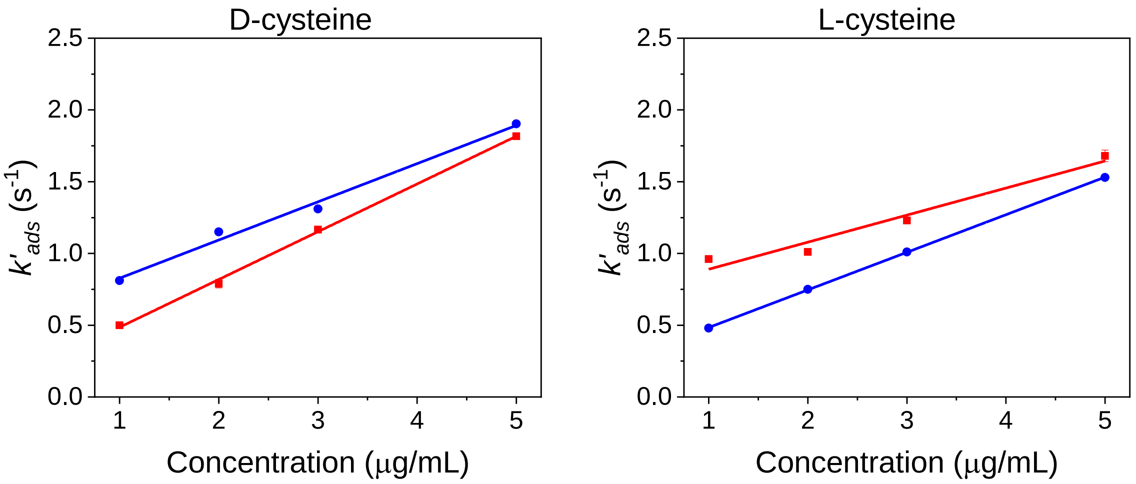

Figure A.4 The adsorption rate k'_{ads} is plotted as a function of the solution concentration for D-cysteine (left) and L-cysteine (right) under North magnetic field (red) and South magnetic field (red). The error bars show the standard deviation of the mean of the effective rate.

Figure S4 shows that there is a linear relationship between k'_{ads} and concentration for both D-cysteine (left panel) and L-cysteine (right panel) under North (red) and South (blue) magnetic field. For D-cysteine under a North (South) magnetic field k_{ads} was 0.33 mL μg^{-1} s^{-1} (0.27 mL μg^{-1} s^{-1}). Conversely, for L-cysteine k_{ads} under a North magnetic field and South magnetic field is 0.19 mL μg^{-1} s^{-1} and 0.26 mL μg^{-1} s^{-1}, respectively.

Table A.1 Summary of D-cysteine and L-cysteine adsorption rate constant and polarization

	D-cysteine			
Conc. (μg/mL)	k'_{ads} N (s^{-1})	k'_{ads} S (s^{-1})	P	$\sigma_{\bar{x}}$
1	0.50	0.81	23.7%	0.65%
2	0.79	1.15	18.5%	1.64%
3	1.17	1.31	-5.8%	0.36%
5	1.82	1.90	-2.3%	0.22%
	L-Cysteine			
Conc. (μg/mL)	k'_{ads} N (s^{-1})	k'_{ads} S (s^{-1})	P	$\sigma_{\bar{x}}$
1	0.96	0.48	33.3%	0.56%
2	1.01	0.75	14.8%	0.40%
3	1.23	1.01	9.8%	0.62%
5	1.68	1.53	4.5%	1.17%

Table A.2 Summary of 1 μg/mL L-cysteine adsorption rate constant and polarization at different pH

pH	k'_{ads} N (s^{-1})	k'_{ads} S (s^{-1})	P	$\sigma_{\bar{x}}$
8	0.96	0.48	33.3%	0.56%
8.11	0.941	0.727	12.8%	0.50%
8.31	0.96	0.85	6.1%	0.38%
8.46	0.67	0.77	-6.9%	0.68%
8.56	0.718	0.963	-14.6%	0.31%
9	1.36	1.55	-6.5%	0.30%
10	1.07	1.2	-5.7%	0.19%
11	1.01	1.05	-1.9%	0.37%
12	0.656	0.665	-0.7%	0.19%

Table A.3 Summary of 1 μg/mL L-cysteine methyl ester adsorption rate constant and polarization at different pH

pH	k'_{ads} N (s^{-1})	k'_{ads} S (s^{-1})	P	$\sigma_{\bar{x}}$
6.6	1.61	2.2	-15.5%	0.43%
6.8	1.9	1.86	1.1%	0.62%
7	1.1	0.97	6.4%	0.80%
8	1.07	0.93	6.9%	0.58%
10	0.53	0.53	0%	0.37%

Appendix B

Appendix B.1 Adsorption Isotherm

Cyclic voltammetry and QCM measurements were used to build the data for the adsorption isotherms. The data were collected by scanning from -0.4 V to - 1.1 V versus saturated Ag|AgCl at a scan rate = 25 mV/s. Unless specified all measurements were made in a pH 8 phosphate buffer solution. The frequency change from the 30th cycle, corresponding to the oxidative adsorption of cysteine on a gold substrate, was converted to a change in mass (Δm) according to the Sauerbrey equation by a factor of - 1.4 ng / Hz. The large number of cycles was needed to allow the instrument to reach equilibrium and give consistent results. Next, the mass change (Δm) or concentration/Δm was plotted versus concentration and fit to a Langmuir – Freundlich isotherm model.

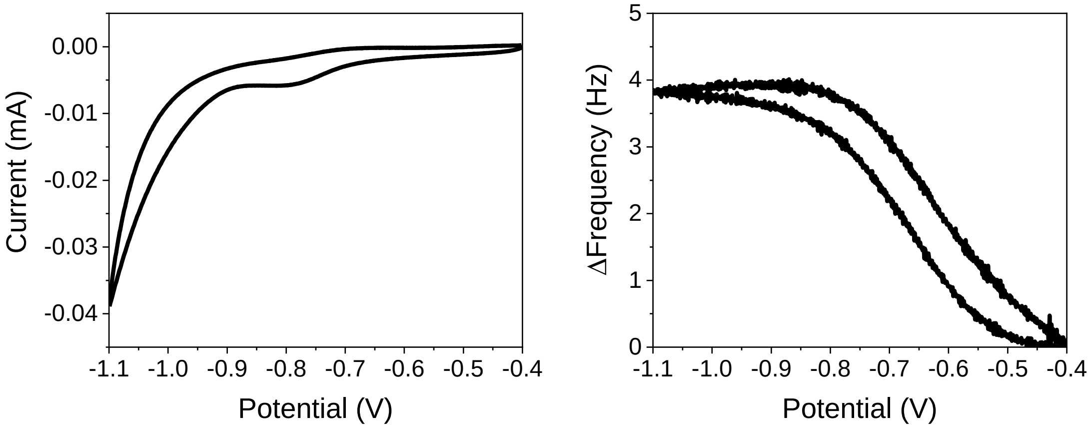

Figure B.1 The adsorption rate k'_{ads} is plotted as a function of the solution concentration for D-cysteine (left) and L-cysteine (right) under North magnetic field (red) and South magnetic field (red). The error bars show the standard deviation of the mean of the effective rate.

Appendix B.2 Linearization derivation of isotherm

Assuming that the adsorption is a reversible chemical reaction, the general form of adsorption isotherm can be expressed in a linear form:

$$\frac{c_{cys}}{\Delta m} = c_{cys} \cdot \frac{1}{\Delta m_{max}} + \frac{1}{K_{ads} \cdot \Delta m_{max}}$$

Thus, the maximum adsorption amount and the adsorption equilibrium constant K_{ads} can be calculated by the slope and intercept value of the linear plot. From the K_{ads}, the Gibbs free energy of the adsorption can be calculated by:

$$K_{ads} = \frac{1}{c_{solvent}} \cdot \exp\left(\frac{-\Delta_{ads}G}{RT}\right)$$

where $c_{solvent}$ is the concentration of the solvent, which is usually close to the concentration of pure solvent for low concentration solutions.

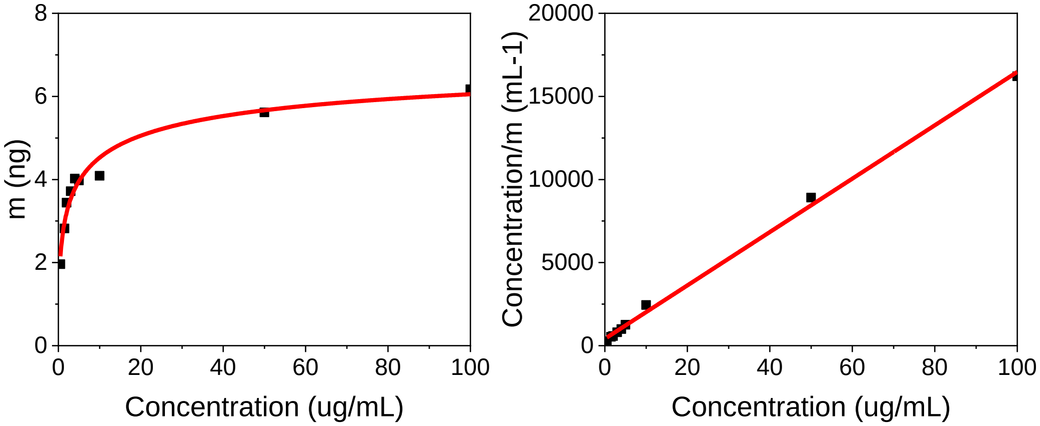

Figure B.2 The left panel shows an adsorption isotherm of D-cysteine using the change in mass determined from the cyclic voltammetry measurements at different cysteine concentrations. The red line is a Langmuir isotherm fit to the data. Right panel shows a linearized Langmuir isotherm plot of the same data in left panel.

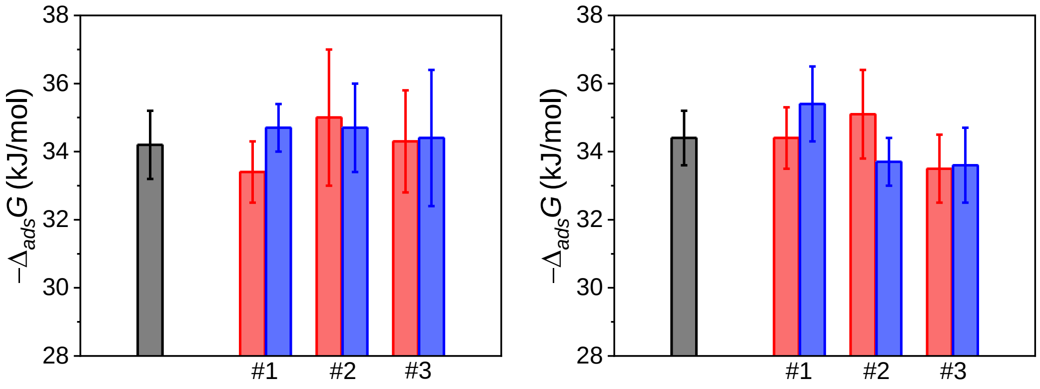

Figure B.3 Histogram of the calculated Δ_{ads}G of D-cysteine (left) and L-cysteine (right) in D_2O at pH* 8.5 for different EQCM electrodes (1−3) under north (red) and south (blue) applied magnetic fields. Studies without a magnetic field on an Au electrode are colored black. The error bars are associated with the error in the linearized isotherm fit.

Appendix B.3 Kinetic model derivation

Assuming a simple Langmuir model, the desorption rate can be written as

$$r_{des} = -\frac{d\theta}{dt} = k_{des} \cdot \theta \quad \text{or} \quad \theta(t) = \theta_{t=0} \cdot \exp\left(-k_{des} \cdot t\right)$$

where θ is the concentration of adsorbed cysteine on the surface (filled surface sites or coverage) and k_{des} is the desorption rate constant. Thus, the rate constant extracted from the exponential fits for the desorption data correspond to k_{des}. For the case of adsorption, we can write the rate as

$$r_{ads} = \frac{d\theta}{dt} = k_{ads} \cdot c_{cys} \cdot (1 - \theta) = k'_{ads} \cdot (1 - \theta)$$

where c_{cys} is the concentration of cysteine in solution, k_{ads} is the adsorption rate constant, and k'_{ads} is the effective adsorption rate constant.

To quantify the rates for the desorption and adsorption processes, the time responses of the QCM frequency were fit to an exponential growth equation $y = A \cdot e^{t/\tau_1} + y_0$ for desorption and an exponential decay equation $y = A \cdot e^{-t/\tau_2} + y_0$ for adsorption, where A, y_0, and τ_1 and τ_2 were adjusted for a best fit to the data. Then the desorption rate constant was calculated as $k_{des} = \frac{1}{|\tau_1|}$, and the effective adsorption rate constant as $k'_{ads} = \frac{1}{|\tau_2|}$.

Appendix B.4 Polarization in adsorption rate constant

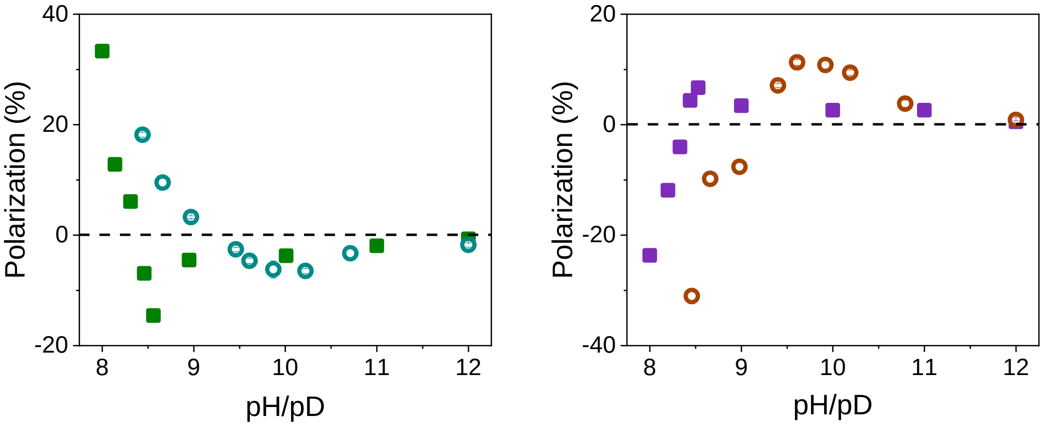

Figure B.4 Polarization in adsorption rate constant at different pK values (pH for H_2O and pD for D_2O) of solution. L-cysteine (left panel) in H_2O (green square) and D_2O (blue circle). D-cysteine (right panel) in H_2O (purple square) and D_2O (brown circle).

Appendix B.5 Abs and CD spectra of cysteine and N-acetyl cysteine methyl ester

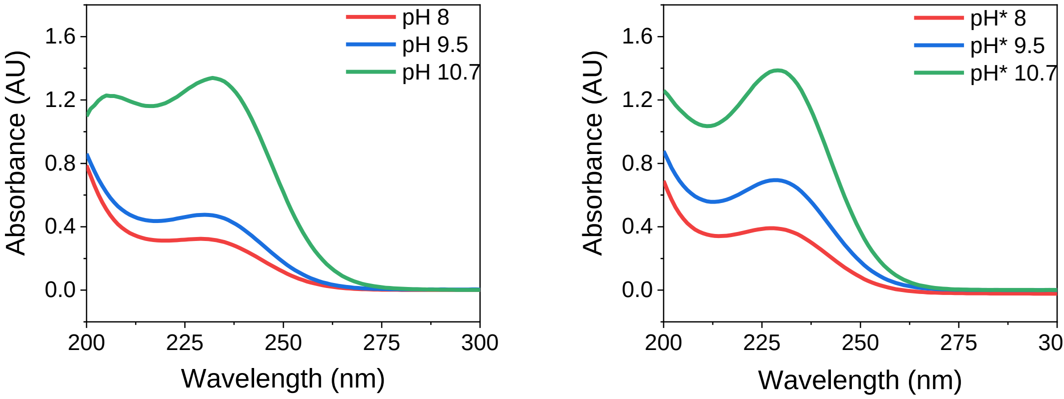

Figure B.5 Absorbance spectra of 0.4 mM L-cysteine in H_2O (left) and D_2O (right) at different pK values.

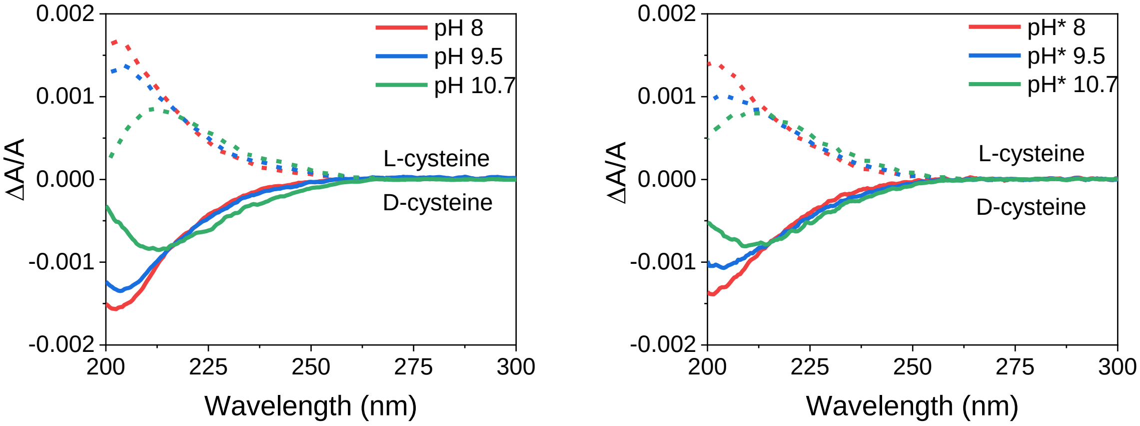

Figure B.6 CD spectra of 0.4 mM L-cysteine (dashed line) and D-cysteine (solid line) in H_2O (left) and D_2O (right) at different pKa values. CD intensities are rescaled based on the absorbance at 200 nm.

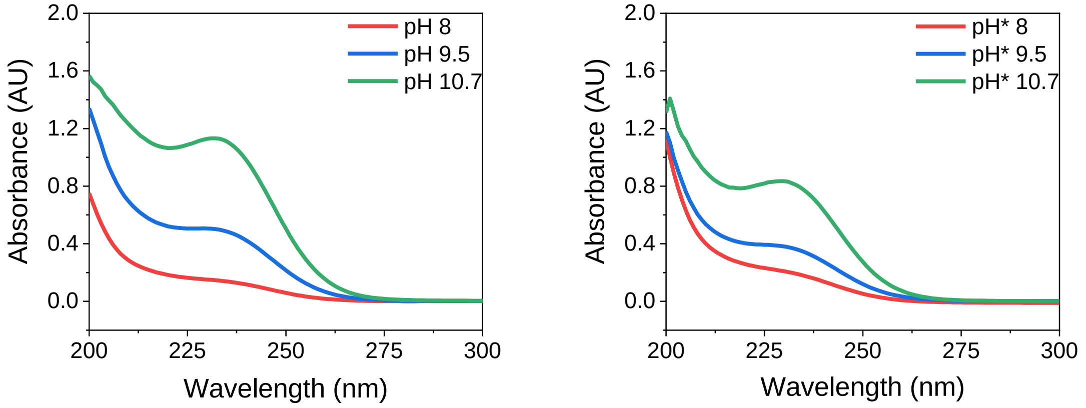

Figure B.7 Absorbance spectra of 0.2 mM N-acetyl cysteine methyl ester in H_2O (left) and D_2O (right) at different pK values.

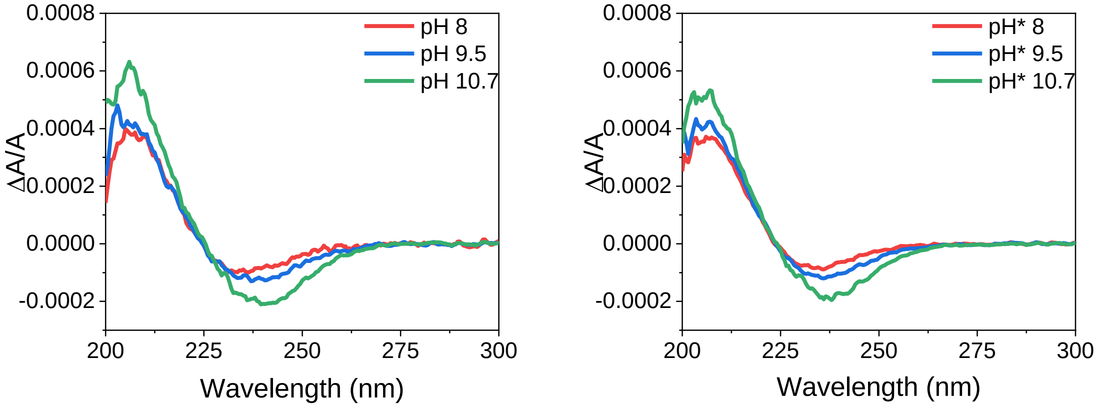

Figure B.8 CD spectra of 0.2 mM N-acetyl cysteine methyl ester in H_2O (left) and D_2O (right) at different pK values. CD intensities are rescaled based on the absorbance at 200 nm.

Appendix B.6 Underpotential deposition (UPD) of lead

Underpotential deposition (UPD) of lead on our substrates were performed using a 5 mM Pb(ClO4)2, 10 mM of HClO4 and 0.1 M of KClO4 solution. Cyclic voltammograms (left panel) from 0.24 V to -0.45 V versus saturated Ag|AgCl in tandem with the QCM show that the lead adsorbs and gives rise to a cathodic peak at -0.31 V and an anodic peak at around -0.2 V. These redox potentials match well with the reported redox peaks for lead UPD on a Au(111) surface.1 While the redox peaks using our electrode are broader, associated with other crystalline facets, the most intense, and hence largest contribution, arises from Au (111).

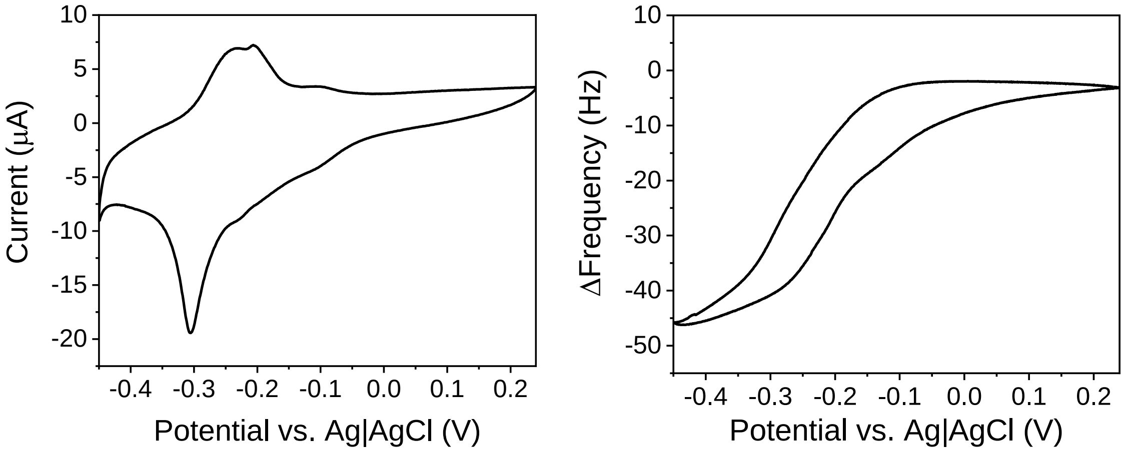

Figure B.9 The voltametric (left) and frequency (right) response of the QCM during the underpotential deposition of Pb.

Appendix B.7 The possible adsorption configurations of cysteine and N-acetyl cysteine methyl ester at other directions

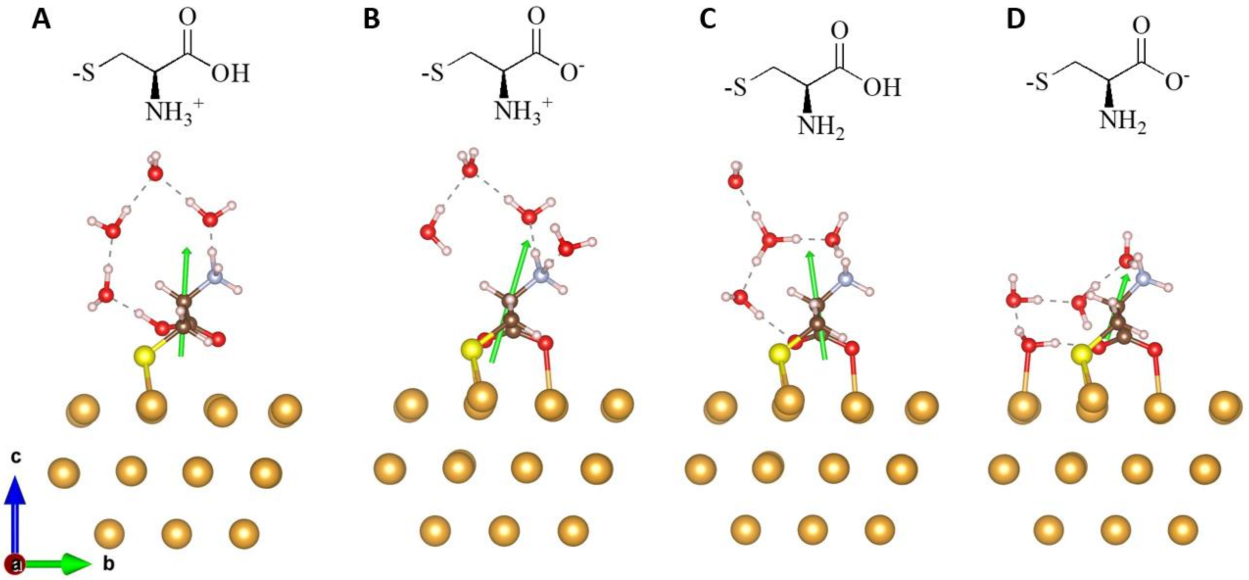

Figure B.10 The possible adsorption configurations and the dipole moments (green arrow) of L-cysteine in H_2O on Au based on DFT calculation. The red, gray, brown and white spheres indicate the oxygen atoms, nitrogen atoms, carbon atoms, and hydrogen atoms.

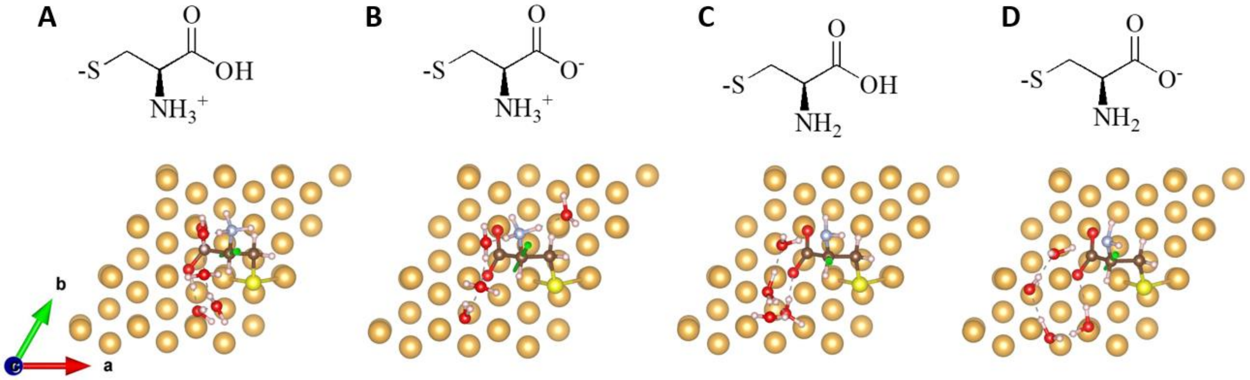

Figure B.11 The possible adsorption configurations and the dipole moments (green arrow) of L-cysteine in H_2O on Au based on DFT calculation. The red, gray, brown and white spheres indicate the oxygen atoms, nitrogen atoms, carbon atoms, and hydrogen atoms.

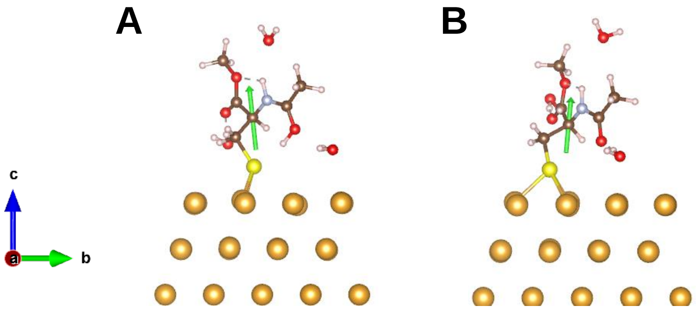

Figure B.12 The possible adsorption configurations and the dipole moments (green arrow) of N-acetyl-L-cysteine methyl ester in H_2O on Au based on DFT calculation. The red, gray, brown and white spheres indicate the oxygen atoms, nitrogen atoms, carbon atoms, and hydrogen atoms.

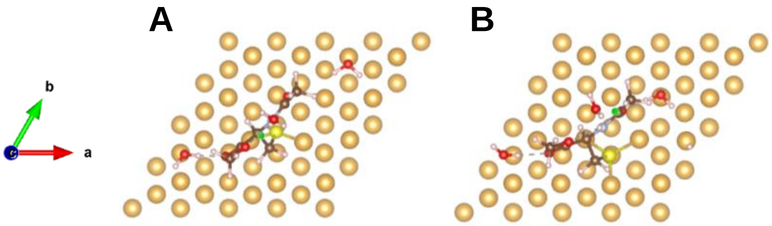

Figure B.13 The possible adsorption configurations and the dipole moments (green arrow) of N-acetyl-L-cysteine methyl ester in H_2O on Au based on DFT calculation. The red, gray, brown and white spheres indicate the oxygen atoms, nitrogen atoms, carbon atoms, and hydrogen atoms.

Appendix B.8 The choice of cysteine orientation

We explored a large number of possible geometries for cysteine adsorbed on the Au surface. We began by investigating which functional groups of cysteine are most important in adsorption. We explored geometries with (A) $-COO^-$, (B) $-S^-$, (C) -SH and $-COO^-$, and (D) -SH, -COOH, and $-NH_2$ interacting with the Au surfaces. Besides the default simulation settings mentioned in the manuscript, a polarizable continuum model (PCM) with the dielectric constant of 80 is also applied by the Environ addon of Quantum Espresso. The geometries before and after the optimizations are shown in Figure B14 and the energies for the optimized geometries are listed below the corresponding geometries.

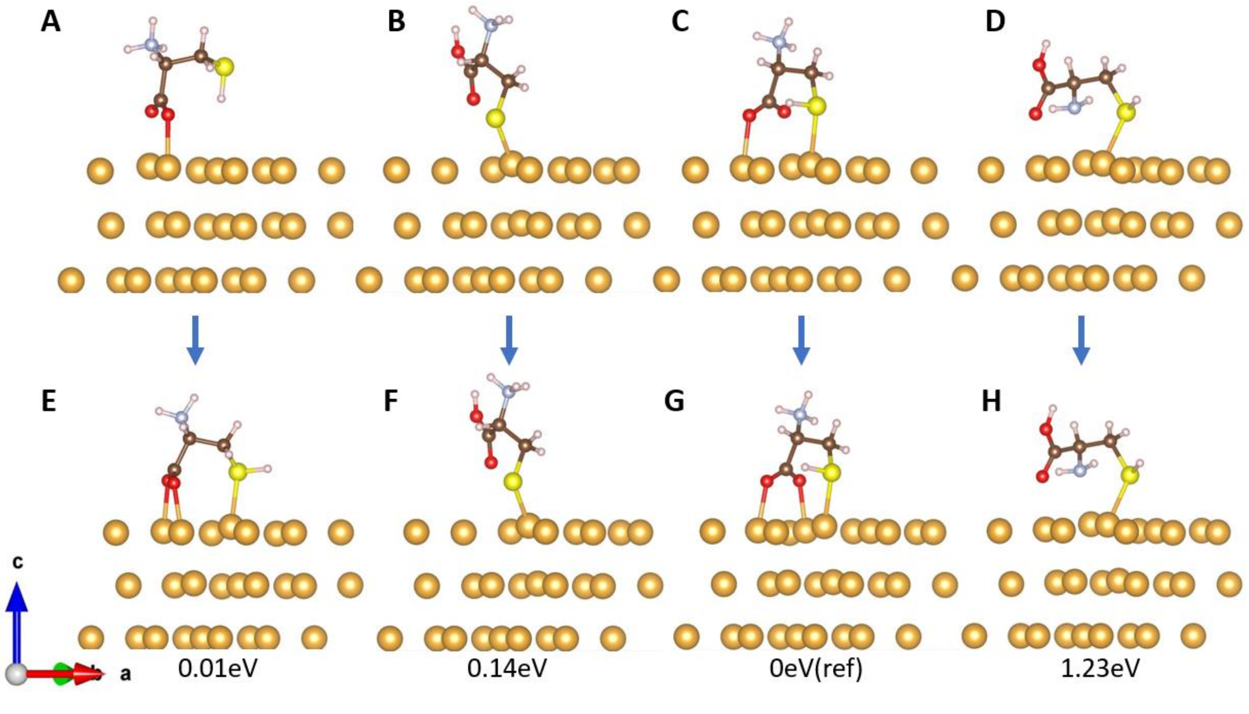

Figure B.14 The possible adsorption configurations and the dipole moments (green arrow) of N-acetyl-L-cysteine methyl ester in H_2O on Au based on DFT calculation. The red, gray, brown and white spheres indicate the oxygen atoms, nitrogen atoms, carbon atoms, and hydrogen atoms.

Appendix B.9 The choice of number of explicit water molecules

To investigate whether the local solvation structure is important or not, explicit water molecules have been added to the simulation cell in the presence of PCM. The structures of adding 3,4, and 5 water molecules before and after the optimization are shown in Figure B15. The adsorption energy of added water molecule is calculated as the reaction energy of the following reaction:

$$\mathrm{S}_i(\mathrm{PCM}) + \mathrm{H_2O}(\mathrm{PCM}) \rightarrow \ \mathrm{S}_j(\mathrm{PCM})$$

where structure S_j has one extra explicit water molecule than S_i. The adsorption energy of adding the 3rd, 4th, and 5th water molecule is plotted in Figure S16 (the data point for the 3rd water molecule is in fact the averaged adsorption energy of all the first three water molecules). Note that adding the 4th water molecule causes a significant energy drop compared to adding 3 and the 5th water molecule. Also, from Figure B15 B and C, we find that a local water-ring structure forms when the 4th water molecule is added, and the structure is effectively unchanged when the 5th water molecule is added. Consequently, we choose to add 4 explicit water molecules.

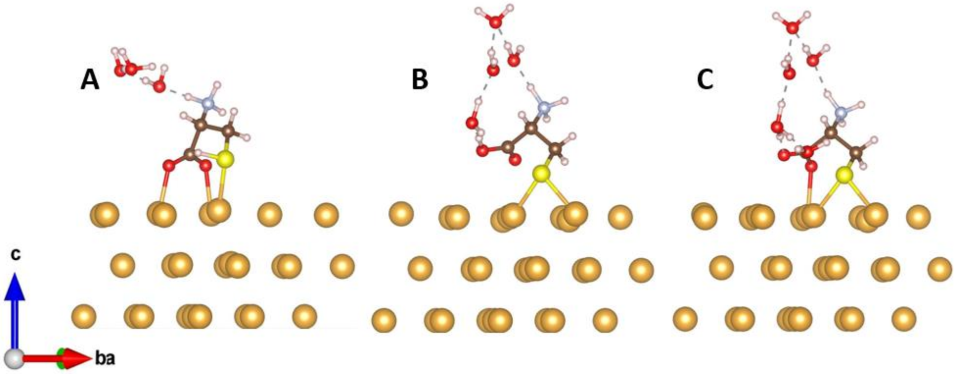

Figure B.15 Optimized geometries of cysteine with explicit water molecules. A, B, and C: cysteine with 3, 4, and 5 explicit water molecules, respectively. Note that with 4 explicit water molecules, a local ring-shape structure forms. This structure effectively unchanges when the 5th water molecule is added.

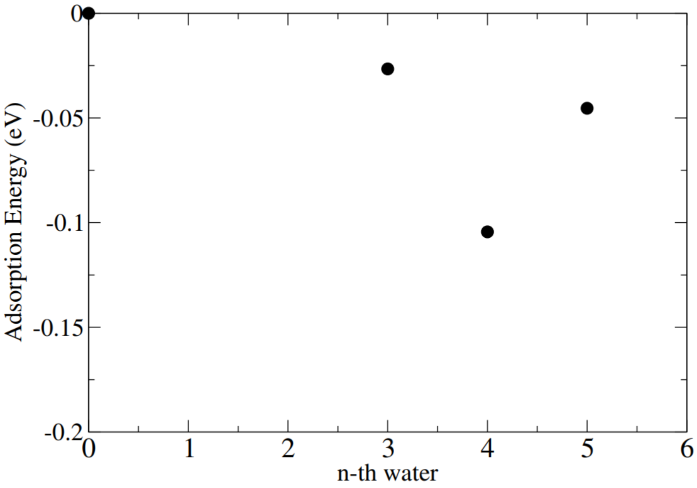

Figure B.16 Adsorption energy of adding another explicit water molecule. The energy of the 3rd water molecule represents the average adsorption energy of the first three water molecules.

Appendix B.10 Geometries and energies of sampled structures

The sampled geometries of cysteine with 4 explicit water molecules after the optimization are shown in Figure B17, and the relative energy of each optimized geometry is listed below the corresponding structure.

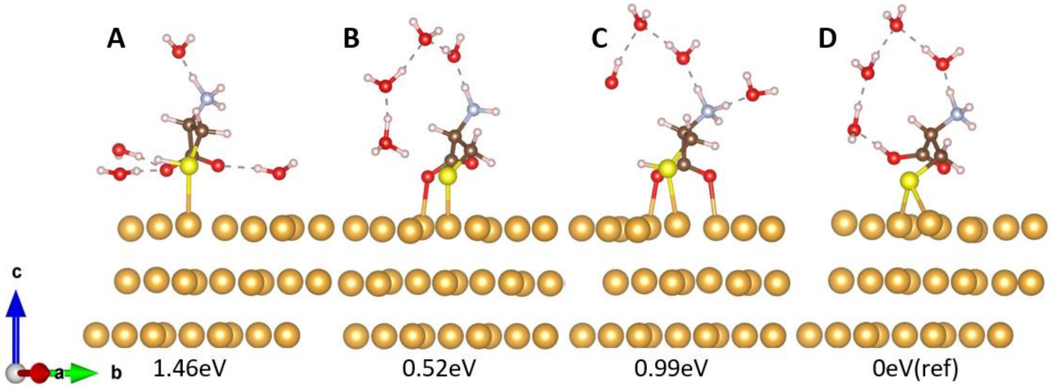

Figure B.17 Several optimized geometries of cysteine with 4 explicit water molecules. Structure D is the most stable structure.

The optimized geometries and relative energies of the sampled deprotonated cysteine (-1 H^+) with 4 water molecules are shown in Figure B18. Among all sampled structures in Figure S18, structure A is the most stable one which has the -NH_3^+ group. For structures with the -NH_2 group instead, structure F is the most stable one.

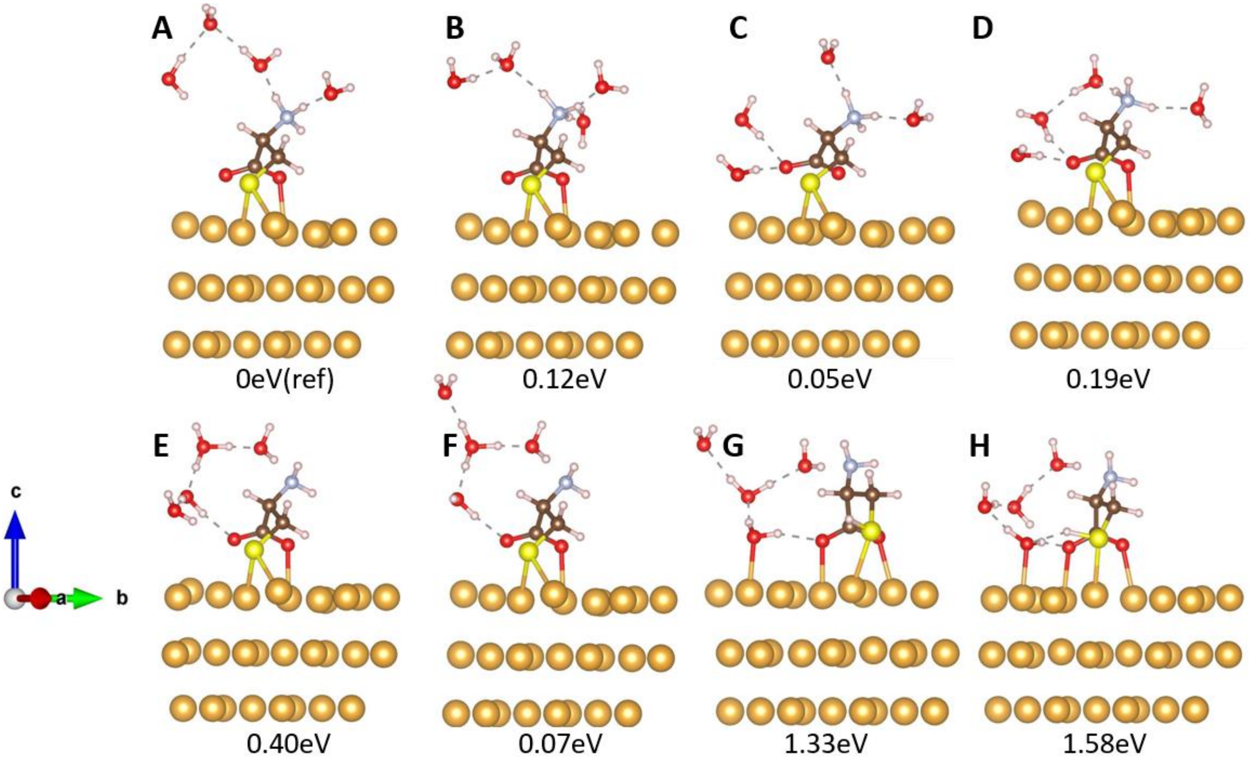

Figure B.18 Optimized geometries of deprotonated cysteine (-1 H^+) with 4 explicit water molecules. A, B, C, and D have an -NH_3^+ group while E, F, G, and H have an -NH_2 group. The most stable structure among all the sampled geometries is A. In terms of structures that have the -NH_2 group, the most stable structure is F. Note that the proton is delocalized in the water ring in structure F.

The optimized geometries and relative energies of the sampled deprotonated cysteine (-2 H^+) with 4 water molecules are shown in Figure B19.

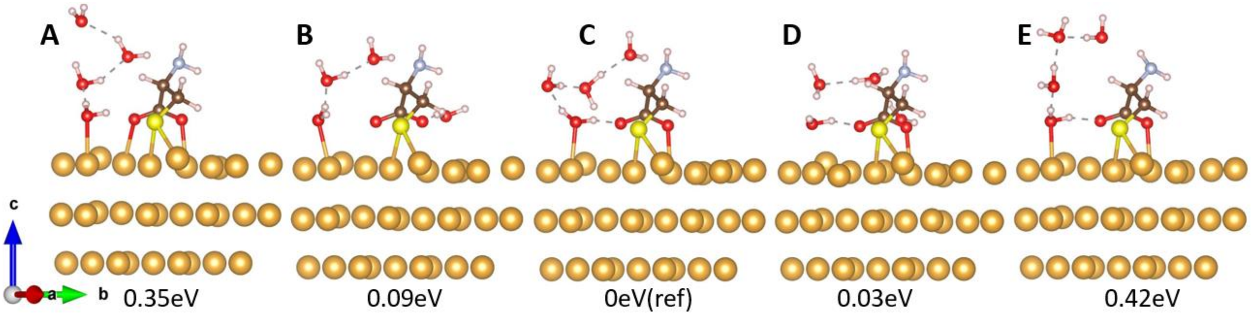

Figure B.19 Optimized geometries of deprotonated cysteine (-2 H^+) with 4 explicit water molecules. Structure C is the most stable.

Appendix C

Appendix C.1 Stability of NAC assemblies

Linear sweep voltammetry measurements were performed to determine the potential required for desorption and re-adsorption of LeuME enantiomers from the NAC coated Ni/Au films. First, the stability of L-NAC and D-NAC coated Ni/Au film was studied. When scanning negatively from 0 V to -0.8V, a cathodic desorption peak occurs at around -0.65 V for both L-NAC and D-NAC (Figure S1A), and the mass begins to decrease from -0.45 V (Figure S1B). These results indicate that the L-NAC and D-NAC are stable if the applied potential is more positive than -0.4 V.

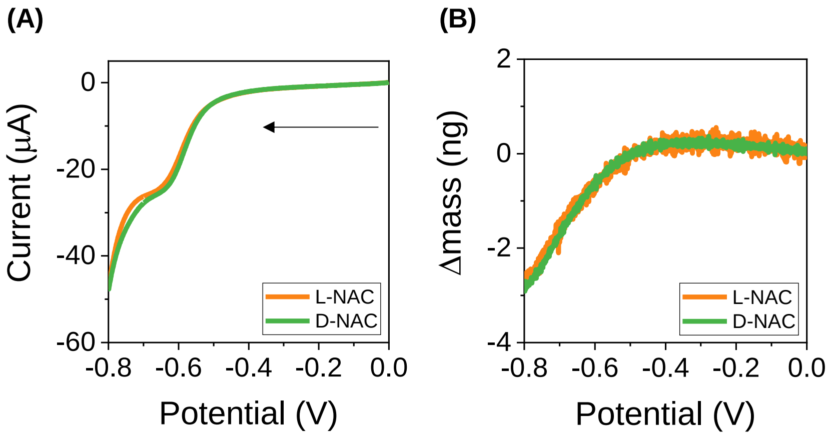

Figure C. 1 (A) Linear sweep voltammograms and (B) corresponding mass changes of L-NAC (Orange) and D-NAC (Green) coated Ni/Au film in 0.1 M phosphate buffer. The Black arrow denotes the sweep direction.

Appendix C.2 Determination of Adsorption and Desorption Behavior of Leu ME on NAC

To determine the adsorption of LeuME enantiomers onto NAC coated Ni/Au films the potential was scanned from 0 V to -0.8V and the change in mass studied. As the potential was swept, a mass increase process followed by a mass decrease process was observed (Figure C.2B & E). This behavior is attributed to cathodic adsorption of LeuME enantiomers onto the L-NAC SAM surface (0 V to around -0.4V) that is followed by a complete cathodic desorption of L-NAC with LeuME (-0.4V to -0.8V). Interestingly, more L-LeuME adsorbs onto the surface under a North magnetic field (red) than a South magnetic field (blue); See Figure C.2C. Conversely the opposite behavior manifests for D-LeuME (Figure C.2F). Also, the desorption peak of L-NAC with LeuME exhibits a dependence on the enantiomeric form of Leu ME and the magnetic field direction; L-LeuME on L-NAC shows a more negative desorption peak under a North magnetic field, indicating a stronger binding onto Ni/Au film, whereas D-Leu ME on L-NAC shows the opposite dependence on magnetic field. These results indicate that the charge delocalization across the NAC-LeuME composite is spin-dependent and enantiospecific. Figure C.3 shows complimentary measurements on D-NAC SAMs, and the result is opposite to that on L-NAC SAMs.

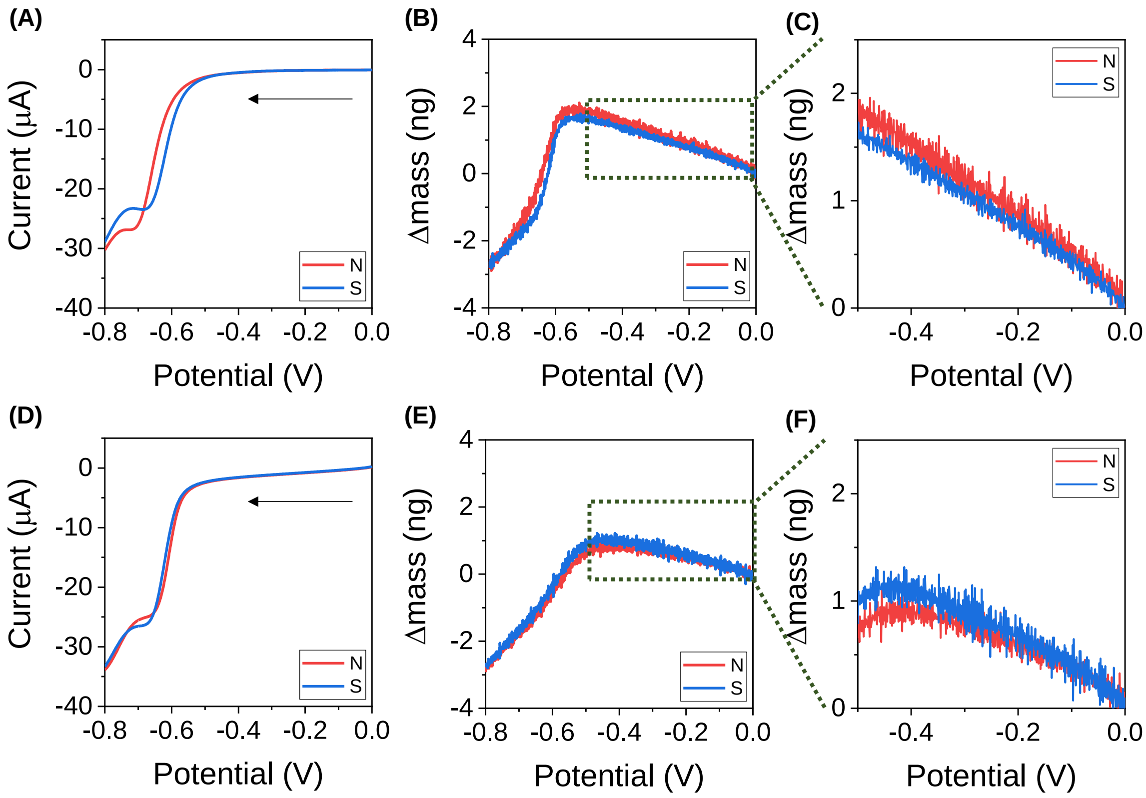

Figure C. 2 Panel (A) shows linear sweep voltammograms, and panel (B) the corresponding mass change, of an L-NAC coated Ni/Au film in 0.1 M phosphate buffer with 150 μM L-Leu ME with a North (red) and South (blue) applied magnetic field. Panel (C) shows a zoomed in view of the mass change of (B). Panel (D) shows linear sweep voltammograms, and panel (E) shows the corresponding mass change, of an L-NAC coated Ni/Au film in 0.1 M phosphate buffer with 150 μM D-LeuME. Panel (F) shows a zoomed in view of the mass change of (E). The black arrow denotes the voltage sweep direction.

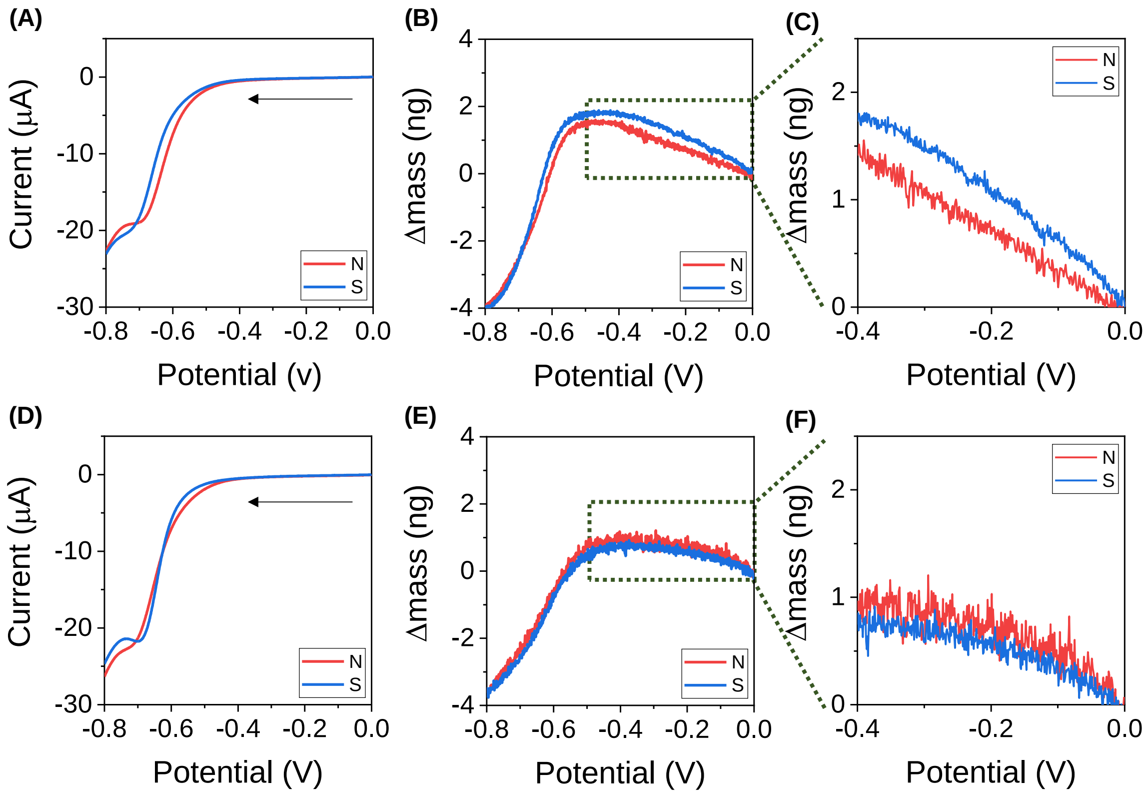

Figure C. 3 Panel (A) shows linear sweep voltammograms, and panel (B) shows the corresponding mass change, of a D-NAC coated Ni/Au film in 0.1 M phosphate buffer with 150 µM L-Leu ME, with a North (red) and a South (blue) applied magnetic field. Panel (C) shows a zoomed in view of the mass change in panel (B). Panel (D) shows linear sweep voltammograms, and panel (E) shows the corresponding mass change, of D-NAC coated Ni/Au film in 0.1 M phosphate buffer with 150 µM D-Leu ME. Panel (F) shows a zoomed in view of the mass change in Panel (E). The black arrows denote the voltage sweep direction.

Appendix C.3 Chronoamperometry Measurements and Data Analysis

Figure C.4A shows representative data for the chronoamperometry measurements; the top panel shows the potential sequence and the bottom panel shows the corresponding frequency response. To extrapolate the rate constant data from the frequency response, the following calculations were performed. First, the adsorption process was assumed to follow a simple Langmuir model and thus,the adsorption rate can be written as Eq. (1)

$$r_{ads} = \frac{d\theta}{dt} = k_{ads} \cdot c_{Leu\,ME} \cdot (1 - \theta) = k'_{\ ads} \cdot (1 - \theta) \qquad \text{Eq. (1)}$$

where $c_{Leu\,ME}$ is the concentration of LeuME in solution, θ is the concentration of adsorbed molecule on the surface, k_{ads} is the adsorption rate constant and $k'_{\ ads}$ is the effective adsorption rate constant. To quantify the adsorption rates, the time responses of the QCM frequency were fit to an exponential decay equation $y = A \cdot e^{-t/\tau_1} + y_0$ for adsorption (Figure C.4B top panel), where A, y_0, and τ_1 were adjusted for a best fit to the data. Then the effective adsorption rate constant was calculated as $k'_{\ ads} = \frac{1}{|\tau_1|}$. A histogram with >150 $k'_{\ ads}$, determined through this method was then built and fit to a Gaussian distribution to obtain the average and standard deviation of the mean for the adsorption rate constant (Figure S4C top panel).

The desorption rate can be written as Eq. (2)

$$r_{des} = -\frac{d\theta}{dt} = k_{des} \cdot \theta \qquad \text{Eq. (2)}$$

where θ is the concentration of adsorbed molecule on the surface and k_{des} is the desorption rate constant. The time responses of the QCM frequency were fit to an exponential growth equation $y = A \cdot e^{t/\tau_2} + y_0$ for desorption (Figure C.4B bottom panel), where A, y_0, and τ_2 were adjusted for a best fit to the data. Then, the desorption rate constant was calculated as $k_{des} = \frac{1}{|\tau_2|}$. A histogram with >150 k_{des}, determined through this method was then built and again fit to a Gaussian distribution to obtain the average and standard deviation of the mean for the desorption rate constant (Figure C.4C bottom panel).

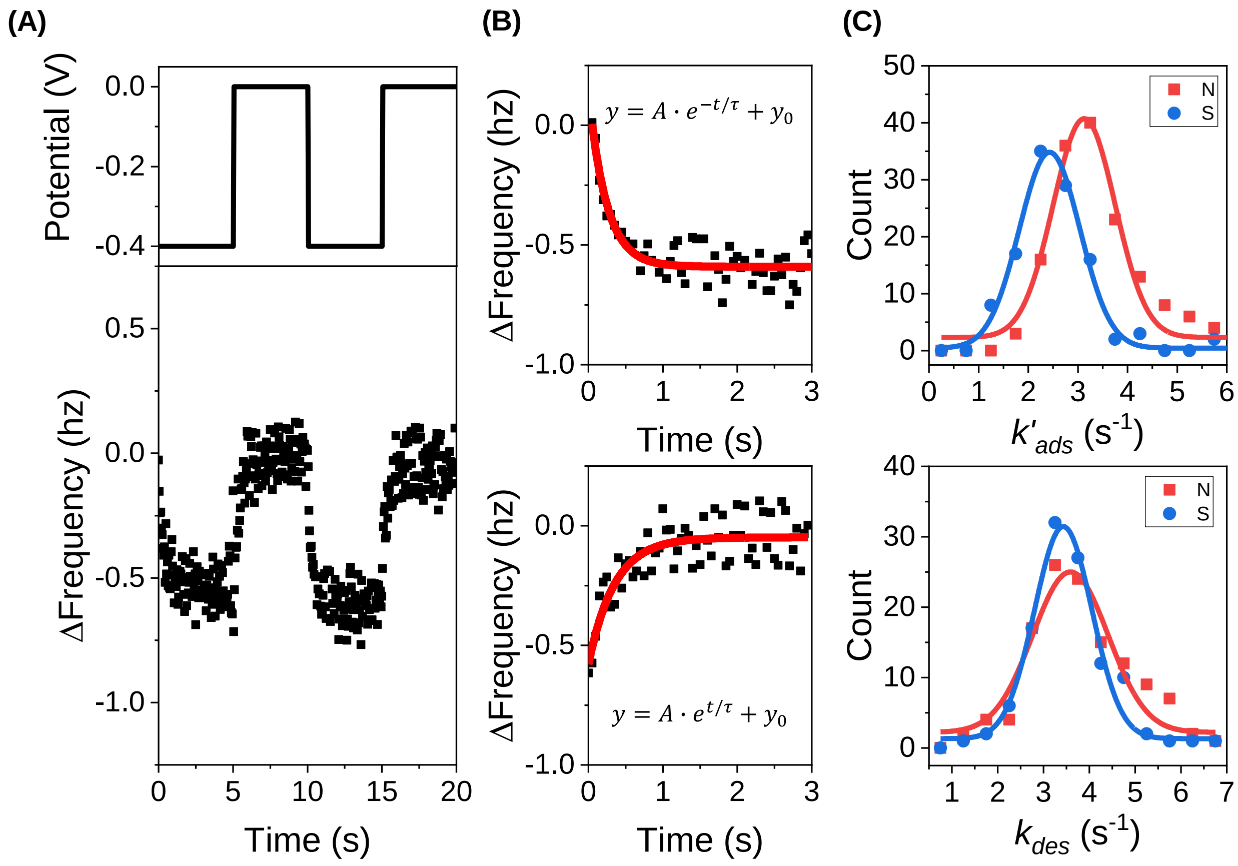

Figure C. 4 (A) Chronoamperometry data for a 150 μM solution of L-Leu ME. The applied potential sequence (top) and the corresponding frequency response (bottom) are recorded. (B) An expanded plot of the adsorption (top) and desorption (bottom) fits by an exponential decay or growth (red line) for determining the rate constant. (C) The histograms on the right comprise >150 fits of the adsorption (top) and desorption (bottom) processes under a north magnetic field (red) and a south magnetic field (blue). A best fit of the data using a Gaussian distribution is shown as a solid curve.

To quantify the mass change during the adsorption (desorption) process, eighty QCM frequency responses were selected at random and the average change in frequency during the 5s adsorption (desorption) process was quantified. A frequency shift of -1.0 Hz corresponds to a mass change of 1.4 ng based on the Sauerbrey equation and characteristics of our EQCM set-up. To determine the mass change, the data were fit to an exponential growth equation, $y = A \cdot e^{t/\tau_1} + y_0$ (Figure C.4), in which A, y_0, and τ_1 and were adjusted for a best fit to the data, allowing the coverage after 5s to be calculated. Figure C.5 (A) –(C) replots the average mass change, reported in Figure 4. 3 (A)-(C) in the main text, for L-LeuME adsorption on L-NAC, MPA, and D-NAC, and the complimentary measurements on the same substrates for D-LeuME are plotted in Figure C.5(D)-(F).

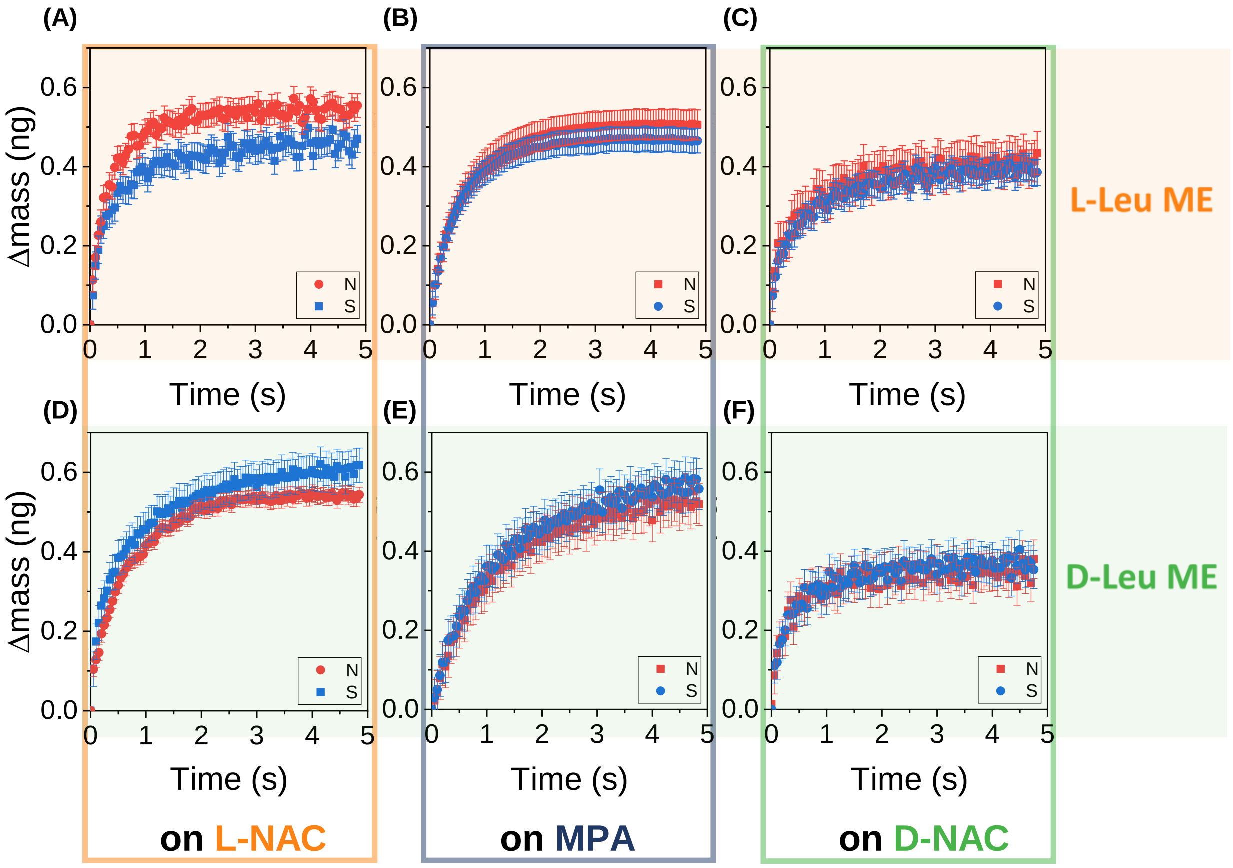

Figure C. 5 The average mass change during adsorption of L-Leu ME onto Ni/Au film coated with (A) L-NAC, (B) MPA, and (C) D-NAC SAMs under North magnetic field (red) and South magnetic field (blue). The average mass change during adsorption of D-Leu ME onto Ni/Au film coated with (D) L-NAC, (E) MPA, (F) and D-NAC SAMs under North magnetic field (red) and South magnetic field (blue).

Figure C.6 shows histograms for the adsorption rate constants of D-Leu ME onto L-NAC (Figure C.6A), MPA (Figure C.6B), and D-NAC (Figure C.6C) coated electrodes upon application of a North (red) and South (blue) magnetic field. In all three SAM configurations the adsorption rate constant for D-Leu ME is faster when the magnetic field is oriented South rather than North.

The change in mass of D-Leu ME at 5s, after the kinetically controlled adsorption process is shown in Figure C.6D. Values for the mass change in Figure C.6D and Figure 4.3 in the main text are reported in Table C.1. Homochiral ensembles exhibited the largest average mass (L-LeuME on L-NAC, and D-LeuME on D-NAC). Heterochiral ensembles exhibited the smallest average mass (L-LeuME on D-NAC, and D-LeuME on L-NAC). Achiral SAMs were intermediate. Analogous adsorption rate constant measurements and mass changes occurring during the desorption process are shown in Figure C.7 and C.8. for L-LeuME and D-LeuME, respectively, on L-NAC, MPA, and D-NAC SAMs. A summary of the polarization in adsorption rate constant for LeuME desorption is shown in Figure C.9A and complimentary measurements on phenylalanine, Phe, for adsorption is shown in Figure C.9B.

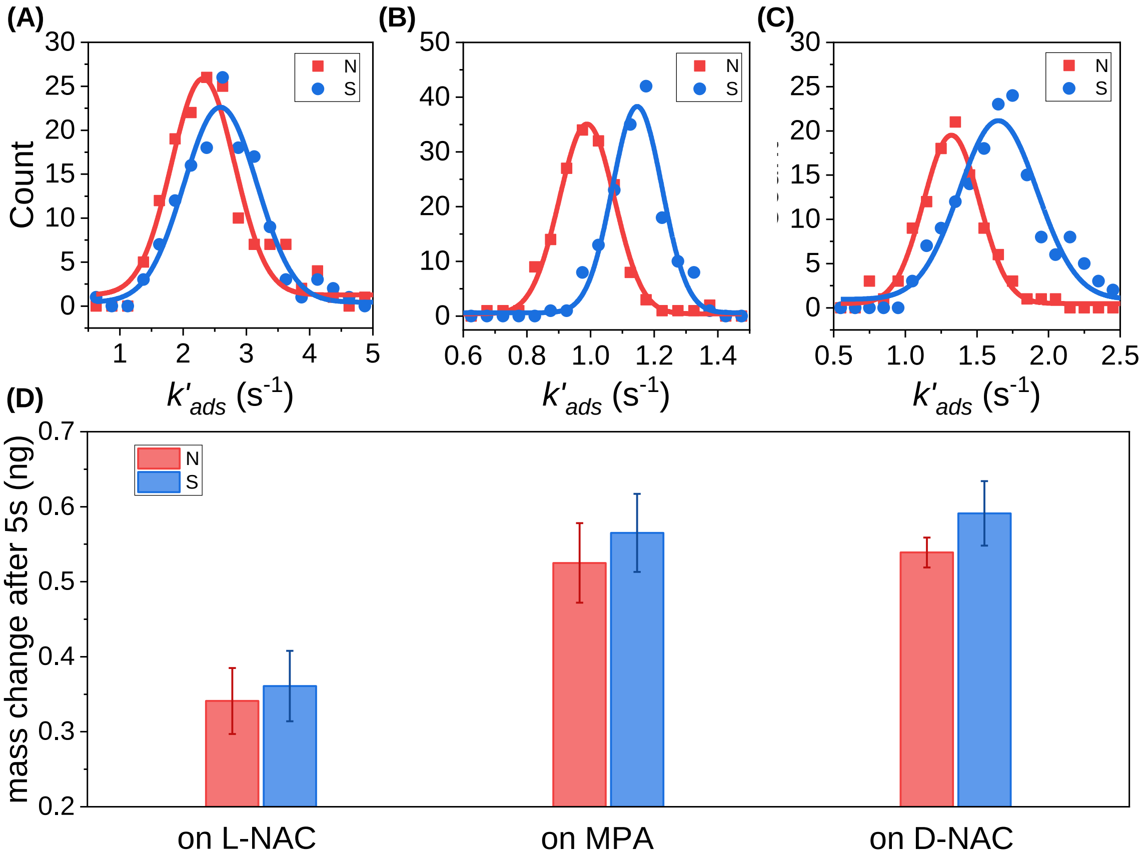

Figure C. 6 Histograms of adsorption rate constant for D-Leu ME onto Ni/Au films coated with (A) L-NAC, (B) MPA, and (C) D-NAC SAMs under North magnetic field (red) and South magnetic field (blue). Panel (D) shows the average mass change during the adsorption of D-Leu ME on to Ni/Au film coated with different SAMs under a North magnetic field (red) and a South magnetic field (blue).

Table C. 1 Total mass change (in unit of ng) for the adsorption of L-LeuME and D-LeuME onto different SAMs after 5s

	L-LeuME			D-LeuME		
	N	S	average	N	S	average
L-NAC	0.566±0.034	0.447±0.030	0.506±0.032	0.341±0.024	0.361±0.027	0.351±0.026
MPA	0.503±0.038	0.466±0.030	0.485±0.034	0.525±0.023	0.565±0.022	0.545±0.023
D-NAC	0.404±0.054	0.381±0.032	0.393±0.043	0.539±0.010	0.591±0.023	0.565±0.016

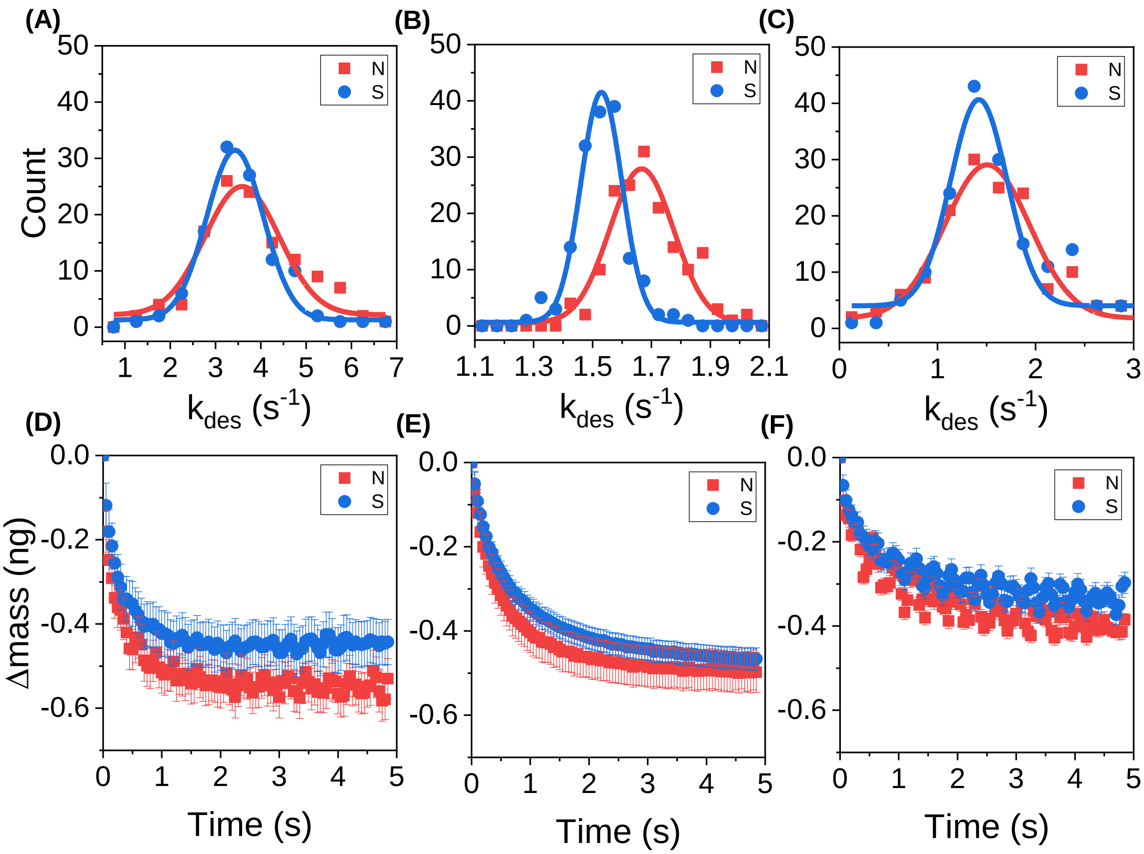

Figure C. 7 Histograms of desorption rate constants of L-LeuME from Ni/Au film coated with (A) L-NAC, (B) MPA, and (C) D-NAC SAM, and the average mass change during desorption of L-LeuME from Ni/Au films coated with (D) L-NAC, (E) MPA, and (F) D-NAC SAMs under North magnetic field (red) and South magnetic field (blue).

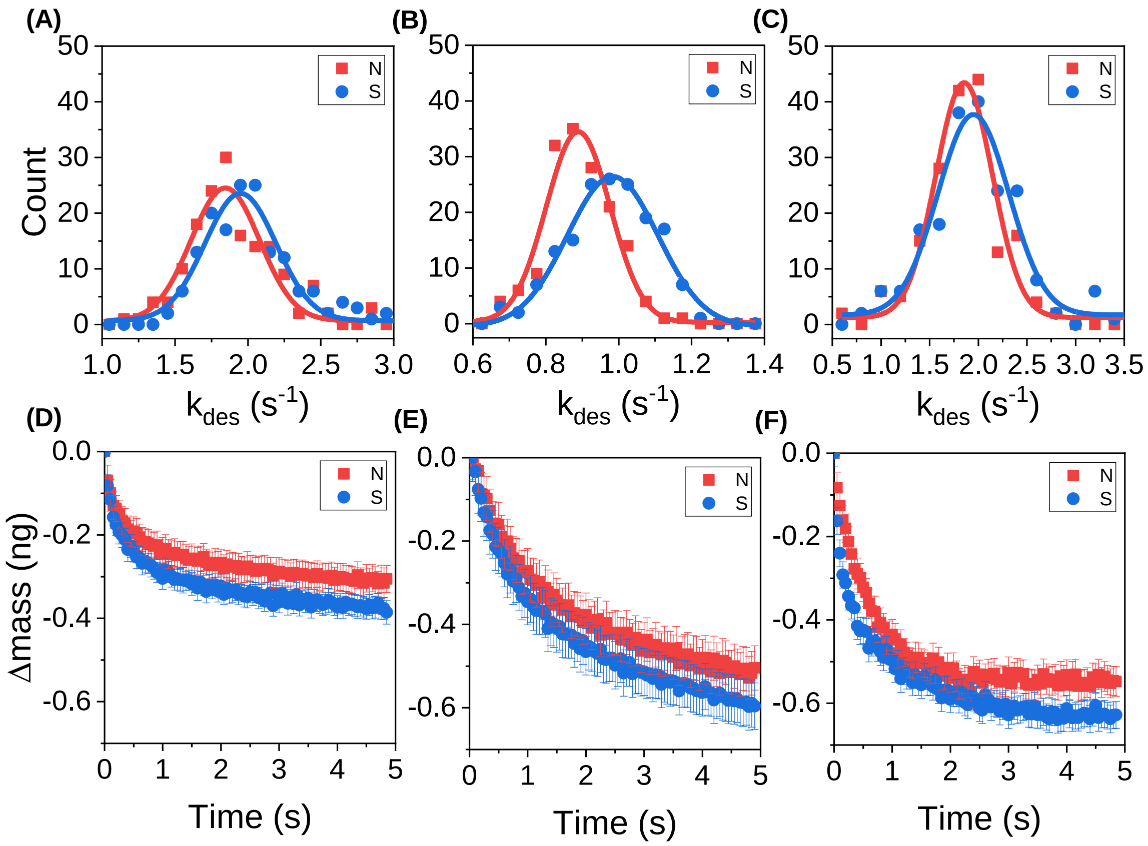

Figure C. 8 Histograms for the desorption rate constants of D-LeuME from Ni/Au film coated with (A) L-NAC, (B) MPA, and (C) D-NAC SAMs, and the average mass change during desorption of D-LeuME from Ni/Au film coated with (D) L-NAC, (E) MPA, and (F) D-NAC SAMs under North magnetic field (red) and South magnetic field (blue).

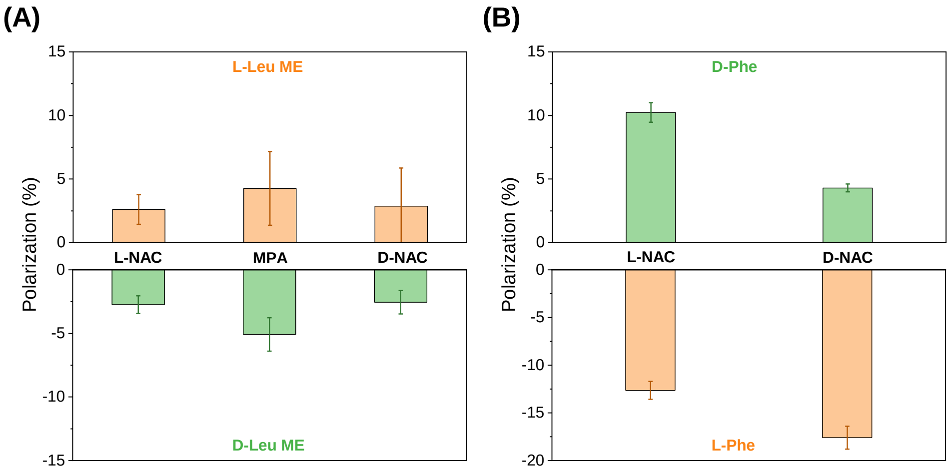

Figure C. 9 Panel (A) shows the polarization in desorption rate constant of Leu ME enantiomers on different SAMs. Panel (B) shows the polarization in adsorption rate constant of Phe enantiomers on different SAM.

Appendix C.4 Adsorption Rate Asymmetry of L-amino acids on L-NAC

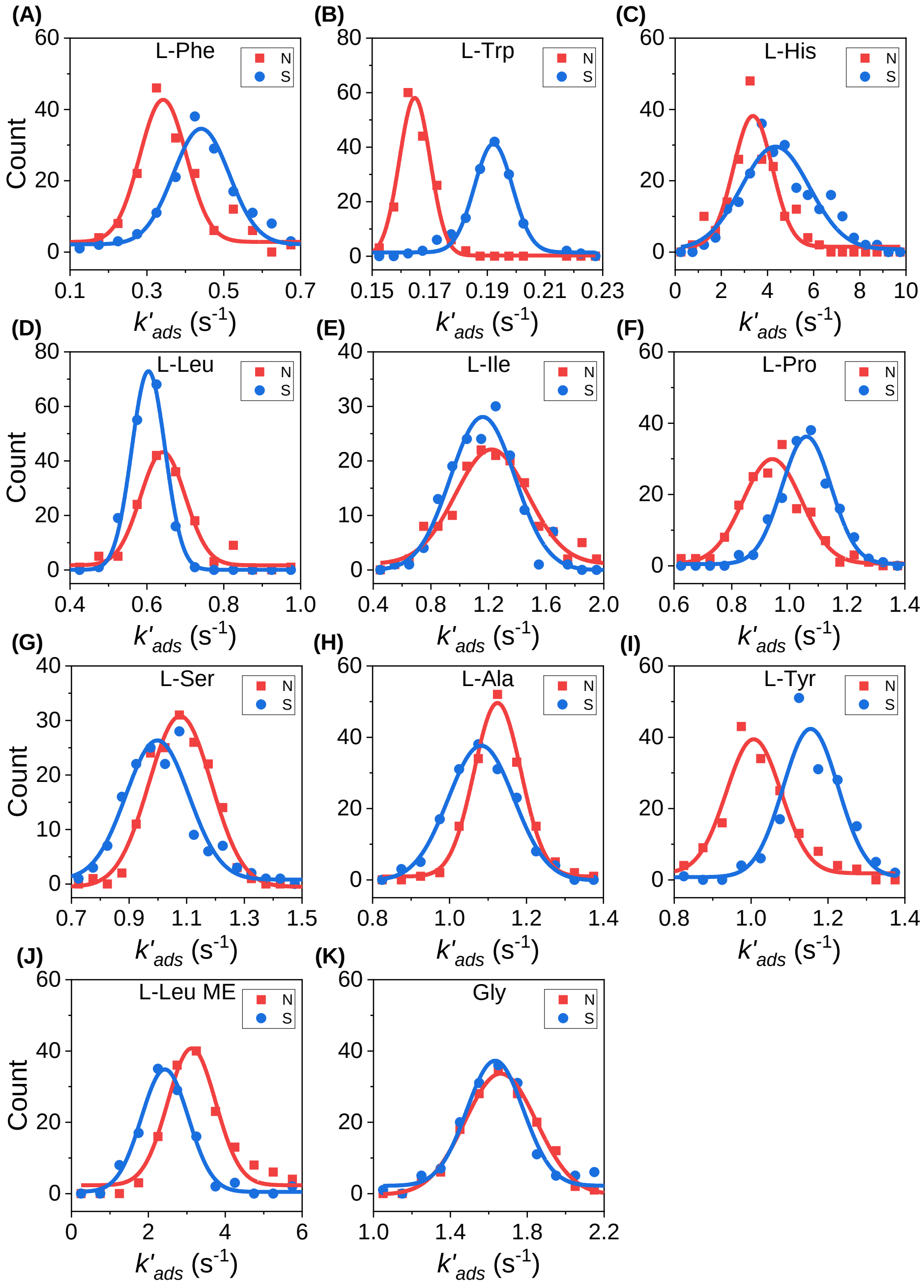

Figure C. 10 Histograms of adsorption rate constants of 150 μM (A) L-Phe, (B) L-Trp, (C) L-His, (D) L-Leu, (E) L-Ile, (F) L-Pro, (G) L-Ser, (H) L-Ala, (I) L-Tyr, (J) L-LeuME, (K) Gly onto L-NAC SAM coated Ni/Au films under North magnetic field (red) and South magnetic field (blue). A best fit of the data using a Gaussian distribution is shown as a solid line.

Appendix C.5 Control Experiments on Gold

Control experiments were performed for the adsorption of L-Leu ME and L-Phe onto L-NAC SAM coated Au films, which are not ferromagnetic, under North and South magnetic fields; See Figure C.11. The polarization in adsorption rate constant for L-Leu ME is 0.94 ± 0.64% and for L-Phe is 1.09 ± 0.58%, indicating the adsorption behavior of a chiral molecule onto a nonmagnetic substrate is the same under the North and South magnetic field. Thus, the enantiospecific adsorption is not arising from the magnetic field per se, but instead from the CISS-mediated spin dependent exchange interactions at the ferromagnetic surface.

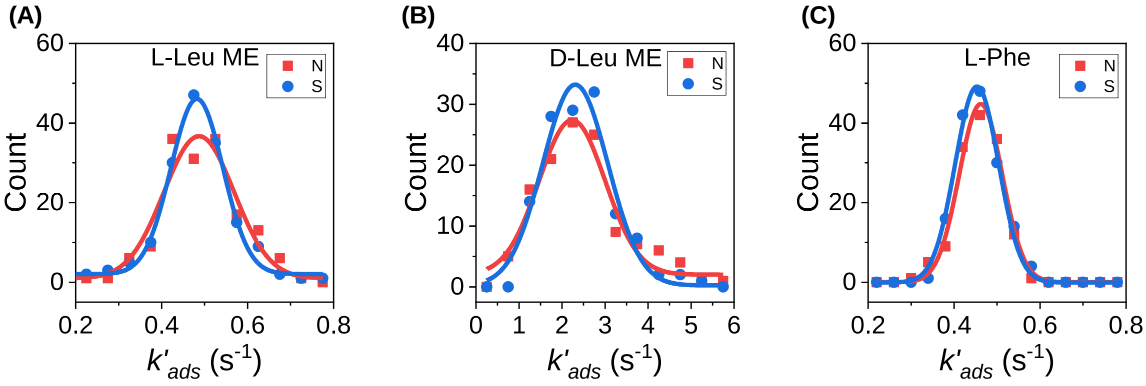

Figure C. 11 Histograms for the adsorption rate constant of 150 μM (A) L-Leu ME and (B) D-Leu ME and (C) L-Phe onto L-NAC SAM coated Au films under North magnetic field (red) and South magnetic field (blue). A best fit of the data using a Gaussian distribution is shown as a solid line.

Appendix C.6 Spectroscopic data

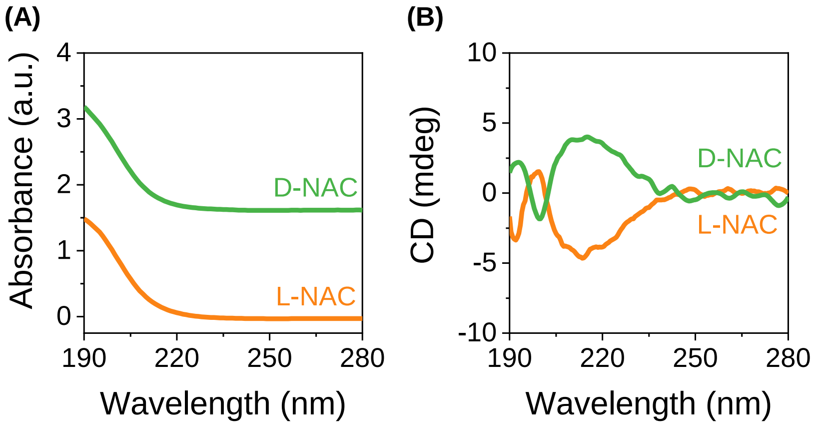

Figure C. 12 Absorbance and CD spectra of 1.5 mM L-NAC (Orange) and D-NAC (Green) in 2 mM phosphate buffer solutions at pH 9.

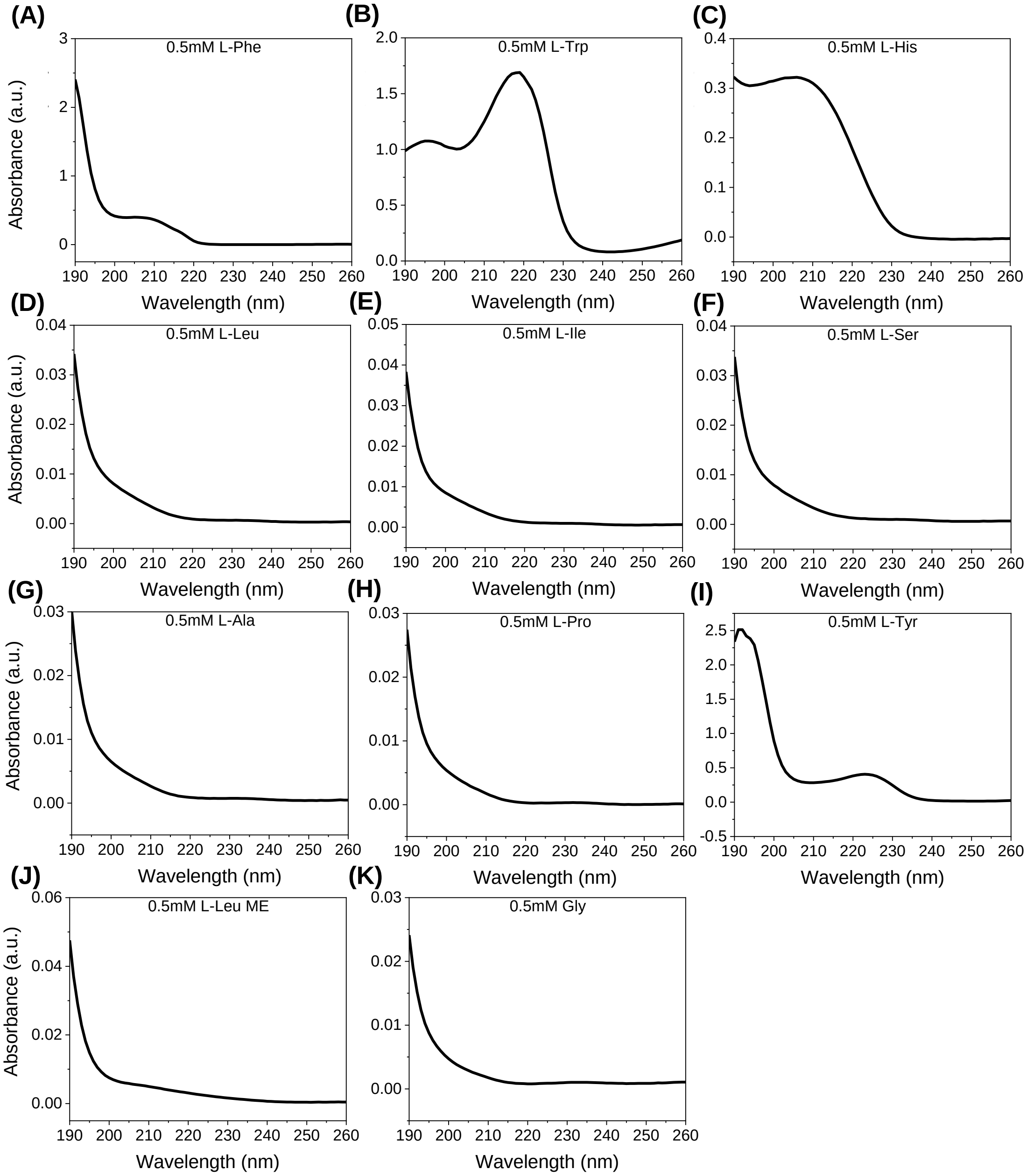

Figure C. 13 Absorbance spectra of of 0.5 mM solutions of the different amino acids studied in 2 mM phosphate buffer solution at pH 9; (A) L-Phe, (B) L-Trp, (C) L-His, (D) L-Leu, (E) L-Ile, (F) L-Ser, (G) L-Ala, (H) L-Pro, (I) L-Tyr, (J) L-LeuME, (K) Gly.

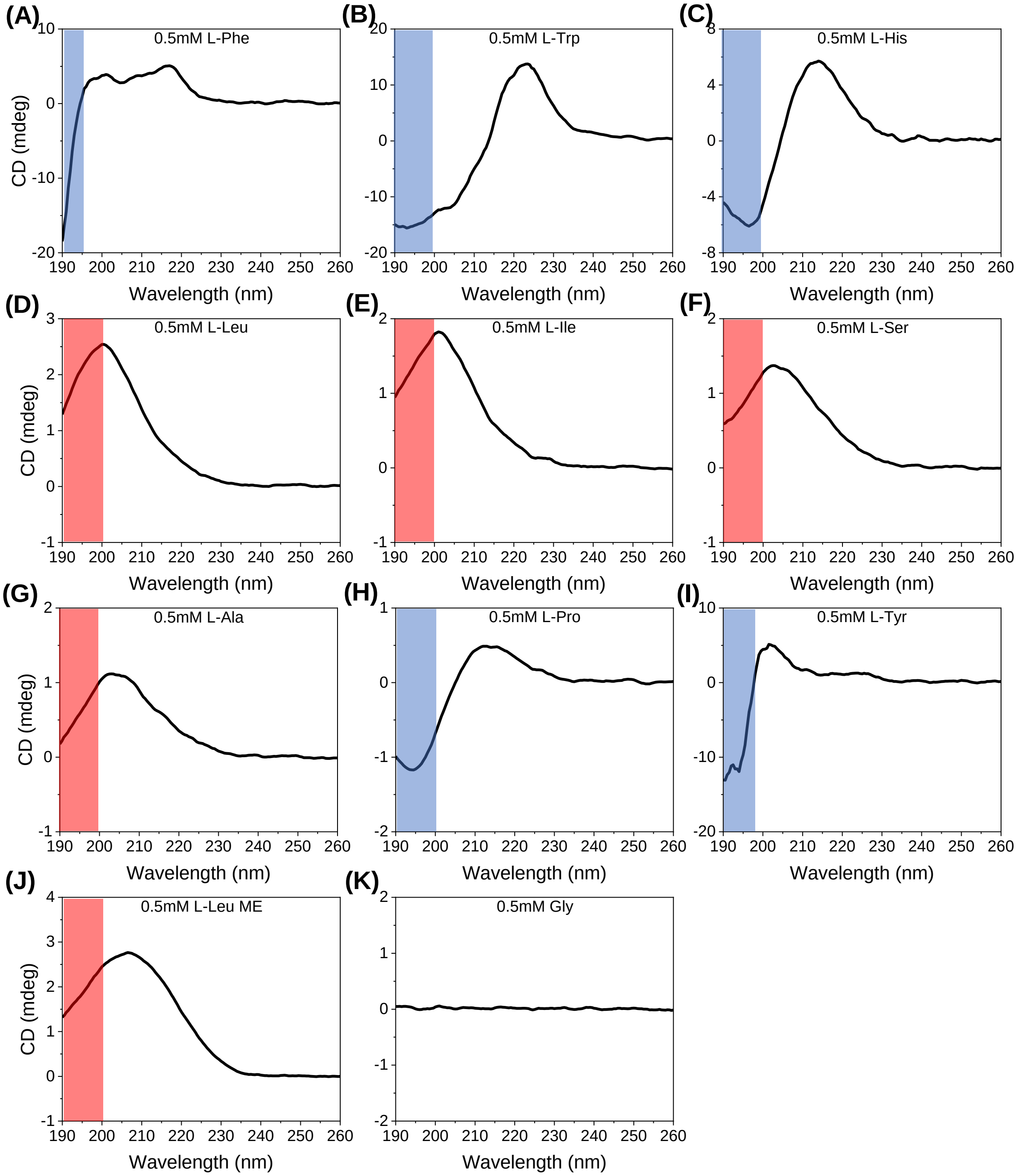

Figure C. 14 CD spectra of 0.5 mM solutions of the different amino acids studied in 2 mM phosphate buffer solution at pH 9; (A) L-Phe, (B) L-Trp, (C) L-His, (D) L-Leu, (E) L-Ile, (F) L-Ser, (G) L-Ala, (H) L-Pro, (I) L-Tyr, (J) L-LeuME, (K) Gly.